Cellular-connected UAV in Next-Generation Wireless Networks

by

Nesrine Cherif

Thesis submitted to the University of Ottawa
In partial fulfillment of the requirements for the degree of

Doctor of Philosophy in Electrical and Computer Engineering

School of Electrical Engineering and Computer Science
Faculty of Engineering
University of Ottawa

Abstract

Unmanned aerial vehicle (UAV) technology has gained a great interest in communication systems due to its ability to host a cellular base station (BS) and thus act as an aerial BS (UAV-BS). The inheritance of mobility in the airspace makes the deployment of UAV-BSs flexible and agile aiming to mainly complement the terrestrial network, extend its coverage, and serve as a capacity injector in high-throughput demand scenarios. Besides, a UAV can also act as an aerial user (UAV-UE) for various use cases, such as aerial data collection and cargo delivery. Such UAV-UE missions need reliable cellular communication links in order to safely operate in beyond visual line-of-sight (BVLoS). Since terrestrial networks were not primarily designed to serve aerial users, due to their down-tilted BS antennas, re-coursing solely to these networks for aerial users' cellular connectivity might not be a viable approach as a long-term solution. Alternatively, deploying UAV-BSs in this context can substantially improve both aerial and terrestrial users coverage and capacity. One of the challenging issues is how to characterize the UAV-UE performance in integrated aerial/terrestrial networks, called vertical heterogeneous networks (VHetNets). First, we thoroughly study the aerial user's performance in terms of coverage probability in a VHetNets setup. Under a more realistic system model, we revisit the coverage and throughput performances of an aerial user in VHetNets, considering LoS and non-LoS (NLoS) transmissions and under different spectrum sharing policies among separate aerial and terrestrial networks. Some insights have been concluded on the integration of aerial BSs and UAV-UEs with the existing terrestrial network. Specifically, optimal positioning of UAV-BSs for maximized aerial users coverage was investigated for various aerial users distribution and spectrum allocations. Moreover, visioning that UAV technology will revolutionize the cargo delivery industry, we proposed a new concept of 3D aerial highways, which designs coordinated routes for a massive number of UAVs used mainly for delivery purposes. In this context, multiple network technologies were proposed and discussed to guarantee the cellular connectivity of cargo-UAVs in 3D aerial highways. For the particular case of connectivity supported by terrestrial cellular networks, an optimal energy-efficient and low-handoff trajectory planning for a cargo-UAV mission was proposed, with respect to disconnectivity constraints. Consequently, associated design guidelines and recommendations have been drawn. Leveraging reinforcement learning (RL) tools, we proposed a novel algorithm for path planning and cell association for the cargo-UAV that maximizes its cellular service reliability and minimizes the handoff events. Finally, we introduced a new paradigm, intermittently tethered UAV (iTUAV), as a trade-off between mobility and energy availability for providing cellular connectivity in temporary events.

Dedicated to

My Loving parents Zohra & Mohamed

My supportive husband Fathi

My little princess Ameerah

Acknowledgments

First and foremost praise is to Allah, the most Gracious and the most Merciful, on whom ultimately we depend for sustenance and guidance. I am grateful to Allah for giving me strength and determination to complete my research.

This thesis has been seen through to completion with the continuous support of numerous people including my family, friends, colleagues and various institutions.

First of all, I would like to thank and express my sincere gratitude to my supervisors Professor Abbas Yongacoglu and Professor Halim Yanikomeroglu for providing necessary resources and guidance throughout my research.

My sincere gratitude goes also to Dr. Wael Jaafar. His expertise and insightful comments were helped me produce a high quality research papers. Indeed, his quick feedback and constructive comments were really valuable and helpful. This work would not been possible without his guidance and encouragement. I deeply hope he is satisfied by what I accomplished during my PhD research.

I would like also to express my gratitude to the University of Ottawa and the government of Ontario for supporting me financially throughout my graduate studies.

Finally, I would like to thank my family. They have been always encouraging me with their best wishes and prayers. I hope I have made them proud of me.

Table of Contents

List of Tables

List of Figures

List of Abbreviations

3D	Three Dimensional
3GPP	3^{rd} Generation Partnership Project
5G	Fifth Generation network of wireless communications
A2A	Air-to-Air channel
A2G	Air-to-Ground channel
BS	Base Station
BPP	Binomial Point Process
BVLoS	Beyond Visual Line of Sight
C&C	Command-and-Control
C2A	Cellular-to-Air channel
Cargo-UAV	Cargo Unmanned Aerial Vehicle
CDF	Cumulative Distribution Function
CoV	Coefficient of Variation
CVRP	Capacitated Vehicle Routing Problem
D2D	Device-to-Device
DLC	Distributed Laser Charging

DP	Dynamic Programming
EIRP	Effective Isotropic Radiated Power
FAA	Federal Aviation Administration
FSO	Free-Space Optics
HAPS-SMBS	High Altitude Platform Station Super Macro BS
HPPP	Homogeneous Poisson Point Process
IAB	Integrated Access and Backhaul
IoT	Internet of Things
iTUAV	intermittently Tethered UAV
ITU	International Telecommunication Union
LEO	Low Earch Orbit
LoS	Line-of-Sight
LTE	Long Term Evolution
MCPP	Matérn Cluster Point Process
MDP	Markov Decision Process
MIMO	Multiple Input Multiple Output
MINLP	Mixed Integer Non Linear Problem
mmWave	millimiter Wave
NLoS	Non Line-of-Sight
NOMA	Non-Orthogonal Multiple Access
N-OSS	Non Orthogonal Spectrum Sharing

NR	New Radio
OSS	Orthogonal Spectrum Sharing
QoS	Quality-of-Service
RL	Reinforcement Learning
RSRP	Reference Signal Received Power
SIR	Signal-to-Interference Ratio
SINR	Signal-to-Interference-Plus-Noise Ratio
SWAP	Size Weight And Power
PDF	Probability Distribution Function
PPP	Poisson Point Process
TBS	Terrestrial BS
TUAV	Tethered Unmanned Aerial Vehicle
UTM	Unmanned aircraft system Traffic Management
UAV	Unmanned Aerial Vehicle
UAV-BS	UAV Base Station
UE	User Equipment
ULA	Uniform Linear Array
UMa	Urban Macro
UMi	Urban Micro
UxNB	On-board radio access node
VHetNets	Vertical Heterogeneous Networks

Chapter 1

Introduction

1.1 Motivation

Since the appearance of the first wireless systems at the end of the last century, the communication paradigm has always evolved around users on the ground. These wireless communication users can range from humans to machines to internet-of-things (IoT) devices and autonomous vehicles, to name few. In fact, all these communication systems users have a common characteristic which is that they all exist and operate on the ground level that we refer as terrestrial users. Recently, with the great technology advancements of unmanned aerial vehicle (UAV), the technology was integrated and deployed over a wide range of applications such as aerial video surveillance, aerial cargo delivery, smart agriculture by detecting crops disease and examining soil texture. This has lead to the emergence of new type of cellular users at elevated altitudes. In this regard, reliable wireless communication links are crucial for the safety and security of UAV missions. Indeed, the risk of accidents or malfunction of a UAV results in a serious threat to individuals and properties especially if it operates in dense urban centres. Hence, providing robust communication link to these flying autonomous vehicles is necessary for its safe deployment especially at beyond visual line-of-sight (BVLoS). Thus, command-and-control (C&C) exchanges with UAVs during their missions ensure the quick intervention under any dangerous or unexpected situation.

While the conventional terrestrial network was primarily designed to serve wireless users on the ground and with its BS antennas tilted-down toward the terrestrial users, re-utilizing the network for UAV users' cellular connectivity may not be adequate as a long-term solution for providing seamless and reliable wireless transmission links. Indeed, it was shown that at elevated altitudes, the coverage holes are more recurrent and frequent which result in compromising the UAV operations [2,3]. Motivated by the aforementioned issues, UAV mounted with BS, i.e., UAV-BS, has emerged as a deal breaker for aerial users cellular connectivity especially that aerial users and UAV-BSs operate in the same airspace environment and enjoy the flexibility of deployment and scalability. In recent years, deploying UAV-BS was so attractive for various use cases ranging from capacity injection in high-throughput demand scenarios like sport events and big concerts [4,5] to data collection for massive IoT [6]. Indeed, the research community studied extensively multiple UAV-BS configurations and deployments such as backhaul capacity limits [7,8] and caching from the sky [9], to name few. However, to the best of our knowledge, most of the literature on UAV-BS focused on terrestrial users-oriented deployments. However, with the resurgence of UAV users, i.e., UAV-UEs, and the skyrocketing predictions about the prominence of UAVs in the future for transportation, cargo-delivery, video-surveillance, and IoTs data collection, cellular connectivity for these aerial users become a crucial issue as the safety and security of the UAV missions are monitored closely through C&C exchanges that in abundant need for ubiquitous and reliable cellular transmission links.

The emergence of UAVs as cellular users led to many efforts in studying and thoroughly investigating the viability and practicality of re-utilizing the existing terrestrial network for aerial coverage. In this regards, multiple works have looked at this possibility [10,11] and the conclusion that has been drawn is that likely terrestrial network as a stand-alone cellular connectivity provider for UAV users is not adequate as its aerial coverage exhibits frequent coverage holes at elevated altitudes of operation. Imminent deployments of aerial users can benefit from terrestrial cellular service as the research community is still looking at different network options available for UAV users. However, with the high throughput demand for aerial users in different scenarios, e.g., aerial high-resolution video surveillance, may not be satisfied by the current network design. Thanks to the huge advancements in UAV on-board battery autonomy and its extreme energy efficiency, UAV equipped with BS, i.e., UAV-BS, can be deployed for extended amount of time until a pull back is requested for battery charging. This leads to the tremendous opportunity of deploying UAV-BS for cellular coverage of aerial users thanks to its flexibility in deployment.

1.2 Thesis Contributions

UAV, as an aerial UE that is in need for cellular connectivity to safely execute its missions or as a flying BS that is deployed to provide cellular coverage for aerial and/or terrestrial users in different scenarios, requires an inter-disciplinary collaboration between governments regulatory authority and cellular network operators. Indeed, regulations on UAV operations are constantly reviewed and updated based on the advancements of the technology. Essentially, safety and security of the UAV technology are the essence for the government regulation and the public acceptance. Hence, in the next few years, regulations around UAV deployment is expected to be more relaxed in terms of the maximum altitude of flying, the maximum allowed weight of UAV, and the no-fly zones [5, 12].

As UAVs are seen as the technology for the future in civil applications (cargo delivery, agriculture monitoring, urban video surveillance, . . .), the catalyst for their successful deployment and functioning is the presence of ubiquitous and reliable cellular connectivity. In the other hand, UAV equipped with BS, i.e., UAV-BS, is discussed for the last few years as an agile and easy-to-deploy solution in on-demand capacity injection or in natural disasters [13, 14]. Yet, UAV-BS can be deployed to complement the terrestrial network in providing cellular connectivity for UAV-UEs. However, performance analysis and optimization of such a complex integrated network, i.e., terrestrial and aerial BSs with aerial users, is not addressed in the literature. Specifically, we identified some of the challenges of UAV-UE operation in integrated aerial and terrestrial networks, i.e., vertical heterogeneous networks (VHetNets) [15–17], that we listed below:

- The coverage probability and the achievable throughput of an aerial user in VHetNets setup is not investigated yet. Thus, by leveraging tools from stochastic geometry, we characterized the cellular coverage of an aerial user in VHetNets in Chapter 2. Assuming line-of-sight (LoS) and non-LoS (NLoS) transmissions, the aerial user's performance is revisited to drew some recommendations and insights on the deployment of aerial users and BSs. This was exposed in Chapter 3.

- Since the terrestrial network was designed to serve terrestrial users on the ground, supplying cellular connectivity for aerial users in elevated heights may require the integration of a new cellular network more adopted to serve these highly mobile users. UAV-BS, as the same nature of technology as the UAV-UEs is best suited for their cellular coverage. Thus, the optimal deployment of a UAV-BS for maximal coverage of UAV-UEs should be investigated. In Chapter 4, we propose an algorithm to optimally place the UAV-BS in 3D for maximal coverage of UAV-UEs under different spectrum sharing policies between aerial and terrestrial networks.

- Cargo-delivery using UAV has been gaining a great momentum in recent years thanks to Amazon Prime Air service that was launched in remote and hard-to-reach areas [18]. With the increasing shift in consumers habits toward online shipping, UAV-based cargo delivery is in front of a huge opportunity to be used for large-scale cargo shipping operations through airspace. The logistics and coordination of simultaneous massive cargo-UAV missions is crucial to ensure the safety and security of UAVs operations. The vision to design *3D aerial highways* is exposed in Chapter 5 where we propose an AI-based framework to design and deploy 3D aerial highways.

- The imminent deployment of UAV for cargo-delivery is limited to the use the existing terrestrial cellular network, as no other network (UAV-BS or satellite) is mature enough to provide the connectivity for cargo-UAV. Thus, UAV-based cargo delivery deployed in the near future is likely to rely solely on terrestrial network for C&C exchanges. Aware of the frequent terrestrial BSs coverage holes in the airspace, we proposed an algorithm for planning a disconnectivity-aware energy-efficient trajectory of the cargo-UAV with minimum handoffs in Chapter 6.

- We revisit the cargo-UAV path planning problem from a new perspective of cell association that substantially decrease the handoff rate and the cellular disconnectivity at a slight cost of on-board battery consumption. The reinforcement learning (RL) based algorithm is highlighted in Chapter 7.

- A new paradigm for serving aerial BS referred as intermittently tethered UAV (iTUAV) is introduced in Chapter 8. iTUAV technology is presented as a balance between the UAV-BS extreme flexibility and unlimited power supply that tethered UAV enjoys. Through simulations, we prove that iTUAV technology outperforms some benchmarks of cellular system at the expense of slightly investing in the deployment of anchor nodes. iTUAV systems are expected to be easily extended to service cellular-connected UAV along terrestrial users.

- Finally, a summary of this work, along with some future research directions are presented in Chapter 9.

1.3 Publications

During the PhD program, the following is a list of publications that has been co-authored:

N. Cherif, M. Alzenad, H. Yanikomeroglu, and A. Yongacoglu, "Downlink coverage and rate analysis of an aerial user in vertical heterogeneous networks (VHetNets)", *IEEE Transactions on Wireless Communications*, vol. 20, no. 3, pp. 1501-1516, Mar. 2021.

N. Cherif, W. Jaafar, H. Yanikomeroglu, and A. Yongacoglu, "On the optimal 3D placement of a UAV base station for maximal coverage of UAV users", *IEEE Global Communications Conference* (Globecom), Taipei, Taiwan, Dec. 2020, pp. 1-6.

N. Cherif, M. Alzenad, H. Yanikomeroglu, and A. Yongacoglu, "Downlink coverage analysis of an aerial user in vertical heterogeneous networks", *IEEE Global Communications Conference* (Globecom), Waikoloa, Hawaii, USA, Dec. 2019, pp. 1-6.

N. Cherif, W. Jaafar, H. Yanikomeroglu, and A. Yongacoglu, "3D aerial highway: The key enabler of the retail industry transformation", *IEEE Communications Magazine*, vol. 59, no. 9, pp. 65-71, September 2021.

N. Cherif, W. Jaafar, H. Yanikomeroglu, and A. Yongacoglu, "RL-Based Cargo-UAV Trajectory Planning and Cell Association for Minimum Handoffs, Disconnectivity, and Energy Consumption", under review at *IEEE Transactions on Vehicular Technologies*.

N. Cherif, W. Jaafar, H. Yanikomeroglu, and A. Yongacoglu, "Disconnectivity-aware energy-efficient cargo-UAV trajectory planning with minimum handoffs", *IEEE International Communications Conference* (ICC), Montreal, Quebec, Canada, Jun. 2021, pp. 1-6. This paper has won "Best Paper Award IEEE ICC 2021".

N. Cherif, W. Jaafar, E. Vinogradov, H. Yanikomeroglu, S.Pollin and A. Yongacoglu, "iTUAVs: Intermittently tethered UAVs for future wireless networks", Accepted for publication at *IEEE Wireless Communications Magazine*.

1.4 Thesis Organization

The rest of this thesis is organized as follows. Chapters 2 and 3 study the performance of an aerial user, i.e., UAV-UE, in a VHetNets using stochastic geometry tools. Then, we focus on the 3D placement problem of a UAV-BS for maximal coverage of UAV-UEs assuming spectrum sharing in VHetNets in Chapter 4. In Chapter 5, we propose our vision for massive UAV-based cargo delivery using 3D aerial highways. We study the viability of different communication network options of cellular connectivity of cargo-UAVs. Aligned with our vision presented in Chapter 5, we proposed a disconnectivity-constrained energy-efficient dynamic programming-based algorithm for cargo-UAV trajectory planning with minimum handoffs in Chapter 6. Joint cell association and trajectory planning for the cargo-UAV is revisited in Chapter 7 leveraging tools from reinforcement learning. Moreover, we introduce a new technology, iTUAV, to provide cellular coverage for users in temporary events in Chapter 8 as a tradeoff between UAV-BS mobility and TUAV infinite power supply. Finally, a brief summary on the work conducted in this thesis with some future research directions are presented in Chapter 9.

Chapter 2

Downlink Coverage Analysis of An Aerial User in Vertical Heterogeneous Networks

2.1 Introduction

The use of unmanned aerial vehicles (UAVs) in the 5th generation (5G) wireless networks has gained a great interest. The main features that distinguish UAV-based wireless networks from their terrestrial counterparts are their agility and flexibility. For instance, a UAV can be deployed for search-and-rescue missions, package delivery, and as flying taxis [19, 20]. In such applications, the UAV needs a wireless connectivity in order to perform its mission, and thus we can refer to it as an aerial user. Similarly, the UAV can be equipped with antennas and act as an aerial-BS that can provide on-demand wireless connectivity, e.g., for a large gathering of people during a temporary event or in the case of a terrestrial infrastructure failure [21–23]. This wide range of UAV use cases leads to

This work has been published in IEEE Globecom 2019 proceedings: **N. Cherif**, M. Alzenad, H. Yanikomeroglu, and A. Yongacoglu, "Downlink coverage analysis of an aerial user in vertical heterogeneous networks", *IEEE Global Communications Conference* (Globecom), Waikoloa, Hawaii, USA, Dec. 2019, pp. 1-6.

the prominent coexistence of aerial users along with terrestrial-BSs and aerial-BSs. The deployment of aerial users in such heterogeneous networks, i.e., terrestrial and aerial networks, is still an open question in the literature and has not been investigated thoroughly yet.

Prior works investigated the downlink coverage probability and achievable rate of either a terrestrial user or an aerial user in the presence of either terrestrial-BSs or aerial-BSs. In [11], the authors studied the feasibility of serving aerial users and terrestrial users by a terrestrial wireless network. Their analysis shows that the excellent channel conditions that the aerial user enjoy with the terrestrial-BSs comes with the cost of a very high interference which leads to a very poor signal-to-interference-and-noise ratio (SINR) at the aerial user. Although, the imminent deployment of aerial-BS as a candidate for providing cellular connectivity, the authors limited their discussion to the re-use of the existing terrestrial network.

While the PPP assumption has become the baseline to model the locations of terrestrial-BSs, it is not suitable to model aerial networks especially with small number of aerial-BSs whose deployed over a finite area. As Binomial Point Process (BPP) was adopted to model terrestrial ad hoc networks with a given number of nodes and distributed over a circular area [24, 25], it presents a reasonable model for aerial networks while assuring the analytical analysis tractability. For instance, the work in [26] was the first to consider such model for aerial networks. In [26], the performance of a terrestrial user exclusively served by aerial-BSs is investigated. The results show that the coverage performance of the terrestrial user decreases as the height of aerial-BSs increases. Moreover, this work does not implement any technique to combat the strong aerial interference signals. The opportunity of re-utilizing existing terrestrial wireless networks to provide coverage for aerial users has been considered in [27]. Indeed, this work proposed several interference mitigation techniques both in the uplink and downlink to maintain an acceptable signal power for the terrestrial and aerial users. Finally, an integrated aerial-terrestrial network comprising aerial-BSs and terrestrial-BSs (VHetNet) is investigated in [15, 16]. Exact and approximate analytical expressions for the downlink coverage and rate are presented in [16].

However, the analysis, in this work, is done for a typical terrestrial user, and hence it is not applicable for the aerial users.

2.2 System Model

We assume a network of macro terrestrial-BSs with heights of h_{T} (meters) uniformly distributed on the ground according to a homogeneous PPP, denoted by Φ_{T}, with density λ_{T}. On the other hand, N aerial-BSs are assumed to be distributed as a BPP, denoted by Φ_{A}, over a disc with a radius r_{D} at a height h_{A} (meters) above the ground. It is noteworthy that if the aerial-BSs are of different heights, our analysis is still applicable since the performance of a network of aerial-BSs distributed between two heights, h_{min} and h_{max}, converges to the same performance of an aerial network uniformly distributed at an average height of $\frac{h_{\mathrm{min}}+h_{\mathrm{max}}}{2}$ [26]. It follows that the density of the BPP $\lambda_{\mathrm{A}} = \frac{N}{\pi r_{\mathrm{D}}^2}$ aerial-BSs/km^2. We consider a typical aerial user located at a height h_{U} (meters) above the ground, i.e., at the 3D location $(0, 0, h_{\mathrm{U}})$.

2.2.1 Cellular-to-Air Channel

We assume that the cellular-to-air (C2A) links between the terrestrial-BSs and the aerial user are LoS transmissions. As a result, the received power at the aerial user from the j-th terrestrial-BS located at point x_j is given by

$$P_{r,j}^{T} = P_T \eta_T \mathrm{H}_T^{x_j} d_{T,x_j}^{-\alpha_T}, \tag{2.1}$$

where P_T and η_T denote the transmit powers of the terrestrial-BSs and the extra losses due to the C2A propagation, respectively. It is noteworthy that aerial user are most likely to be served by the terrestrial-BSs antenna's sidelobe [11]. Indeed, the terrestrial-BSs antenna's sidelobe gain is incorporated in the transmit power P_T. $\mathrm{H}_T^{x_j}$ is the small-scale fading component which is assumed to follow Gamma distribution, i.e., $\mathrm{H}_T^{x_j} \sim$ Gamma $(m_T, 1/m_T)$, where m_T is the fading parameter, d_{T,x_j} denotes the 3-D distance between the j-th terrestrial-BS and the aerial user. Finally, α_T is the path-loss exponent.

2.2.2 Air-to-Air Channel

The links between a typical aerial user and an aerial-BSs are assumed to be LoS transmissions [28, 29]. Also, we assume that the aerial-BSs employ beamforming to improve the SIR. We denote by G_r, the gain of the aerial-BS antenna at an arbitrary location towards the aerial user which is given by [30]

$$G_r = \begin{cases} G_{\mathrm{A}}, & -\frac{\theta_B}{2} \leqslant \psi \leqslant \frac{\theta_B}{2} \\ g_{\mathrm{A}}, & \text{otherwise}, \end{cases} \tag{2.2}$$

where G_A and g_A are the mainlobe and sidelobe gains, respectively, ψ is the sector angle and $\theta_B \in [0, 180]$ is the beamwidth in degrees. The received power at the aerial user from the i-th aerial-BS located at point x_i is given by

$$P_{r,i}^A = P_A G_r \eta_A \mathrm{H}_A^{x_i} d_{A,x_i}^{-\alpha_A}, \tag{2.3}$$

where P_A and η_A are the transmit powers of the aerial-BSs and the excess losses, respectively. $\mathrm{H}_A^{x_i}$ is the small-scale fading component which is assumed to follow Gamma distribution, i.e., $\mathrm{H}_A^{x_i} \sim \text{Gamma}\,(m_A, 1/m_A)$, where m_A is the fading parameter, d_{A,x_i} is the 3-D distance between the typical aerial user and the i-th aerial-BS. Finally, α_A is the path-loss exponent.

Unlike terrestrial-BSs whose antennas are tilted down towards ground users, the aerial-BSs can direct their beams towards their associated aerial users. Hence, the beamforming gain from the serving aerial-BS towards the typical aerial user is always G_{A} [31]. For the remaining aerial-BSs, their main beams may not necessarily be aligned with the typical aerial user. We introduce a probability q_{A} that depends on the beamwidth θ_B that quantifies the likelihood that an interfering aerial-BS's mainlobe is directed towards the typical aerial user. The gain of the interfering aerial-BS is g_{A} when the typical aerial user is in its sidelobe direction with occurrence probability $1 - q_{\mathrm{A}}$. Typically, g_{A} is 20 dB less than main lobe gain G_{A} [31].

2.2.3 BS Association

The typical aerial user is served by a single BS, located at point x_0, that offers the strongest average biased received power [32,33]. It is noteworthy that the beamforming at the serving aerial-BS is taken into account at the aerial user association. Since $\mathbb{E}[\mathrm{H}_T^{x_j}] = \mathbb{E}[\mathrm{H}_A^{x_j}] = 1$ for each $x_j \in \Phi_\mathrm{T} \cup \Phi_\mathrm{A}$ and noting that the aerial user is associated with either the closest aerial-BS or the closest terrestrial-BS, the serving BS can be written as

$$x_0 = \arg\max\{B_T \mu_T R_T^{-\alpha_T}, B_A \mu_A R_A^{-\alpha_A}\}, \tag{2.4}$$

where $B_\nu, \nu \in \{\mathrm{T}, \mathrm{A}\}$ is an added bias factor to force the extension/shrinking of the coverage in the tier Φ_ν, $\mu_T = P_T \eta_T$, $\mu_A = P_A G_A \eta_A$, $R_T = \min\limits_{\forall x_j \in \Phi_\mathrm{T}} d_{T,x_j}$, and $R_A = \min\limits_{\forall x_i \in \Phi_A} d_{A,x_i}$.

For simplicity, we assume an interference-limited network, and thus the noise can be ignored. The signal-to-interference ratio (SIR) can then be written as

$$\gamma = \frac{\mu_\nu \mathrm{H}_\nu^{x_0} R_\nu^{-\alpha_\nu}}{I_T + I_A}, \quad \text{if } x_0 \in \Phi_\nu(\mathcal{E}_\nu), \;\; \nu \in \{\mathrm{T}, \mathrm{A}\}, \tag{2.5}$$

where $\mathcal{E}_\nu$ denotes the event that the serving BS belongs to the tier Φ_ν. Finally, I_T and I_A are the terrestrial and aerial interference powers, respectively, which can be expressed as

$$I_T = \sum_{x_j \in \Phi_\mathrm{T} \setminus x_0} \mu_T \mathrm{H}_T^{x_j} d_{T,x_j}^{-\alpha_T} \tag{2.6}$$

$$I_A = \sum_{i=1, x_i \in \Phi_\mathrm{A} \setminus x_0}^{N} P_A G_r \eta_A \mathrm{H}_A^{x_i} d_{A,x_i}^{-\alpha_A}, \tag{2.7}$$

where $G_r = G_\mathrm{A}$ with a probability of q_A and $G_r = g_\mathrm{A}$ with a probability of $1 - q_\mathrm{A}$.

2.3 Coverage Analysis

In this section, we start by deriving several relevant distance distributions and the association probabilities. Then, closed-form expressions for the Laplace transforms of the aggregated interference powers given in (2.6) and (2.7) are derived. Finally, we characterize the coverage probability of the typical aerial user.

2.3.1 Distances Distributions of the Nearest Terrestrial-BS and Aerial-BS

The PDF and CDF of the distance between the aerial user and the nearest terrestrial-BS, denoted by R_T, are given by [31, Eqs.(8) and (9)]

$$f_{R_T}(r) = 2\pi\lambda_{\mathrm{T}} r \exp\left(-\pi\lambda_{\mathrm{T}}\left(r^2 - h_{\mathrm{UT}}^2\right)\right), r \geqslant h_{\mathrm{UT}} \tag{2.8}$$

$$F_{R_T}(r) = 1 - \exp\left(-\pi\lambda_{\mathrm{T}}\left(r^2 - h_{\mathrm{UT}}^2\right)\right), \quad r \geqslant h_{\mathrm{UT}}, \tag{2.9}$$

where $h_{\mathrm{UT}} = h_{\mathrm{U}} - h_{\mathrm{T}}$. Similarly, the PDF and the CDF of R_A are given by [26]

$$f_{R_A}(r) = N\left(\frac{2r}{r_{\mathrm{D}}^2}\right)\left(\frac{d^2 - r^2}{r_{\mathrm{D}}^2}\right)^{N-1}, h_{\mathrm{UA}} \leqslant r \leqslant d \tag{2.10}$$

$$F_{R_A}(r) = \begin{cases} 0, & r \leqslant h_{\mathrm{UA}} \\ 1 - \left(\frac{d^2 - r^2}{r_{\mathrm{D}}^2}\right)^N, & h_{\mathrm{UA}} \leqslant r \leqslant d \\ 1, & r \geqslant d, \end{cases} \tag{2.11}$$

where $h_{\mathrm{UA}} = h_{\mathrm{A}} - h_{\mathrm{UT}}$ and $d = \sqrt{r_{\mathrm{D}}^2 + h_{\mathrm{UA}}^2}$.

2.3.2 Distances of the Nearest Interfering BSs

In Table 2.1, we summarize the distances of the nearest interfering BSs given that the aerial user is associated with an aerial-BS or terrestrial-BS (i.e., conditioned on the events $\mathcal{E}_\nu, \nu \in \{\mathrm{T}, \mathrm{A}\}$). Note that N' in Table 2.1 quantifies the number of interfering aerial-BSs which depends on the association policy.

2.3.3 Association Probabilities

Lemma 2.1. The probability that the aerial user is associated with a terrestrial-BS is given by

$$\mathcal{A}_{\mathrm{T}} = \begin{cases} 1 - \exp\left(-\pi\lambda_{\mathrm{T}}\left(\zeta^2 - h_{\mathrm{UT}}^2\right)\right) + \frac{\pi\lambda_{\mathrm{T}} h_{\mathrm{UT}}^2}{r_{\mathrm{D}}^{2N}} \\ \times \sum_{i=0}^{N} \binom{N}{i} (-1)^i d^{2(N-i)} \left(\frac{B_A \mu_A}{B_T \mu_T}\right)^{\frac{2i}{\alpha_A}} (\pi\lambda_{\mathrm{T}})^{-\frac{\alpha_T i}{\alpha_A}} \\ \times \left[\Upsilon(\zeta) - \Upsilon(\zeta_{\mathrm{A}}^{\mathrm{T}}(d))\right], & h_{\mathrm{UT}} \leqslant \zeta_{\mathrm{A}}^{\mathrm{T}}(d) \\ 0, & h_{\mathrm{UT}} \geqslant \zeta_{\mathrm{A}}^{\mathrm{T}}(d). \end{cases} \tag{2.12}$$

Table 2.1: Interferers distances

Event	Nearest interferer distance	N'
$\mathcal{E}_{\mathrm{T}}$	$\tau_{A\mid\mathcal{E}_{\mathrm{T}}}(r) = \begin{cases} h_{\mathrm{UA}}, & h_{\mathrm{UT}} \leqslant \zeta_{\mathrm{A}}^{\mathrm{T}}(h_{\mathrm{UA}}) \\ \left(\frac{B_A \mu_A r^{\alpha_T}}{B_T \mu_T}\right)^{\frac{1}{\alpha_A}}, & \zeta_{\mathrm{A}}^{\mathrm{T}}(h_{\mathrm{UA}}) \leqslant r \leqslant \zeta_{\mathrm{A}}^{\mathrm{T}}(d), \end{cases}$ where $\zeta_{\mathrm{A}}^{\mathrm{T}}(x) = \left(\frac{B_T \mu_T x^{\alpha_A}}{B_A \mu_A}\right)^{\frac{1}{\alpha_T}}$	N
$\mathcal{E}_{\mathrm{A}}$	$\tau_{T\mid\mathcal{E}_{\mathrm{A}}}(r) = \begin{cases} h_{\mathrm{UT}}, & h_{\mathrm{UA}} \leqslant r \leqslant \zeta_{\mathrm{T}}^{\mathrm{A}} \\ \left(\frac{B_T \mu_T r^{\alpha_A}}{B_A \mu_A}\right)^{\frac{1}{\alpha_T}}, & \zeta_{\mathrm{T}}^{\mathrm{A}} \leqslant r \leqslant d, \end{cases}$ where $\zeta_{\mathrm{T}}^{\mathrm{A}} = \left(\frac{B_A \mu_A h_{\mathrm{UT}}^{\alpha_T}}{B_T \mu_T}\right)^{\frac{1}{\alpha_A}}$	$N-1$

where $\zeta = \arg\max\left\{h_{\mathrm{UT}}, \zeta_{\mathrm{A}}^{\mathrm{T}}(h_{\mathrm{UA}})\right\}$ and $\Upsilon(x) = \Gamma\left[\frac{\alpha_T}{\alpha_A} i + 1, \pi \lambda_{\mathrm{T}} x^2\right]$, where $\Gamma[\cdot,\cdot]$ is the upper incomplete Gamma function [34, 8.358.2].

Proof: See Appendix A.1.

The probability that the aerial user is associated with an aerial-BS is given by $\mathcal{A}_{\mathrm{A}} = 1 - \mathcal{A}_{\mathrm{T}}$.

2.3.4 Serving Distance Distributions

In the following lemmas, we present the distributions of the serving distances conditioned to the aerial user association policy.

Lemma 2.2. Conditioned on the event that the aerial user is associated with a terrestrial-BS, i.e., conditioned on $\mathcal{E}_{\mathrm{T}}$, the PDF of the distance between a serving terrestrial-BS and the typical aerial user is given by

$$f_{\tilde{R}_T|\mathcal{E}_\mathrm{T}}(r)=\begin{cases}\frac{2\pi\lambda_\mathrm{T}}{\mathcal{A}_\mathrm{T}}\left(\frac{d^2-\tau^2_{A|\mathcal{E}_\mathrm{T}}(r)}{r_\mathrm{D}^2}\right)^N r\exp\left(-\pi\lambda_\mathrm{T}\left(r^2-h_\mathrm{UT}^2\right)\right), & \\ & r\in\mathfrak{R}_\mathrm{T}\\ 0, & \text{otherwise,}\end{cases} \tag{2.13}$$

where $\mathfrak{R}_\mathrm{T}=[h_\mathrm{UT},\zeta_\mathrm{A}^\mathrm{T}(d)]$. Note that according to (2.12), $\mathcal{A}_\mathrm{T}=0$ outside $\mathfrak{R}_\mathrm{T}$.

Proof: See Appendix A.2.

Lemma 2.3. Conditioned on the event that the aerial user is associated with an aerial-BS, i.e., conditioned on $\mathcal{E}_\mathrm{A}$, the PDF of the distance between a serving aerial-BS and the typical aerial user is given by

$$f_{\tilde{R}_A|\mathcal{E}_\mathrm{A}}(r)=\begin{cases}\frac{2N}{\mathcal{A}_\mathrm{A}}r\exp\left(-\pi\lambda_\mathrm{T}\left(\tau_{T|\mathcal{E}_\mathrm{A}}(r)^2-h_\mathrm{UT}^2\right)\right) & \\ \times\frac{1}{r_\mathrm{D}^{2N}}\left(d^2-r^2\right)^{N-1}, & r\in\mathfrak{R}_\mathrm{A}\\ 0, & \text{otherwise,}\end{cases} \tag{2.14}$$

where $\mathfrak{R}_\mathrm{A}=[h_\mathrm{UA},d]$.

Proof: The proof is similar to the proof of Lemma 2.2, therefore omitted here.

2.3.5 Laplace Transform of the Aggregated Interference

As easily seen from (2.6), the aerial user receives interference signals from the terrestrial-BSs and aerial-BSs. In the following lemmas, we present closed-form expressions for the Laplace transform of the terrestrial and aerial interference powers conditioned on the events $\mathcal{E}_\nu,\nu\in\{\mathrm{T},\mathrm{A}\}$ and the serving BS located at the distance r from the aerial user.

Lemma 2.4. Conditioned on $\mathcal{E}_\nu,\nu\in\{\mathrm{T},\mathrm{A}\}$, the Laplace transform of the terrestrial interference is given by

$$\mathcal{L}_{I_T|\mathcal{E}_\nu}(s)=\exp\Bigg(-2\pi\lambda_\mathrm{T}\sum_{i=0}^{m_T-1}\left(\frac{s\mu_T}{m_T}\right)^{1+i-m_T}\frac{1}{\alpha_T\Gamma[m_T-i]}$$
$$\times\tau_{T|\mathcal{E}_\nu}(r)^{\alpha_T(m_T-i-1)}\Theta(s,\tau_{T|\mathcal{E}_\nu}(r))\Bigg), \tag{2.15}$$

where $\Theta(\cdot,\cdot)$ is defined as

$$\Theta(\mathbf{s},\mathbf{r}) = \mathrm{G}_{2,2}^{2,1}\left[\frac{\mathbf{r}^{\alpha_T} m_T}{\mathbf{s}\mu_T}\middle| \begin{matrix} 1+i-m_T, 2+i-m_T-\frac{2}{\alpha_T} \\ 1+i-m_T-\frac{2}{\alpha_T}, 0 \end{matrix}\right], \tag{2.16}$$

where $\mathrm{G}[\cdot]$ is the Meijer-G function [34, Eq.(9.301)].

Proof: See Appendix A.3.

Lemma 2.5. Conditioned on $\mathcal{E}_\nu, \nu \in \{\mathrm{T}, \mathrm{A}\}$, the Laplace transform of the aerial interference is given by

$$\begin{aligned} \mathcal{L}_{I_A|\mathcal{E}_\nu}(s) &= \sum_{i=0}^{N'} \binom{N'}{i} \left(\frac{2 m_A^{m_A} (s P_A B_A \eta_A)^{-m_A}}{\alpha_A \Gamma(m_A)(d^2 - r^2)}\right)^{N'} \\ &\times \left[q_{\mathrm{A}} \left(\Omega(d, G_A) - \Omega(\tau_{A|\mathcal{E}_\nu}(r), G_A)\right)\right]^{N'-i} \\ &\times \left[(1-q_{\mathrm{A}}) \left(\Omega(d, g_A) - \Omega(\tau_{A|\mathcal{E}_\nu}(r), g_A)\right)\right]^{i}, \end{aligned} \tag{2.17}$$

where $\Omega[\cdot,\cdot]$ is given by

$$\Omega(\mathbf{x},\mathbf{g}) = \frac{\mathbf{x}^{\alpha_A m_A + 2}}{\mathbf{g}^{m_A}} \mathrm{G}_{2,2}^{1,2}\left[\frac{\mathbf{x}^{\alpha_A} m_A}{\mathbf{g} s P_A B_A \eta_A}\middle| \begin{matrix} 1-m_A-\frac{2}{\alpha_A}, 1-m_A \\ 0, -m_A-\frac{2}{\alpha_A} \end{matrix}\right]. \tag{2.18}$$

Proof: See Appendix A.4.

2.3.6 Coverage Probability

The coverage probability is defined as the probability that the SIR at the typical aerial user exceeds a predetermined threshold T. The following theorem presents the coverage probability in terms of the Laplace transform of the terrestrial and aerial interference powers.

Theorem 2.6. *The downlink coverage probability at the typical aerial user is given by*

$$\begin{aligned} \mathcal{C} &= \sum_{\nu \in \{\mathrm{T},\mathrm{A}\}} \sum_{k=0}^{m_\nu - 1} \mathcal{A}_\nu \frac{(-1)^k}{k!} \left(\frac{m_\nu T}{\mu_\nu}\right)^k \\ &\times \int_{r \in \Re_\nu} r^{k\alpha_\nu} \left[\frac{\partial^k}{\partial s^k} \mathcal{L}_{I|\mathcal{E}_\nu}(s)\right]_{s = \frac{m_\nu T r^{\alpha_\nu}}{\mu_\nu}} f_{\tilde{R}_\nu|\mathcal{E}_\nu}(r) dr, \end{aligned} \tag{2.19}$$

where $\mathcal{L}_{I|\mathcal{E}_\nu}(s) = \mathcal{L}_{I_T|\mathcal{E}_\nu}(s) \times \mathcal{L}_{I_A|\mathcal{E}_\nu}(s)$.

Proof: See Appendix A.5.

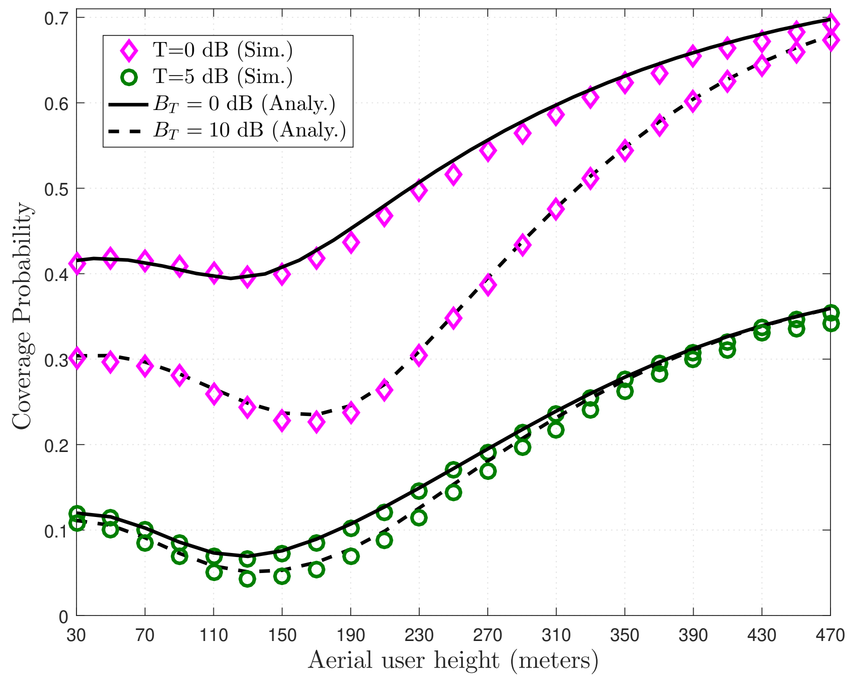

Fig. 2.1: Coverage probability versus the aerial user height ($h_{\text{A}} = 500$ meters).

Table 2.2: Parameters values

Parameter	Value	Parameter	Value
(P_T, P_A)	(33, 30) dBm	(m_T, m_A)	(2,2)
T	5 dB	h_{T}	25 meters
r_{D}	2 km	N	10
q_{A}	0.05	(η_T, η_A)	(-3, -1) dB
(α_T, α_A)	(2.5, 2)	$\lambda_{\text{T}}/\text{km}^2$	5

2.4 Simulation Results

In this section, we validate the analytical expression of the coverage probability through Monte Carlo simulations. We also investigate the impact of several system parameters on the network performance. Table 2.2 summarizes the simulation parameters unless stated otherwise.

Fig. 2.1 shows the coverage probability versus the aerial user height for different terrestrial bias factors. Clearly, the closed-form expression in (2.19) matches the simulations

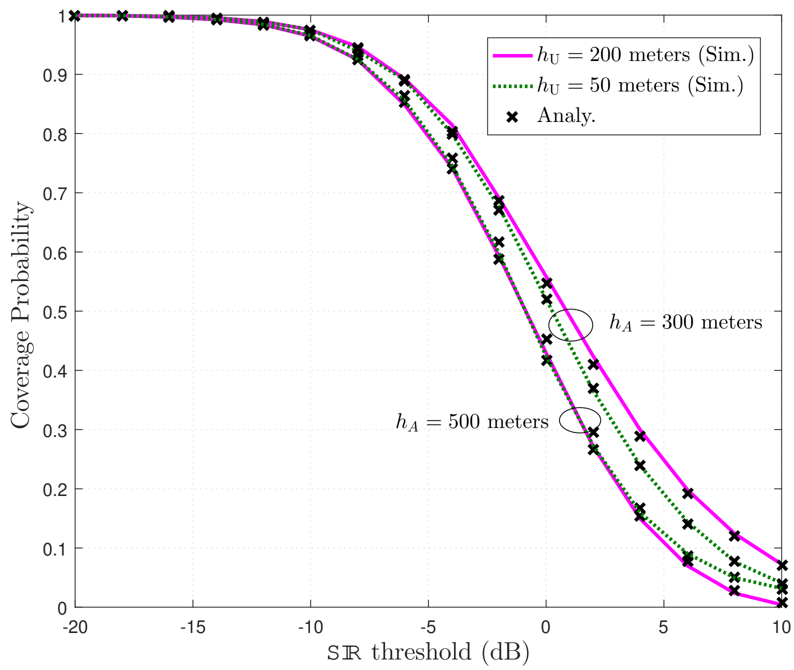

Fig. 2.2: Coverage probability versus SIR threshold.

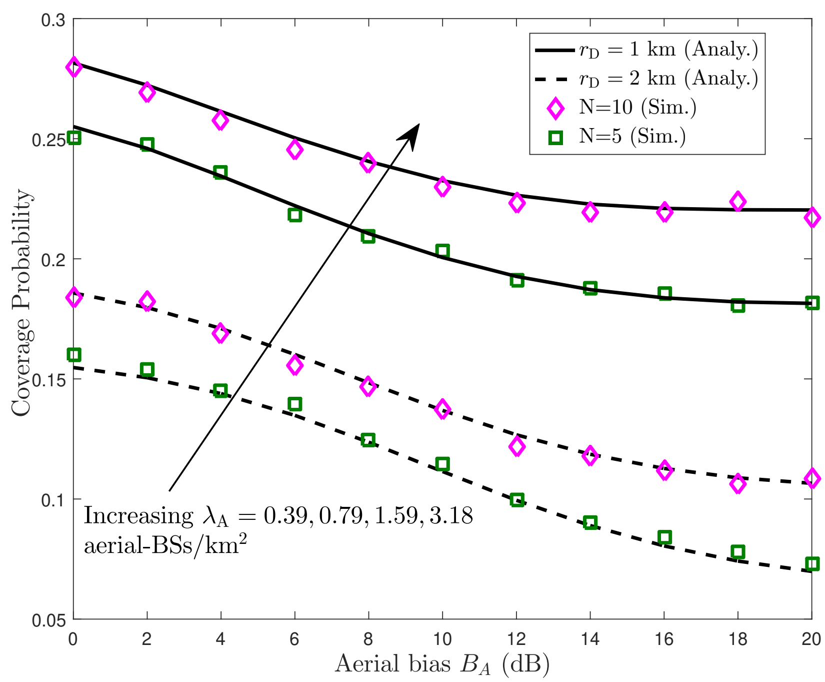

Fig. 2.3: Coverage probability versus the aerial bias factor ($h_{\mathrm{U}} = 50$ meters and $h_{\mathrm{A}} = 300$ meters).

very closely. As it can be noticed, the coverage probability decreases as $h_{\rm U}$ increases which can be explained by the fact that the terrestrial interference increases at a larger rate than the increase in the desired signal. With a further increase in $h_{\rm U}$, the coverage probability starts to increase since the terrestrial interference decreases substantially due to the large path-losses while the desired signal, which is mainly received from an aerial-BS, increases. Note that although the aerial user becomes closer to the aerial-BSs as its height increases, the aerial interference does not increase at the same rate as the desired signal from the serving aerial-BS due to the beamforming technique. Finally, increasing the terrestrial bias deteriorates the coverage probability and also shifts its minimum. Intuitively, biasing the association in favor of terrestrial-BSs may force the typical aerial user to be associated with a terrestrial-BS they may not guarantee the strongest SIR which results in decreasing the the coverage probability.

In Fig. 2.2, we show the coverage probability versus the SIR thresholds for different heights of the aerial user. Overall, deploying the aerial-BSs at low heights has a positive impact on the coverage probability. Moreover, we can notice that deploying the aerial user at high heights does not always lead to a better coverage probability. This substantiates more the trend shown in Fig. 2.1 where a lower height can guarantee a better coverage probability than a higher height.

The impacts of the number of aerial-BSs and the area radius $r_{\rm D}$ on the coverage probability are shown in Fig. 2.3 for different aerial bias factors . As it can be observed, increasing the density of aerial-BSs, i.e., increasing $\lambda_{\rm A} = \frac{N}{\pi r_{\rm D}^2}$ (aerial-BS/km^2), improves the coverage probability substantially. This is because a denser network of aerial-BSs improves the desired signal received from an aerial-BS at a higher rate than the increase in the aerial interference because of the beamforming technique that keeps the aerial interference at a low level. Similar to the outcome in Fig. 2.2, biasing the association in favor of aerial-BSs decreases the coverage probability due to extending the aerial interference range.

2.5 Conclusion

In this Chapter, we developed analytical framework to analyze the coverage probability for an aerial user in the VHetNet. The results reveal that the coverage probability highly depends on the aerial user's height. Furthermore, biasing the association in favor of the terrestrial-BSs or aerial-BSs extends the range of the interference which deteriorates the SIR and thus, the coverage probability. Moreover, the bias factor should be optimized to increase the SIR. Finally, the consideration of LoS and NLoS transmissions in C2A channel may affect the overall performance of the aerial user. Thus, we investigate a more realistic system model incorporating the occurrence of both LoS and NLoS links in C2A channels.

Chapter 3

Downlink Coverage and Rate Analysis of an Aerial User in Vertical Heterogeneous Networks (VHetNets) with LoS/NLoS transmissions

3.1 Introduction

UAVs (also referred to as drones) have drawn a great deal in the reserach community in recent years due to their flexibility and cost effectiveness in executing a range of applications, including search-and-rescue missions, aerial imaging, surveillance, and package-delivery, to name few [19]. To accommodate such high-capacity and demanding scenarios, ubiquitous coverage for UAVs is becoming crucial for delivering ultra-reliable and low-latency real-time communications [35, 36]. On this point, it may be worth mentioning that 3GPP in its recent report [37] discussed the great potential of UAVs for providing cellular connectivity

This work has been published in IEEE Transactions on Wireless Communications: **N. Cherif**, M. Alzenad, H. Yanikomeroglu, and A. Yongacoglu, "Downlink coverage and rate analysis of an aerial user in vertical heterogeneous networks (VHetNets)", *IEEE Transactions on Wireless Communications*, vol. 20, no. 3, pp. 1501-1516, March 2021.

in 5G networks. More specifically, the report investigated the communication needs of UAVs (referred to as on-board radio access nodes (UxNB) in [37]). Connected with this, a new paradigm has recently emerged where existing cellular networks (e.g., Long Term Evolution (LTE) networks) and future cellular networks (5G and beyond) can be re-utilized to provide cellular connectivity to UAVs (aerial users) [20]. Indeed, some field trials have been carried out to substantiate the feasibility of terrestrial networks for supporting aerial user communications [38]. The authors of [39], for instance, provided a comprehensive study of the potential of terrestrial base stations (terrestrial-BSs) and aerial base stations (aerial-BSs) in providing cellular coverage to aerial users based on 4G deployment. Besides the multitude of applications where UAVs are deployed as aerial users, UAVs can also be equipped with mounted antennas (i.e., as aerial-BSs) to provide cellular connectivity in case of disasters where the terrestrial network is in failure [40, 41]. Also, significantly, aerial-BSs can be deployed to support terrestrial network connectivity for high-capacity demands, such as concerts and sporting events. Due to the nature of temporary spikes in throughput demand, deploying aerial-BSs is the fastest and most cost-effective solution, compared to terrestrial-BSs [21, 22, 42–44]. Aerial-BSs have also been investigated as a promising solution for providing pervasive cellular connectivity in remote areas where the installation of conventional terrestrial network infrastructure is deemed challenging [23]. Clearly, the deployment of aerial users is imminent due to their flexibility and the great improvements of their payload capacity and extended flight duration. However, the performance of aerial users in terms of coverage and achievable throughput have not received much attention in the literature on integrated aerial and terrestrial networks (i.e., vertical heterogeneous networks or VHetNets) [15, 16, 44, 45]. In this chapter, we leverage tools from stochastic geometry to derive closed-form expressions for the downlink coverage and achievable rate of a typical aerial user in VHetNets under the assumptions of a 2-D infinite terrestrial network (terrestrial-BSs distributed over an infinite 2-D region with a certain density) and a 2-D finite aerial network. The results provide some interesting insights for the future deployment of aerial users/BSs.

3.1.1 Motivation and Related Work

Due to the emerging applications of UAVs as aerial-BSs and aerial users, the performance of VHetNets involving aerial and terrestrial users have attracted a great deal of interest. While the research community has extensively studied the efficiency of deploying UAVs as aerial-BSs [15, 26, 46, 47], the study of aerial users in terms of coverage probability and achievable rates has been lacking [10, 11, 38, 48]. For instance, the authors in [38] presented a non-orthogonal multiple access (NOMA) technique for uplink communications between aerial users and terrestrial-BSs. In [49], the authors investigated interference-aware path planning for aerial users using a deep reinforcement learning algorithm. Moreover, the work in [38] tackled the interference problem in aerial communications. A thorough comparison between the existing network infrastructure and futuristic deployment scenarios involving massive multiple-input multiple-output (MIMO) systems on the performance of aerial users was studied in [48]. While both [38] and [48] focused on terrestrial-BSs as servers for aerial users, neither explored the opportunity of deploying aerial-BSs for the cellular connectivity of aerial users.

Based on the tools of stochastic geometry, the authors in [11] and [10] investigated the feasibility of serving aerial and terrestrial users with a terrestrial wireless network. The authors claimed that the line-of-sight (LoS) condition between aerial users and terrestrial-BSs degrades the signal-to-interference-and-noise ratio SINR at the terrestrial users due to the strong interference signals received from the LoS aerial users. The same authors also presented several tuning parameters to combat these strong interference signals. However, they did not consider the possibility of using aerial-BSs capable of serving aerial users in the event of a congested terrestrial wireless network.

While the PPP assumption has become the baseline for modeling the locations of terrestrial-BSs, it is not suitable for modeling aerial networks, especially those with a small number of aerial-BSs deployed over a limited area. Since the BPP was adopted to model ad hoc terrestrial networks with a given number of nodes distributed over a circular area [24, 25], it presents a reasonable model for aerial networks while also assuring the tractability of mathematical analysis. It is noteworthy that the deployment of BSs (terrestrial or aerial) is not random in practice. However, by assuming BPP aerial network, the mathematical analysis remains tractable. For instance, the work in [26] was the first to consider a BPP model for aerial networks. In this work, the links between terrestrial users and aerial-BSs were assumed to be in LoS condition (non-LoS (NLoS) links were not considered). Such an assumption may not be applicable to aerial-BSs operating at very low heights and/or in dense environments due to the high likelihood of NLoS occurrences in these scenarios. In addition, the work in [26] limited the association of terrestrial users to only aerial-BSs, and it did not consider the possibility of the terrestrial user being served by a nearby terrestrial-BS that would provide a better channel condition than that provided by an aerial-BS, if there were one. Similar to the authors in [10], the authors in [27] investigated the opportunity of reusing existing terrestrial networks to serve aerial users. Their work suggested several interference mitigation techniques both in the uplink and downlink transmissions in order to maintain an acceptable performance of the terrestrial network for both terrestrial and aerial users. In [9], the use of coordinated multi-point transmissions to provide seamless cellular connectivity for aerial users was studied. In the same work, clustered small cell BSs were considered for serving aerial users in content-caching architecture, where popularly requested content was cached for aerial users which could then be transmitted to terrestrial users. However, the work was limited to scenarios where terrestrial-BSs did not coexist with aerial-BSs. The authors in [16] proposed a framework to analyze the coverage and rate of a VHetNet. Yet the analysis was exclusively for a typical terrestrial user; so it is not applicable for aerial users.

In Table 3.1, we summarize the stochastic geometry-based works in VHetNets in terms of characteristics for terrestrial and aerial networks, C2A transmissions link type, derived performance, and whether they account for aerial users. It may be worth mentioning that aerial-BSs can serve terrestrial users along with their aerial counterparts. However, in this work, we focus on filling the gap in the literature by investigating only the aerial user's performance in a VHetNet setup.

3.1.2 Contributions

The contributions of this Chapter can be summarized as follows:

Table 3.1: The main relevant stochastic geometry-based works on VHetNets

Ref.	Aerial network	Terrestrial network	C2A links model	Coverage prob.	Rate	Aerial user
[44]	Finite 2-D BPP	Infinite 2-D PPP	LoS links	✓	✗	✓
[16]	Infinite 2-D PPP	N/A	LoS/NLoS links	✓	✓	✗
[15]	Infinite 2-D PPP	Infinite 2-D PPP	LoS/NLoS links	✓	✓	✗
[26]	Finite 2-D BPP	N/A	LoS links	✓	✗	✗
[11]	N/A	Infinite 2-D PPP	LoS/NLoS links	✓	✓	✓
[10]	N/A	Infinite 2-D PPP	LoS/NLoS links	✓	✗	✓
[9]	N/A	Infinite 2-D PPP	LoS/NLoS links	✓	✓	✓
[50]	Single aerial-BS	Single terrestrial-BS	LoS/NLoS links	✓	✗	✗
This work	Finite 2-D PPP	Infinite 2-D PPP	LoS/NLoS links	✓	✓	✓

- We propose a novel framework to analyze the downlink coverage and rate of an aerial user served by a VHetNet comprising of aerial-BSs and terrestrial-BSs. The model consists of terrestrial-BSs that follow an infinite 2-D PPP and aerial-BSs that follow a finite 2-D BPP deployed at a particular height above the ground [26]. We model the C2A links according to the general framework provided by the International Telecommunications Union (ITU) in its recommendation report [51], which incorporates LoS and NLoS transmissions occurring according to a given probability. By contrast, the air-to-air (A2A) channels are assumed to be in LoS condition due to the absence of obstacles between the aerial user and aerial-BSs. In order to alleviate the strong interference signals received from the aerial-BSs, we incorporate directional beamforming at the aerial-BSs, where the interfering main beam of the aerial-BS is directed toward the typical aerial user with a certain probability depending on its antenna beamwidth. Two spectrum sharing policies between aerial-BSs and terrestrial-BSs (referred to as orthogonal spectrum sharing (OSS) and non-OSS (N-OSS)) are considered.

- Since the expression of the LoS probability of C2A links is difficult to use, and the widely used air-to-ground (A2G) model in [46] and [52] was exclusively developed for terrestrial users, we derive an easy-to-use compact exponential function as an approximation using curve fitting. We subsequently show that the obtained simple LoS probability matches perfectly with the ITU model in [51].

- We derive exact and approximate expressions for the coverage probability and rate in terms of the Laplace transform of interference power, and we show that the derived expressions match the simulations perfectly.

- Under the assumption that there are only LoS C2A links (no NLoS transmissions), closed-form expressions for the aerial user association probabilities and the Laplace transform of the terrestrial interference power are derived.

- The mathematical analysis of the interference received from the aerial-BSs is challenging, especially because of the beamforming that directs the main beam of the aerial-BS toward the typical aerial user with a certain probability. This assumption results in two dependent tiers of aerial-BSs, where the number of aerial-BSs in each tier depends on the other tier. Based on this setup, we derive an exact expression for the Laplace transform of the interference received from aerial-BSs in terms of the Meijer-G function. To the best of our knowledge, there are no existing studies that present a closed-form expression for the interference received from aerial-BSs. In fact, closed-form expressions are often presented as integral expressions [26]. In this case, the derived closed-form expression simplifies the evaluation of the expressions

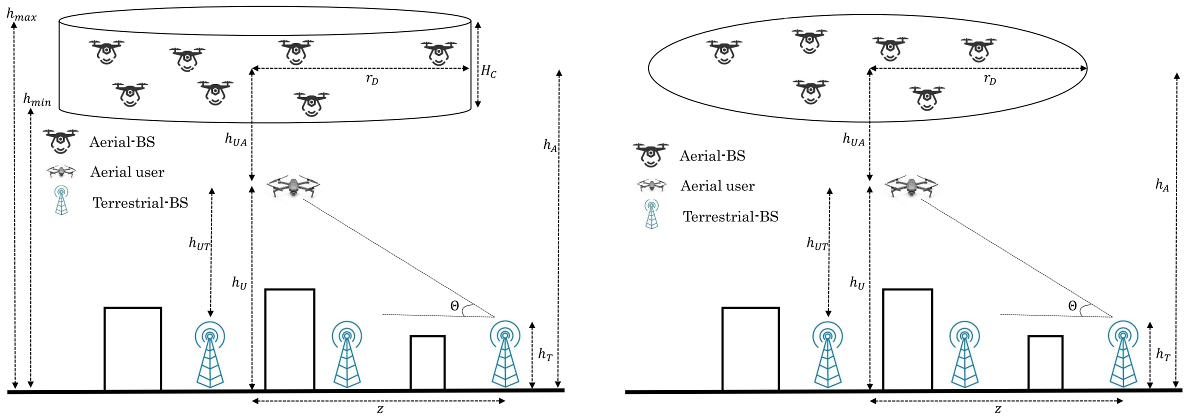

(a) VHetNet with 3-D BPP aerial network: N aerial-BSs are uniformly distributed within a finite cylinder with height $\mathrm{H_C}$ and radius r_D

(b) VHetNet with 2-D BPP aerial network: N aerial-BSs are uniformly distributed over a finite disc with height h_A and radius r_D

Fig. 3.1: VHetNet with terrestrial-BSs, aerial-BSs, and aerial users.

of the coverage probability and rate.

3.2 System Model

We assume a network of single tier terrestrial-BSs, denoted by Φ_T, uniformly distributed at ground level (i.e., terrestrial-BSs follow PPP) with density λ_T [terrestrial-BSs/km^2] and height h_T [1]. Since in practice, aerial-BSs can hover at different heights, we start by assuming that a finite number of aerial-BSs, N, hovers at different heights confined between minimum and maximum heights, h_min and h_max, respectively, as shown in Fig. 3.1(a). We also assume that N aerial-BSs are uniformly distributed within a cylinder with a radius r_D and a height $\mathrm{H_C}$ to form a BPP with a center $(0, 0, \frac{h_\mathrm{min}+h_\mathrm{max}}{2})$. Introducing such a randomness to the height of aerial-BSs makes the distance distributions between a typical aerial user and any aerial-BS difficult to derive without much of a useful outcome. Since it has been shown in [26] that the performance of a 3-D BPP aerial network matches perfectly

[1]Although terrestrial-BSs are often a mix of macro-, micro-, and pico-BSs, we only consider a single tier terrestrial network composed of macro-BS since macro-BSs transmit at higher powers than other terrestrial-BSs and are thus more suitable for providing wireless connectivity to aerial users.

that of 2-D BPP aerial-BSs deployed at an average height, $h_{\mathrm{A}} = \frac{h_{\min}+h_{\max}}{2}$, we assume in our framework, N aerial-BSs hovering at a height h_{A} from the ground and uniformly distributed over a disc with a center $(0, 0, h_{\mathrm{A}})$ and radius r_{D}, as illustrated in Fig. 3.1(b). So although we place the aerial-BSs at the same height h_{A}, our framework is still applicable for aerial-BSs with different heights. Simulation results will substantiate the correctness of this assumption. It may be worth mentioning that the deployment of BSs (either terrestrial of aerial) is not random in practice. However, the point process assumption enables the tractability of the analysis of the network using stochastic geometry tools while tracking realistic BS deployment in practice [16, 26, 32]. In this Chapter, our focus is mainly on an aerial user's performance in VHetNets. The transmit power of the terrestrial-BSs and aerial-BSs are assumed to be P_T and P_A, respectively. Finally, we consider a typical aerial user hovering at a height h_{U}, where $h_{\mathrm{T}} < h_{\mathrm{U}} < h_{\mathrm{A}}$.

3.2.1 Cellular-to-Air Channel

The widely used A2G channel model proposed in [52] and [46] is not applicable to aerial users because it was developed for terrestrial users positioned at heights of 1.5 meters, while our system model involves terrestrial-BSs positioned at much greater heights (e.g., 30 meters for macro-BSs) [53]. Therefore, in this section, we develop a more tractable expression for the LoS probability. According to the ITU recommendation report [51], the probability of an LoS between a transmitter and receiver with heights h_{TX} and h_{RX}, respectively, is given by [51]

$$P_{\mathrm{L}}(z) = \prod_{n=0}^{m} \left[1 - \exp\left(- \frac{\left[h_{\mathrm{TX}} - \frac{\left(n+\frac{1}{2}\right)(h_{\mathrm{TX}} - h_{\mathrm{RX}})}{m+1} \right]^2}{2\delta^2} \right) \right], \tag{3.1}$$

where z denotes the horizontal distance between the transmitter and the receiver on the xy plane, and $m = \lfloor \left(\frac{z\sqrt{\alpha\beta}}{1000} - 1 \right) \rfloor$ where α, β, and δ are environment-related coefficients given in Table I in [54].

As we can see in (3.1), the LoS probability $P_{\mathrm{L}}(z)$ is not a continuous function of z which makes the analysis intractable. Similar to the work in [52] and [46], we simplify

Table 3.2: Approximated LoS probabilities for different environments

Environment	$\mathbf{h_T}$ **(meters)**	**a**	**b**	**c**
Suburban	30	1	6.581	1
Urban	19	1	0.151	1
Dense urban	25	1	0.106	1
Highrise urban	62	1.124	0.049	1.024

(3.1) to a more tractable exponential function under some assumptions. This can be done by approximating the curve of $P_L(z)$ in (3.1) by a continuous exponential function of the elevation angle θ for a fixed terrestrial-BS height. From Fig. 3.1(b), the horizontal distance z can be written as $z = (h_U - h_T)/\tan(\theta)$. Comparing the parameters in (3.1) with the parameters of the system model presented in Fig. 3.1(b), we have, $h_{TX} = h_T$ and $h_{RX} = h_U$. Notably, the resulting plot of the expression in (3.1) will smooth for large values of h_U (we used $h_U = 10,000$ meters in our simulation). Thus, the probability of an LoS condition becomes a continuous function of the elevation angle θ and the environment parameters. In Fig. 3.2, we plotted the ITU LoS probability for four different environments with a solid red line. As we can see, the trend of the curves can be closely approximated to a continuous exponential function. Using the Matlab® feature 'Curve Fitting', we have

$$P_L(\theta) = -a \exp(-b\theta) + c, \tag{3.2}$$

where $\theta = \tan^{-1}\left(\frac{h_U - h_T}{z}\right)$, and a, b, and c are parameters that depend on the environment and height of the terrestrial-BSs. The LoS probability model used in this Chapter is presented in Table 3.2. Indeed, the LoS probability derived in (3.2) for C2A links presents a compact expression that depends only on the environment and the height of the aerial user in its elevation angle for a given terrestrial-BS height.

Fig. 3.2 shows the LoS probability using the original ITU model in (3.1) and the approximated expression in (3.2) for different environments. As we can see, the approximated LoS expression in (3.2) matches the original ITU model very closely. Each C2A link between the aerial user, which is at a height $h_{UT} = h_U - h_T$ from the terrestrial-BS, is assumed to

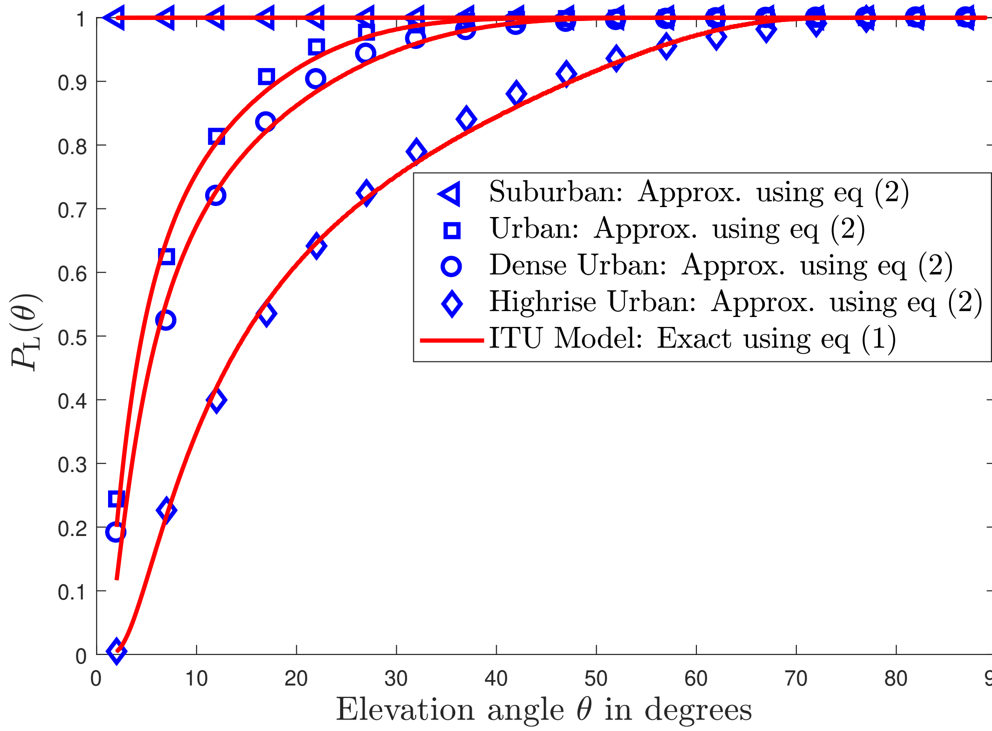

Fig. 3.2: LoS probability versus the elevation angle θ for different environments.

be either an LoS or NLoS link with an LoS probability $P_{\rm L}(z)$ given by

$$P_{\rm L}(z) = -a \exp\left(-b \tan^{-1}\left(\frac{h_{\rm UT}}{z}\right)\right) + c. \tag{3.3}$$

Finally, the NLoS probability is given by $P_{\rm N}(z) = 1 - P_{\rm L}(z)$.

Due to the fact that the aerial user is either in an LoS or NLoS condition with each terrestrial-BS [15], the set of terrestrial-BSs can be broken down into two independent inhomogeneous PPPs, where the LoS terrestrial-BSs form a subset $\Phi_{\rm L}$ with density $\lambda_{\rm T} P_{\rm L}(z)$, while the NLoS terrestrial-BSs form a subset $\Phi_{\rm N}$ with density $\lambda_{\rm T} P_{\rm N}(z)$ [55]. We assume that the LoS and NLoS C2A channels experience Nakagami-m fading with different m parameters, and therefore the received power from the terrestrial-BS located at point x_j is Gamma-distributed, i.e., ${\rm H}_{\nu}^{x_j} \sim {\rm Gamma}\left(m_\nu, \frac{1}{m_\nu}\right)$, where m_ν, $\nu \in \{{\rm L}, {\rm N}\}$ denotes the fading parameters for the LoS and NLoS C2A links. The PDF of the Gamma-distributed channel gain is given by [15]

$$f_{{\rm H}_{\nu}^{x_j}}(x) = \frac{m_\nu^{m_\nu} x^{m_\nu x}}{\Gamma(m_\nu)} e^{-m_\nu x}, \quad \nu \in \{{\rm L}, {\rm N}\}, \tag{3.4}$$

where $\Gamma(\cdot)$ is the Gamma function defined as $\Gamma(m_\nu) = \int_0^\infty t^{m_\nu - 1} e^{-t} dt$.

The received power at the typical aerial user from a terrestrial-BS located at x_j is given by

$$P_{r,j}^{\nu} = P_T \eta_\nu G^{\mathrm{T}}(r_j) \mathrm{H}_\nu^{x_j} d_{\nu,x_j}^{-\alpha_\nu}, \quad \nu \in \{\mathrm{L}, \mathrm{N}\}, \tag{3.5}$$

where η_ν are the excess losses for the LoS and NLoS C2A links, respectively [52]. Moreover, d_{ν,x_j} denotes the distance between the typical aerial user and a terrestrial-BS from the tier $\Phi_\nu, \nu \in \{\mathrm{L}, \mathrm{N}\}$ located at x_j. α_ν, $\nu \in \{\mathrm{L}, \mathrm{N}\}$, is the path-loss coefficient. Finally, $G^{\mathrm{T}}(r_j)$ denotes the antenna directivity gain of the terrestrial-BS's antenna located at x_j and the typical aerial user, which can be written as [10]

$$G^{\mathrm{T}}(r_j) = \begin{cases} G_{\mathrm{m}}^{\mathrm{T}}, & r_j \in \mathcal{D}_{\mathrm{TBS}} \\ g_{\mathrm{s}}^{\mathrm{T}}, & r_j \notin \mathcal{D}_{\mathrm{TBS}}, \end{cases} \tag{3.6}$$

where $\mathcal{D}_{\mathrm{TBS}}$ denotes the set of all distances r_j satisfying $r_j \tan\left(\theta_t + \frac{\theta_{\mathrm{B}}^{\mathrm{T}}}{2}\right) < h_{\mathrm{U}} < h_{\mathrm{T}} - r_j \tan\left(\theta_t - \frac{\theta_{\mathrm{B}}^{\mathrm{T}}}{2}\right)$, where r_j refers to the horizontal distance separating the aerial user from the projection of the terrestrial-BS location on the xy plane, and θ_t and $\theta_{\mathrm{B}}^{\mathrm{T}}$ are the down-tilt and beamwidth angles of the terrestrial-BS's antenna. In other words, $G^{\mathrm{T}}(r_j)$ determines whether the aerial user falls within the mainlobe or sidelobe of the terrestrial-BS's antenna.

Since the terrestrial-BS antennas are typically tilted toward the ground in order to provide cellular coverage to terrestrial users [56], aerial users that hover at a greater height than the terrestrial-BS, i.e., $h_{\mathrm{T}} < h_{\mathrm{U}}$, will most likely receive signals from the terrestrial-BS antenna sidelobes. For the tractability of the analysis in this work, we assume that $G^{\mathrm{T}}(r_j) = g_{\mathrm{s}}^{\mathrm{T}}$, $\forall\, r_j$. In the simulation results section, we will provide findings to substantiate the accuracy of this assumption.

3.2.2 Air-to-Air Channel

Since the aerial user is assumed to hover above rooftops, the A2A links between the typical aerial user and the aerial-BSs are assumed to be in LoS condition [28, 29]. We also assume that the aerial-BSs employ directive beamforming to improve the SINR. As a result, the gain of the aerial-BS antenna located at x_i, denoted by G^{A}, at the typical aerial user is given by [30]

$$G^{\mathrm{A}}(d_{A,x_i}) = \begin{cases} G_{\mathrm{m}}^{\mathrm{A}}, & -\frac{\theta_{\mathrm{B}}^{\mathrm{A}}}{2} \leqslant \psi \leqslant \frac{\theta_{\mathrm{B}}^{\mathrm{A}}}{2} \\ g_{\mathrm{s}}^{\mathrm{A}}, & \text{otherwise}, \end{cases} \tag{3.7}$$

where d_{A,x_i} denotes the distance between the typical aerial user and the aerial-BS located at x_i, $G_{\mathrm{m}}^{\mathrm{A}}$ and $g_{\mathrm{s}}^{\mathrm{A}}$ are the gains of the mainlobe and sidelobe, respectively, ψ is the sector angle, and $\theta_{\mathrm{B}}^{\mathrm{A}} \in [0, 180]$ is the beamwidth in degrees [31, Fig. 3]. Thus, the received power at the aerial user from an aerial-BS located at x_i is given by

$$P_{r,i}^{A} = P_A G^{\mathrm{A}}(d_{A,x_i}) \eta_A \mathrm{H}_{\mathrm{A}}^{x_i} d_{A,x_i}^{-\alpha_A}, \tag{3.8}$$

where η_A represents the excess losses, $\mathrm{H}_{\mathrm{A}}^{x_i}$ is the Gamma-distributed channel power gain, i.e., $\mathrm{H}_{\mathrm{A}}^{x_i} \sim \text{Gamma}\left(m_A, \frac{1}{m_A}\right)$, with a fading parameter m_A, and α_A is the path-loss exponent. Unlike terrestrial-BSs whose antennas with fixed antenna patterns are deployed to serve terrestrial users, the aerial-BSs with down-tilted antennas can direct their beams toward their associated aerial users. Hence, the beamforming gain from the serving aerial-BS is always $G_{\mathrm{m}}^{\mathrm{A}}$ [31]. For the remaining interfering aerial-BSs, their main beams are not necessarily aligned with the typical aerial user since their beam orientations are uniformly distributed in $[0, 180°]$. We introduce a probability q_{A} depending on the beamwidth $\theta_{\mathrm{B}}^{\mathrm{A}}$ that quantifies the likelihood of an interfering aerial-BS's mainlobe being directed toward the typical aerial user. It follows that $q_{\mathrm{A}} = \mathbb{P}\left(G^{\mathrm{A}}(d_{A,x_i}) = G_{\mathrm{m}}^{\mathrm{A}}\right) = \frac{\theta_{\mathrm{B}}^{\mathrm{A}}}{180}$. The interfering aerial-BS gain is $g_{\mathrm{s}}^{\mathrm{A}}$ when the typical receiver is in its sidelobe direction with a probability of occurrence of $1 - q_{\mathrm{A}}$ [31, Fig. 3]. Typically, $g_{\mathrm{s}}^{\mathrm{A}}$ is 20 dB less than the mainlobe gain $G_{\mathrm{m}}^{\mathrm{A}}$ [31]. It is worth noting that realistic 3-D antenna radiation models, such as those presented in [57] and [58], can be adopted in our VHetNet's framework analysis. However, as shown above, we choose to investigate a more analytically tractable BS antenna model. Future works can focus on more realistic 3-D antenna patterns in the context of VHetNets for even more practical insights.

The typical aerial user is assumed to be served by the BS (located at point x_0) that provides the strongest *long-term averaged* received power [33]. Indeed, since the A2A links are in LoS, it is possible for a distantly located aerial-BS to offer better SINR than that of a closer terrestrial-BS due to differences in path-loss parameters. It should be noted that if the aerial user is associated with a specific tier of BS, i.e., $\{\Phi_{\mathrm{L}}, \Phi_{\mathrm{N}}, \Phi_{\mathrm{A}}\}$, the serving BS would be the nearest BS to that specific tier. Thus, by assuming that the average power of all channels is 1, i.e., $\mathbb{E}[\mathrm{H}_{\mathrm{L}}^{x_j}] = \mathbb{E}[\mathrm{H}_{\mathrm{N}}^{x_j}] = \mathbb{E}[\mathrm{H}_{\mathrm{A}}^{x_j}] = 1$ for each $x_j \in \Phi_{\mathrm{T}} \cup \Phi_{\mathrm{A}}$, the serving BS is given by

$$x_0 = \arg\max\{\mu_L R_L^{-\alpha_L}, \mu_N R_N^{-\alpha_N}, \mu_A R_A^{-\alpha_A}\}, \tag{3.9}$$

where $\mu_\nu = P_T \eta_\nu g_{\mathrm{s}}^{\mathrm{T}}$, $\nu \in \{\mathrm{L}, \mathrm{N}\}$, $\mu_A = P_A G_{\mathrm{m}}^{\mathrm{A}} \eta_A$, $R_L = \min\limits_{\forall x_j \in \Phi_{\mathrm{L}}} d_{L,x_j}$, and, $R_N = \min\limits_{\forall x_j \in \Phi_{\mathrm{L}}} d_{N,x_j}$, and $R_A = \min\limits_{\forall x_i \in \Phi_{\mathrm{A}}} d_{A,x_i}$. As a result, the SINR at the typical aerial user is given by

$$\gamma = \begin{cases} \frac{\mu_L \mathrm{H}_{\mathrm{L}}^{x_0} R_L^{-\alpha_L}}{I+\sigma^2}, & \text{if } x_0 \in \Phi_{\mathrm{L}}(\mathcal{E}_{\mathrm{L}}) \\ \frac{\mu_N \mathrm{H}_{\mathrm{N}}^{x_0} R_N^{-\alpha_N}}{I+\sigma^2}, & \text{if } x_0 \in \Phi_{\mathrm{N}}(\mathcal{E}_{\mathrm{N}}) \\ \frac{\mu_A \mathrm{H}_{\mathrm{A}}^{x_0} R_A^{-\alpha_A}}{I+\sigma^2}, & \text{if } x_0 \in \Phi_{\mathrm{A}}(\mathcal{E}_{\mathrm{A}}), \end{cases} \tag{3.10}$$

where $\mathcal{E}_\nu$, $\nu \in \{\mathrm{L}, \mathrm{N}, \mathrm{A}\}$, denotes the event that the serving BS belongs to the tier Φ_ν and σ^2 is the additive white Gaussian noise power. Finally, I refers to the aggregate interference power.

Two spectrum sharing policies between aerial-BSs and terrestrial-BSs are used: orthogonal spectrum sharing (OSS) and non-orthogonal spectrum sharing (N-OSS) [50]. OSS/N-OSS implies that aerial-BSs and terrestrial-BSs operate on the same/different frequencies. The interference I is given by

$$I = \begin{cases} I_L + I_N + I_A, & \text{N-OSS} \\ I_L + I_N, & \text{OSS}, \quad \text{if } x_0 \in \Phi_{\mathrm{L}} \cup \Phi_{\mathrm{N}} \\ I_A, & \text{OSS}, \quad \text{if } x_0 \in \Phi_{\mathrm{A}}, \end{cases} \tag{3.11}$$

where

$$I_L = \sum_{x_j \in \Phi_L \setminus x_0} \mu_L \mathrm{H}_{\mathrm{L}}^{x_j} d_{L,x_j}^{-\alpha_L}, \quad I_N = \sum_{x_j \in \Phi_N \setminus x_0} \mu_N \mathrm{H}_{\mathrm{N}}^{x_j} d_{N,x_j}^{-\alpha_N}, \text{ and, } I_A = \sum_{i=1, x_i \in \Phi_A \setminus x_0}^{N} P_A G^{\mathrm{A}}(d_{A,x_i}) \eta_A \mathrm{H}_{\mathrm{A}}^{x_i} d_{A,x_i}^{-\alpha_A}, \tag{3.12}$$

where $G^{\mathrm{A}}(d_{A,x_i}) = G_{\mathrm{m}}^{\mathrm{A}}$ with a probability of q_{A} and $G^{\mathrm{A}}(d_{A,x_i}) = g_{\mathrm{s}}^{\mathrm{A}}$ with a probability of $1 - q_{\mathrm{A}}$.

We provide the list of symbols in Table 3.3.

Table 3.3: List of symbols

Notation	Description
h_{UT}	Height of the aerial user with reference to the terrestrial-BSs
h_{UA}	Height of the aerial user with reference to the aerial-BSs
h_{U}	Height of the aerial user with reference to the ground level
$P_T,\ P_A$	Transmit power of terrestrial and aerial BSs, respectively
r_{D}	Radius of the circle where aerial-BSs are distributed
$\mathrm{H_C}$	Height of the cylinder where aerial-BSs are distributed in the 3-D setup
$\Phi_{\mathrm{T}},\ \Phi_{\mathrm{A}},\ \Phi_{\mathrm{L}},\ \Phi_{\mathrm{N}}$	Tier of terrestrial-BSs, aerial-BSs, LoS terrestrial-BSs, or NLoS terrestrial-BSs, respectively
λ_{T}	Density of terrestrial-BSs
$P_{\mathrm{L}}(\cdot),\ P_{\mathrm{N}}(\cdot)$	Probability of the aerial user being in LoS and NLoS with terrestrial-BSs, respectively
$G_{\mathrm{m}}^{\mathrm{A}},\ g_{\mathrm{s}}^{\mathrm{A}}$	Gain of the aerial-BS's antenna mainlobe and sidelobe, respectively
$G_{\mathrm{m}}^{\mathrm{T}},\ g_{\mathrm{s}}^{\mathrm{T}}$	Gain of the terrestrial-BS's antenna mainlobe and sidelobe, respectively
q_{A}	Probability that the mainlobe of the interfering aerial-BS is directed toward the aerial user
$m_L,\ m_N,\ m_A$	Nakagami-m fading parameter for LoS terrestrial-BS, NLoS terrestrial-BS, and aerial-BS, respectively
$\alpha_L,\ \alpha_N,\ \alpha_A$	Path-loss exponent parameter for LoS terrestrial-BS, NLoS terrestrial-BS, and aerial-BS, respectively
$d_{L,x_i},\ d_{N,x_i},\ d_{A,x_i}$	Distance between the aerial user and an LoS terrestrial-BS, NLoS terrestrial-BS, or aerial-BS, respectively, located at x_i
$R_L,\ R_N,\ R_A$	Distance between the aerial user and its nearest LoS terrestrial-BS, NLoS terrestrial-BS, or aerial-BS, respectively
$\tilde{R}_L,\ \tilde{R}_N,\ \tilde{R}_A$	Distance between the aerial user and its serving BS assuming the that the aerial user is associated with an LoS terrestrial-BS, NLoS terrestrial-BS, or aerial-BS, respectively
$\mathcal{E}_{\mathrm{L}},\ \mathcal{E}_{\mathrm{N}},\ \mathcal{E}_{\mathrm{A}}$	Event that describes an aerial user's serving BS as LoS terrestrial-BS, NLoS terrestrial-BS, or aerial-BS, respectively
$\mathrm{H}_{\mathrm{L}}^{x_i},\ \mathrm{H}_{\mathrm{N}}^{x_i},\ \mathrm{H}_{\mathrm{A}}^{x_i}$	Channel power gain between the aerial user and an LoS terrestrial-BS, NLoS terrestrial-BS, or aerial-BS, respectively, located at x_i
$I_L,\ I_N,\ I_A$	Interference at the aerial user from LoS terrestrial-BS, NLoS terrestrial-BS, and aerial-BS, respectively
$\mathcal{A}_{\mathrm{L}},\ \mathcal{A}_{\mathrm{N}},\ \mathcal{A}_{\mathrm{A}}$	Probability of association between aerial user and LoS terrestrial-BS, NLoS terrestrial-BS, or aerial-BS, respectively

3.3 Relevant Distance Distributions and Association Probabilities

In this section, we begin by deriving several relevant distance distributions that will be useful in deriving the association probabilities and Laplace transforms of the interference powers given in (3.11). Afterwards, simplified expressions for the association probabilities and the terrestrial interference's Laplace transforms are presented under the assumption that all C2A links are in LoS condition.

3.3.1 Distances Distributions of the Nearest BSs

In Lemma 3.1, we present the distribution of the distances between the aerial user and its nearest aerial-BS, LoS terrestrial-BS, and NLoS terrestrial-BS.

Lemma 3.1. The PDF and the CDF of $R_\nu, \nu \in \{\mathrm{L}, \mathrm{N}\}$ are given by

$$f_{R_\nu}(r) = 2\pi\lambda_{\mathrm{T}} r P_\nu\left(\sqrt{r^2 - h_{\mathrm{UT}}^2}\right) \exp\left(-2\pi\lambda_{\mathrm{T}} \int_{h_{\mathrm{UT}}}^{r} t P_\nu\left(\sqrt{t^2 - h_{\mathrm{UT}}^2}\right) dt\right), r \geqslant h_{\mathrm{UT}} \quad (3.13)$$

$$F_{R_\nu}(r) = 1 - \exp\left(-2\pi\lambda_{\mathrm{T}} \int_{h_{\mathrm{UT}}}^{r} t P_\nu\left(\sqrt{t^2 - h_{\mathrm{UT}}^2}\right) dt\right), \qquad r \geqslant h_{\mathrm{UT}}. \quad (3.14)$$

Proof: See Appendix B.1.

The PDF and the CDF of R_A are given by [26, eq. (7)]

$$f_{R_A}(r) = N\left(\frac{2r}{r_{\mathrm{D}}^2}\right)\left(\frac{d^2 - r^2}{r_{\mathrm{D}}^2}\right)^{N-1}, h_{\mathrm{UA}} \leqslant r \leqslant d \quad (3.15)$$

$$F_{R_A}(r) = \begin{cases} 0, & r \leqslant h_{\mathrm{UA}} \\ 1 - \left(\frac{d^2 - r^2}{r_{\mathrm{D}}^2}\right)^N, & h_{\mathrm{UA}} \leqslant r \leqslant d \\ 1, & r \geqslant d, \end{cases} \quad (3.16)$$

where $d = \sqrt{r_{\mathrm{D}}^2 + h_{\mathrm{UA}}^2}$.

3.3.2 Distances of the Nearest Interfering BSs

In Table 3.4, we summarize the distances $\tau_{\nu|\mathcal{E}_\nu}(r), \nu \in \{\mathrm{L}, \mathrm{N}, \mathrm{A}\}$ between the typical aerial user and the nearest interfering BSs from the three tiers $\Phi_{\mathrm{L}}, \Phi_{\mathrm{N}}, \Phi_{\mathrm{A}}$ where the serving BS

Table 3.4: Interferer distances

Condition	$\tau_{L\|\mathcal{E}_\nu}(r)$	$\tau_{N\|\mathcal{E}_\nu}(r)$	$\tau_{A\|\mathcal{E}_\nu}(r)$	N'
$\mathcal{E}_{\rm L}$ ($x_0 \in \Phi_{\rm L}$)	r	$\begin{cases} h_{\rm UT}, & h_{\rm UT} \leqslant r \leqslant \zeta_{\rm N}^{\rm L} \\ \left(\frac{\eta_N r^{\alpha_L}}{\eta_L}\right)^{\frac{1}{\alpha_N}}, & r \geqslant \zeta_{\rm N}^{\rm L}, \end{cases}$ where $\zeta_{\rm N}^{\rm L} = \left(\frac{\eta_L h_{\rm UT}^{\alpha_N}}{\eta_N}\right)^{\frac{1}{\alpha_L}}$	$\begin{cases} h_{\rm UA}, & h_{\rm UT} \leqslant \zeta_{\rm A}^{\rm L}(h_{\rm UA}) \\ \left(\frac{\mu_A r^{\alpha_L}}{\mu_L}\right)^{\frac{1}{\alpha_A}}, & \zeta_{\rm A}^{\rm L}(h_{\rm UA}) \leqslant r \leqslant \zeta_{\rm A}^{\rm L}(d), \end{cases}$ where $\zeta_{\rm A}^{\rm L}(x) = \left(\frac{\mu_L x^{\alpha_A}}{\mu_A}\right)^{\frac{1}{\alpha_L}}$	N
$\mathcal{E}_{\rm N}$ ($x_0 \in \Phi_{\rm N}$)	$\left(\frac{\mu_L r^{\alpha_N}}{\mu_N}\right)^{\frac{1}{\alpha_L}}$	r	$h_{\rm UA}$	N
$\mathcal{E}_{\rm A}$ ($x_0 \in \Phi_{\rm A}$)	$\begin{cases} h_{\rm UT}, & h_{\rm UA} \leqslant r \leqslant \zeta_{\rm L}^{\rm A} \\ \left(\frac{\mu_L r^{\alpha_A}}{\mu_A}\right)^{\frac{1}{\alpha_L}}, & \zeta_{\rm L}^{\rm A} \leqslant r \leqslant d. \end{cases}$ where $\zeta_{\rm L}^{\rm A} = \left(\frac{\mu_A h_{\rm UT}^{\alpha_L}}{\mu_L}\right)^{\frac{1}{\alpha_A}}$	$h_{\rm UT}$	r	N-1

is at a distance of r. More specifically, the set of distances where $r \geqslant \tau_{\nu|\mathcal{E}_\nu}(r)$ quantify the region over which the interfering BSs from Φ_ν exist. Note that N' in Table 3.4 quantifies the number of interfering aerial-BSs.

3.3.3 Association Probabilities

As stated previously, the typical aerial user is associated with an aerial-BS, LoS terrestrial-BS, or NLoS terrestrial-BS with probabilities given in the following lemmas.

Lemma 3.2. The probability that the typical aerial user is associated with an LoS terrestrial-BS is given by

$$\mathcal{A}_{\rm L} = \Xi_{\rm N}^{\rm L} \times \Xi_{\rm A}^{\rm L}, \tag{3.17}$$

where

$$\Xi_{\rm N}^{\rm L} = \begin{cases} F_{R_L}(\zeta_{\rm N}^{\rm L}) + \int_{\zeta_{\rm N}^{\rm L}}^{\infty} F_{R_N}^{(c)}\left(\left(\frac{\eta_N r^{\alpha_L}}{\eta_L}\right)^{\frac{1}{\alpha_N}}\right) f_{R_L}(r)dr, & h_{\rm UT} \leqslant \zeta_{\rm N}^{\rm L} \\ \int_{\zeta_{\rm N}^{\rm L}}^{\infty} F_{R_N}^{(c)}\left(\left(\frac{\eta_N r^{\alpha_L}}{\eta_L}\right)^{\frac{1}{\alpha_N}}\right) f_{R_L}(r)dr, & h_{\rm UT} \geqslant \zeta_{\rm N}^{\rm L}, \end{cases} \tag{3.18}$$

and,

$$\Xi_{\rm A}^{\rm L} = \begin{cases} 1 + \int_{\zeta}^{\zeta_{\rm A}^{\rm L}(d)} F_{R_A}^{(c)}\left(\left(\frac{\mu_A r^{\alpha_L}}{\mu_L}\right)^{\frac{1}{\alpha_A}}\right) f_{R_L}(r)dr - F_{R_L}^{(c)}(\zeta), & h_{\rm UT} \leqslant \zeta_{\rm A}^{\rm L}(d) \\ 0, & h_{\rm UT} \geqslant \zeta_{\rm A}^{\rm L}(d), \end{cases} \tag{3.19}$$

with $\zeta = \arg\max\left\{h_{\rm UT}, \zeta_{\rm A}^{\rm L}(h_{\rm UA})\right\}$.

Proof: See Appendix B.2.

Lemma 3.3. The probability of the typical aerial user being associated with an aerial-BS is given by

$$\mathcal{A}_{\mathrm{A}} = \Xi_{\mathrm{N}}^{\mathrm{A}} \times \Xi_{\mathrm{L}}^{\mathrm{A}}, \tag{3.20}$$

where

$$\Xi_{\mathrm{N}}^{\mathrm{A}} = \begin{cases} \int_{h_{\mathrm{UA}}}^{d} F_{R_N}^{(c)}\left(\left(\frac{\mu_N r^{\alpha_A}}{\mu_A}\right)^{\frac{1}{\alpha_N}}\right) f_{R_A}(r)dr, & \zeta_{\mathrm{N}}^{\mathrm{A}} \leqslant h_{\mathrm{UA}} \\ F_{R_A}(\zeta_{\mathrm{N}}^{\mathrm{A}}) + \int_{\zeta_{\mathrm{N}}^{\mathrm{A}}}^{d} F_{R_N}^{(c)}\left(\left(\frac{\mu_N r^{\alpha_A}}{\mu_A}\right)^{\frac{1}{\alpha_N}}\right) f_{R_A}(r)dr, & h_{\mathrm{UA}} \leqslant \zeta_{\mathrm{N}}^{\mathrm{A}} \leqslant d \\ 1, & \zeta_{\mathrm{N}}^{\mathrm{A}} \geqslant d, \end{cases} \tag{3.21}$$

where $\zeta_{\mathrm{N}}^{\mathrm{A}} = \left(\frac{\mu_A h_{\mathrm{UT}}^{\alpha_N}}{\mu_N}\right)^{\frac{1}{\alpha_A}}$, and,

$$\Xi_{\mathrm{L}}^{\mathrm{A}} = \begin{cases} \int_{h_{\mathrm{UA}}}^{d} F_{R_L}^{(c)}\left(\left(\frac{\mu_L r^{\alpha_A}}{\mu_A}\right)^{\frac{1}{\alpha_L}}\right) f_{R_A}(r)dr, & \zeta_{\mathrm{L}}^{\mathrm{A}} \leqslant h_{\mathrm{UA}} \\ F_{R_A}(\zeta_{\mathrm{L}}^{\mathrm{A}}) + \int_{\zeta_{\mathrm{L}}^{\mathrm{A}}}^{d} F_{R_L}^{(c)}\left(\left(\frac{\mu_L r^{\alpha_A}}{\mu_A}\right)^{\frac{1}{\alpha_L}}\right) f_{R_A}(r)dr, & h_{\mathrm{UA}} \leqslant \zeta_{\mathrm{L}}^{\mathrm{A}} \leqslant d \\ 1, & \zeta_{\mathrm{L}}^{\mathrm{A}} \geqslant d. \end{cases} \tag{3.22}$$

Proof: The proof follows the same steps as that of Lemma 3.2; therefore, it is omitted here.

Finally, the probability of the aerial user being associated with an NLoS terrestrial-BS is given by $\mathcal{A}_{\mathrm{N}} = 1 - \mathcal{A}_{\mathrm{L}} - \mathcal{A}_{\mathrm{A}}$.

3.3.4 Conditional Distance Distributions of the Serving BS

In this section, we present the distribution of the distances between the typical aerial user and its serving BS, where the latter is an LoS terrestrial-BS, NLoS terrestrial-BS, or aerial-BS.

Lemma 3.4. Where the aerial user is associated with an LoS terrestrial-BS (i.e., the event $\mathcal{E}_{\mathrm{L}}$ occurs), the distribution of the distance $\tilde{R}_L$ between the aerial user and the serving LoS terrestrial-BS is given by

$$f_{\tilde{R}_L|\mathcal{E}_{\mathrm{L}}}(r) = \begin{cases} \frac{1}{\mathcal{A}_{\mathrm{L}}} F_{R_N}^{(c)}\left(\tau_{N|\mathcal{E}_{\mathrm{L}}}(r)\right) \times F_{R_A}^{(c)}\left(\tau_{A|\mathcal{E}_{\mathrm{L}}}(r)\right) \times f_{R_L}(r), & r \in \mathfrak{R}_{\mathrm{L}} \\ 0, & \text{otherwise}, \end{cases} \tag{3.23}$$

where $\mathfrak{R}_{\rm L} = [h_{\rm UT}, \zeta_{\rm A}^{\rm L}(d)]$. Note that according to (3.19), $\mathcal{A}_{\rm L} = 0$ outside $\mathfrak{R}_{\rm L}$.

Proof: See Appendix B.3.

Lemma 3.5. Where the aerial user is associated with an aerial-BS (i.e., the event $\mathcal{E}_{\rm A}$ occurs), the distribution of the distance $\tilde{R}_A$ between the aerial user and the serving aerial-BS is given by

$$f_{\tilde{R}_A|\mathcal{E}_{\rm A}}(r)=\begin{cases}\frac{1}{\mathcal{A}_{\rm A}} F_{R_N}^{(c)}\left(h_{\rm UT}\right) \times F_{R_L}^{(c)}\left(\tau_{L|\mathcal{E}_{\rm A}}(r)\right) \times f_{R_A}(r), & r \in \mathfrak{R}_{\rm A} \\ 0, & \text{otherwise,}\end{cases} \tag{3.24}$$

where $\mathfrak{R}_{\rm A} = [h_{\rm UA}, d]$.

Proof: The proof follows the same steps as that of Lemma 3.4; therefore, it is omitted here.

Lemma 3.6. Where the aerial user is associated with an NLoS terrestrial-BS (i.e., the event $\mathcal{E}_{\rm N}$ occurs), the distribution of the distance $\tilde{R}_N$ between the aerial user and the serving NLoS terrestrial-BS is given by

$$f_{\tilde{R}_N|\mathcal{E}_{\rm N}}(r) = \begin{cases}\frac{1}{\mathcal{A}_{\rm N}} F_{R_L}^{(c)}\left(\tau_{L|\mathcal{E}_{\rm N}}(r)\right) \times F_{R_A}^{(c)}\left(h_{\rm UA}\right) \times f_{R_N}(r), & r \in \mathfrak{R}_{\rm N} \\ 0, & \text{otherwise,}\end{cases} \tag{3.25}$$

where $\mathfrak{R}_{\rm N} = [h_{\rm UT}, d]$.

3.3.5 Laplace Transform of the Aggregated Interference

Depending on the spectrum sharing policy, the aerial user may receive interference signals from aerial-BSs and terrestrial-BSs whose Laplace transforms are characterized in the following lemmas.

Lemma 3.7. Conditioned on the event $\mathcal{E}_\nu$, $\nu \in \{\rm L, N, A\}$, the Laplace transform of the terrestrial interference power, $I_L + I_N$, is given by

$$\mathcal{L}_{(I_N+I_L)|\mathcal{E}_\nu}(s)=\prod_{\omega\in\{\rm L,N\}}\exp\left(-2\pi\lambda_{\rm T}\int_{\tau_{\omega|\mathcal{E}_\nu}(r)}^{\infty}\left(1-\left(\frac{m_\omega}{m_\omega+s\mu_\omega t^{-\alpha_\omega}}\right)^{m_\omega}\right)tP_\omega\left(\sqrt{t^2-h_{\rm UT}^2}\right)dt\right). \tag{3.26}$$

Proof: See Appendix B.4.

Lemma 3.8. Conditioned on the event $\mathcal{E}_\nu$, $\nu \in \{\mathrm{L}, \mathrm{N}, \mathrm{A}\}$, the Laplace transform of the aerial interference power, I_A, is given by

$$\mathcal{L}_{I_A|\mathcal{E}_\nu}(s) = \sum_{i=0}^{N'} \binom{N'}{i} \left(\frac{2 m_A^{m_A} (s P_A \eta_A)^{-m_A}}{\alpha_A \Gamma(m_A)(d^2 - r^2)} \right)^{N'} \times \left[q_{\mathrm{A}} \left(\Omega(d, G_{\mathrm{m}}^{\mathrm{A}}) - \Omega(\tau_{A|\mathcal{E}_\nu}(r)), G_{\mathrm{m}}^{\mathrm{A}}) \right) \right]^{N'-i} \times \left[(1 - q_{\mathrm{A}}) \left(\Omega(d, g_{\mathrm{s}}^{\mathrm{A}}) - \Omega(\tau_{A|\mathcal{E}_\nu}(r), g_{\mathrm{s}}^{\mathrm{A}}) \right) \right]^{i}, \quad (3.27)$$

where $\Omega[\cdot,\cdot]$ is given below by

$$\Omega(x, g) = \frac{x^{\alpha_A m_A + 2}}{g^{m_A}} \mathrm{G}_{2,2}^{1,2} \left[\frac{m_A x^{\alpha_A}}{s P_A g \eta_A} \middle| \begin{matrix} 1 - m_A - \frac{2}{\alpha_A}, 1 - m_A \\ 0, -m_A - \frac{2}{\alpha_A} \end{matrix} \right], \quad (3.28)$$

where $\mathrm{G}[\cdot]$ is the Meijer-G function given in [34, eq (9.301)].

Proof: See Appendix B.5.

3.3.6 Simplified C2A Channel Model

The previous results (association probabilities and Laplace transform of interference) require numerical evaluations of multiple integrals. These expressions can be simplified by noting that the aerial user may hover at elevated heights resulting in LoS transmissions with the terrestrial-BSs. Therefore, we assume that the C2A links are in LoS condition with the aerial user. The validity of this assumption will be investigated with simulations in Section 3.5. Under this assumption, the PDF and CDF of the distance between the aerial user and the nearest LoS terrestrial-BS are given by [31, eqs. (8) and (9)]

$$f_{R_L}(r) = 2\pi\lambda_{\mathrm{T}} r \exp\left(-\pi\lambda_{\mathrm{T}} \left(r^2 - h_{\mathrm{UT}}^2\right)\right), r \geqslant h_{\mathrm{UT}} \quad (3.29)$$

$$F_{R_L}(r) = 1 - \exp\left(-\pi\lambda_{\mathrm{T}} \left(r^2 - h_{\mathrm{UT}}^2\right)\right), \quad r \geqslant h_{\mathrm{UT}}. \quad (3.30)$$

Corollary 3.9. With the assumption that the aerial user is in LoS with the terrestrial-BSs, the association probability with a terrestrial-BS given in (3.17) can be written as in (3.31) at the top of the next page, where $\Upsilon(x) = \Gamma\left[\frac{\alpha_L}{\alpha_A} i + 1, \pi\lambda_{\mathrm{T}} x^2\right]$, with $\Gamma[\cdot,\cdot]$ denoting the upper incomplete Gamma function [34, eq (8.358.2)]. Thus, the probability of association with an aerial-BS is given by $\mathcal{A}_{\mathrm{A}} = 1 - \mathcal{A}_{\mathrm{L}}$.

$$\mathcal{A}_{\mathrm{L}} = \begin{cases} 1 - \exp\left(-\pi\lambda_{\mathrm{T}}\left(\zeta^2 - h_{\mathrm{UT}}^2\right)\right) + \frac{\pi\lambda_{\mathrm{T}} h_{\mathrm{UT}}^2}{r_{\mathrm{D}}^{2N}} \sum_{i=0}^{N} \binom{N}{i} (-1)^i d^{2(N-i)} \left(\frac{\mu_A}{\mu_L}\right)^{\frac{2i}{\alpha_A}} (\pi\lambda_{\mathrm{T}})^{-\frac{\alpha_L i}{\alpha_A}} & \\ \times \left[\Upsilon(\zeta) - \Upsilon(\zeta_{\mathrm{A}}^{\mathrm{L}}(d))\right], & h_{\mathrm{UT}} \leqslant \zeta_{\mathrm{A}}^{\mathrm{L}}(d) \\ 0, & h_{\mathrm{UT}} \geqslant \zeta_{\mathrm{A}}^{\mathrm{L}}(d). \end{cases} \tag{3.31}$$

Proof: Substitute (3.29) into (3.19) and apply the Binomial theorem. Then, using the definition of the upper incomplete Gamma function and some manipulations, we obtain (3.31).

Corollary 3.10. The Laplace transform of the terrestrial interference, $\mathcal{L}_{I_L|\mathcal{E}_\nu}(s)$, where $\nu \in \{\mathrm{L}, \mathrm{A}\}$, is given by

$$\mathcal{L}_{I_L|\mathcal{E}_\nu}(s) = \exp\left(-2\pi\lambda_{\mathrm{T}} \sum_{i=0}^{m_L-1} \left(\frac{s\mu_L}{m_L}\right)^{1+i-m_L} \frac{1}{\alpha_L \Gamma[m_L - i]} \tau_{L|\mathcal{E}_\nu}(r)^{\alpha_L(m_L-i-1)} \Theta(s, \tau_{L|\mathcal{E}_\nu}(r))\right), \tag{3.32}$$

where $\Theta(\cdot,\cdot)$ is defined as

$$\Theta(s, r) = \mathrm{G}_{2,2}^{2,1}\left[\frac{m_L r^{\alpha_L}}{s\mu_L} \middle| \begin{matrix} 1+i-m_L, 2+i-m_L-\frac{2}{\alpha_L} \\ 1+i-m_L-\frac{2}{\alpha_L}, 0 \end{matrix}\right]. \tag{3.33}$$

Proof: Starting from (3.26), substituting $P_L(t) = 1, \quad t \geqslant h_{\mathrm{UT}}$ and applying the identity $a^n - b^n = (a-b)\sum_{i=0}^{n-1} a^i b^{n-1-i}$, [59, eq (1.43)], and [34, eq (7.811.2)] yield (3.32).

3.4 Coverage and Rate Analysis

3.4.1 Downlink Coverage Probability

The coverage probability is defined as the probability of the SINR at the typical aerial user exceeding a predetermined threshold T. By applying the law of total probability, the coverage probability at the typical aerial user is given by

$$\mathcal{C} = \sum_{\nu \in \{\mathrm{L,N,A}\}} \mathcal{A}_\nu \times \mathcal{C}_\nu, \tag{3.34}$$

where $\mathcal{A}_\nu$ and $\mathcal{C}_\nu, \nu \in \{\mathrm{L}, \mathrm{N}, \mathrm{A}\}$ denote the association probability with the Φ_ν tier and the coverage probability given that the aerial user is associated with the BS from Φ_ν, respectively.

Theorem 3.11. *The coverage probability $\mathcal{C}_\nu$ conditioned on the events $\mathcal{E}_\nu, \nu \in \{\mathrm{L}, \mathrm{N}, \mathrm{A}\}$ is given by*

$$\mathcal{C}_\nu = \sum_{k=0}^{m_\nu - 1} \frac{(-1)^k}{k!} \left(\frac{m_\nu T}{\mu_\nu} \right)^k \int_{r \in \mathfrak{R}_\nu} r^{k\alpha_\nu} \left[\frac{\partial^k}{\partial s^k} \mathcal{L}_{V|\mathcal{E}_\nu}(s) \right]_{s = \frac{m_\nu T r^{\alpha_\nu}}{\mu_\nu}} f_{\tilde{R}_\nu|\mathcal{E}_\nu}(r) dr, \tag{3.35}$$

where $V = I + \sigma^2$ and $\mathcal{L}_{V|\mathcal{E}_\nu}(s)$ is given by $\mathcal{L}_{V|\mathcal{E}_\nu}(s) = \exp(-\sigma^2 s) \mathcal{L}_{I|\mathcal{E}_\nu}(s)$.

Note that under the N-OSS policy, $\mathcal{L}_{I|\mathcal{E}_\nu}(s) = \mathcal{L}_{(I_N + I_L)|\mathcal{E}_\nu}(s) \times \mathcal{L}_{I_{A|\mathcal{E}_\nu}}(s)$.

Proof: See Appendix B.6.

3.4.2 Downlink Average Achievable Rate

In this section, we derive the average achievable rate of the typical aerial user. Following the same analysis as the coverage probability, the average ergodic rate is given by

$$\mathcal{R} = \sum_{\nu \in \{\mathrm{L}, \mathrm{N}, \mathrm{A}\}} \mathcal{A}_\nu \times \mathcal{R}_\nu, \tag{3.36}$$

where $\mathcal{R}_\nu$ is the average achievable rate of the aerial user when it is associated with a BS from the tier Φ_ν.

Theorem 3.12. *The average achievable rate of the typical aerial user when it is associated with Φ_ν tier is given by*

$$\mathcal{R}_\nu = \sum_{k=0}^{m_\nu - 1} \frac{(-1)^k}{\ln(2) k!} \left(\frac{m_\nu}{\mu_\nu} \right)^k \int_0^\infty \int_{r \in \mathfrak{R}_\nu} r^{k\alpha_\nu} (e^t - 1)^k \left[\frac{\partial^k}{\partial s^k} \mathcal{L}_{V|\mathcal{E}_\nu}(s) \right]_{s = \frac{m_\nu (e^t - 1) r^{\alpha_\nu}}{\mu_\nu}} f_{\tilde{R}_\nu|\mathcal{E}_\nu}(r) dr dt, \tag{3.37}$$

Proof: Using Shannon's theorem, the average achievable rate can be expressed as

$$\mathcal{R}_\nu = \frac{1}{\ln(2)} \mathbb{E}_{\tilde{R}_\nu} \left[\mathbb{E}_\gamma \left[\ln(1 + \gamma) \right] \right] \overset{(a)}{=} \frac{1}{\ln(2)} \mathbb{E}_{\tilde{R}_\nu} \left[\int_0^\infty \mathbb{P} \left(\gamma \geqslant e^t - 1 \right) dt \right], \tag{3.38}$$

where (a) follows from $\mathbb{E}[Z] = \int_0^\infty \mathbb{P}(Z > t) dt$. Substituting (3.10) into (3.38) and following the same steps as those of Theorem 3.11 yields (3.37).

3.4.3 Downlink Coverage and Average Achievable Rate Approximations

The evaluation of the results presented in (3.35) and (3.37) for the conditional coverage probabilities and average achievable rates involves higher order derivative of the Laplace transform, which leads to a more complex computation especially for large fading parameters, i.e., m_ν, $\nu \in \{\mathrm{L}, \mathrm{N}, \mathrm{A}\}$. Thus, a lower bound of the Gamma distribution's CCDF is used instead of the exact evaluation.

Theorem 3.13. *The approximation of the conditional coverage probability* $\mathcal{C}_\nu^{\text{approx}}$, $\nu \in \{\mathrm{L}, \mathrm{N}, \mathrm{A}\}$ *is given by*

$$\mathcal{C}_\nu^{\text{approx}} \approx \sum_{k=1}^{m_\nu} (-1)^{k+1} \binom{m_\nu}{k} \int_{r \in \Re_\nu} \mathcal{L}_{V|\mathcal{E}_\nu} \left(\frac{k \rho_\nu T r^{\alpha_\nu}}{\mu_\nu} \right) f_{\tilde{R}_\nu|\mathcal{E}_\nu}(r) dr, \tag{3.39}$$

where $\rho_\nu = m_\nu (m_\nu!)^{\frac{-1}{m_\nu}}$, *with* $m_\nu > 1$.

Proof: Using [60], the CCDF of a Gamma-distributed random variable, $\mathrm{H}_\nu^{\mathrm{x}_0}$, can be tightly lower bounded by

$$\mathbb{P}\left(\mathrm{H}_\nu^{x_0} \geqslant \beta\right) \geqslant 1 - [1 - e^{-\rho_\nu \beta}]^{m_\nu} = \sum_{k=1}^{m_\nu} (-1)^{k+1} \binom{m_\nu}{k} e^{-k \rho_\nu \beta}, \tag{3.40}$$

where the equality holds when $m_\nu = 1$. Thus, substituting this upper bound to (c) in (B.8) along the same mathematical manipulations concludes the proof.

Theorem 3.14. *The conditional average achievable rate approximation* $\mathcal{R}_\nu^{\text{approx}}$, $\nu \in \{\mathrm{L}, \mathrm{N}, \mathrm{A}\}$ *is given by*

$$\mathcal{R}_\nu^{\text{approx}} \approx \frac{1}{\ln(2)} \sum_{k=1}^{m_\nu} (-1)^{k+1} \binom{m_\nu}{k} \int_0^\infty \int_{r \in \Re_\nu} \mathcal{L}_{V|\mathcal{E}_\nu} \left(\frac{k \rho_\nu r^{\alpha_\nu} (e^{-t} - 1)}{\mu_\nu} \right) f_{\tilde{R}_\nu|\mathcal{E}_\nu}(r) dr dt. \tag{3.41}$$

Proof: The proof follows the same steps as that of Theorem 3.13; therefore, it is omitted here.

3.5 Results and Discussion

In this section, we use Monte Carlo simulations to validate the analytical expressions. We also investigate the impact of several design parameters on the VHetNet's performance.

Table 3.5: Parameter values

Parameter	Value	Parameter	Value	Parameter	value
$(P_T,\ P_A)$	(43, 30) dBm	$(m_L,\ m_N,\ m_A)$	(2, 1, 2)	N	10
r_{D}	2000 meters	$(G_{\mathrm{m}}^{\mathrm{T}},\ g_{\mathrm{s}}^{\mathrm{T}})$	(0, -15) dB	$(\eta_L,\ \eta_N,\ \eta_A)$	(-3, -20, -1) dB
$(G_{\mathrm{m}}^{\mathrm{A}},\ g_{\mathrm{s}}^{\mathrm{A}})$	(0, -20) dB	C2A	LoS/NLoS	σ^2	-113 dBm
$(\alpha_L,\ \alpha_N,\ \alpha_A)$	(2.5, 3.5, 2)	λ_{T}	5	T	5 dB
Policy	N-OSS	Environment	Urban	$\theta_{\mathrm{B}}^{\mathrm{A}}$	18°
$(h_{\mathrm{U}},\ h_{\mathrm{A}})$	(50, 300) meters	q_{A}	0.1	h_{T}	20 meters

Table 3.5 summarizes the parameters used in the simulations, unless otherwise indicated. It should be mentioned that we used parameters set by the 3GPP report in [2] which limit the maximum hovering height for aerial users to 300 meters. The height of an aerial-BS, however, can extend up to a few kilometers [16, 26, 46].

In Fig. 3.3, we compare aerial-BS and terrestrial-BS association probabilities with different aerial user heights and environments. Notably, at any aerial user height, $\mathcal{A}_{\mathrm{A}} + (\mathcal{A}_{\mathrm{L}} + \mathcal{A}_{\mathrm{N}}) = 1$. At low aerial user heights, the aerial user tends to be associated with an aerial-BS because the C2A links are dominated by NLoS links, which have poor channel conditions in comparison to LoS A2A links. As the height increases, the terrestrial-BS association probability increases since more terrestrial-BSs come within LoS condition of the aerial user. However, with a further increase in height, the terrestrial-BS association probability starts to decrease because of the significant path-loss caused by the increasing distances between the aerial user and the terrestrial-BSs. Essentially, for a given environment and height, the aerial user probability of association to either a terrestrial or aerial network indicates the likelihood of the serving BS belonging to either of the two networks, respectively.

Fig. 3.4 shows the coverage probability versus the SINR threshold for different environments. For a particular SINR threshold, as the environment becomes less dense, more terrestrial-BSs come into LoS with the aerial user (i.e., more interfering LoS terrestrial-BSs) which increases the interference. As discussed in Section II, the analytical tractability of a VHetNet with aerial-BSs at varying heights is quite challenging. Interestingly, aerial-BSs hovering at the same height h_{A} guarantee a comparable performance to VHetNets involving aerial-BSs with heights uniformly distributed between $h_{\max}$ and $h_{\min}$ with an average height of h_{A}. The results presented in Fig. 3.4 show that a small variation in the height

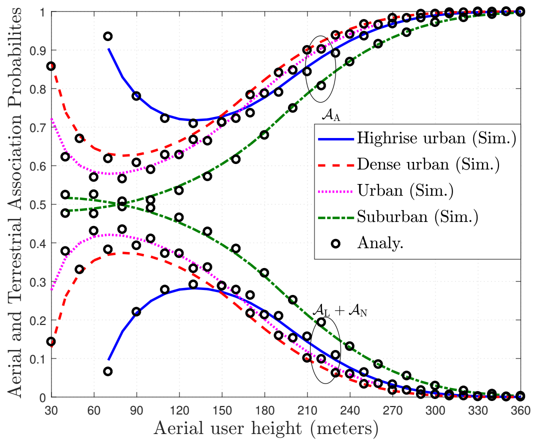

Fig. 3.3: Association probability versus aerial user height with $h_{\mathrm{A}} = 500$ meters.

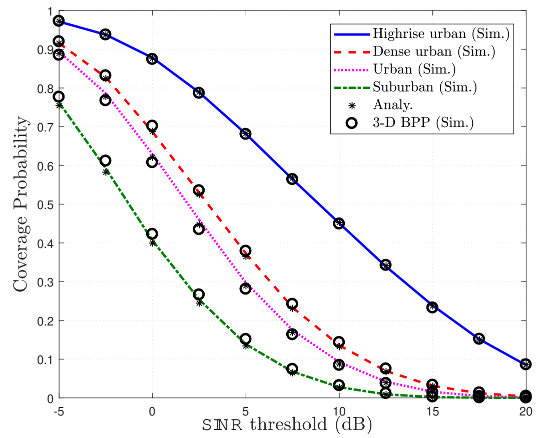

Fig. 3.4: Coverage probability versus SINR threshold: $h_{\mathrm{U}} = 70$ meters and $h_{\mathrm{A}} = 200$ meters. For 3-D BPP scenario: $h_{\max} = 225$ meters and $h_{\min} = 175$ meters.

of aerial-BSs does not affect the overall performance. This is because the aerial-BSs are distributed over the area of a disc with a radius that is much larger than the aerial-BS heights, which means that small variations in aerial-BS heights do not have a significant impact on the distribution of the distances separating the aerial user from the aerial-BSs.

Fig. 3.5 shows the performance of VHetNets where aerial-BSs hover at different heights but are confined between two values: $h_{\min} = h_{\mathrm{A}} - \frac{\mathrm{H_C}}{2}$ and $h_{\max} = h_{\mathrm{A}} + \frac{\mathrm{H_C}}{2}$ as depicted in Fig. 3.1(a), where aerial-BSs are uniformly distributed within a finite cylinder of height $\mathrm{H_C}$ and radius r_{D}. Fig. 3.5 shows that the coverage probability using a 3-D BPP aerial network is the same as its counterpart assuming a 2-D BPP at a fixed height h_{A} (in this case $\mathrm{H_C} = 0$) when $\mathrm{H_C}$ is much larger than the aerial-BSs height, h_{A}. However, the 2-D BPP assumption does not guarantee a likewise coverage probability under 3-D BPP when the radius over which the aerial-BSs are distributed uniformly, r_{D}, is comparable to their heights, h_{A}. Indeed, works in [26] and [61] indicate that aerial-BSs are distributed over a large area with a radius in the order of a few kilometers, whereas aerial-BS heights are in the order of a few hundred meters. Given this, we wish to emphasize that the framework presented in this work is applicable under the assumption that the radius of the disk r_{D} over which the aerial-BSs can be distributed is much larger than the cylinder height $\mathrm{H_C}$. That

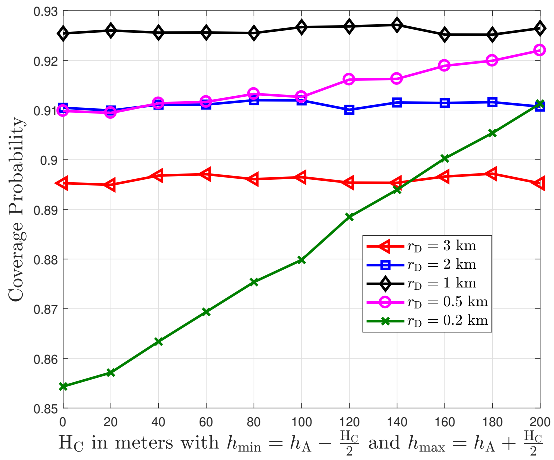

Fig. 3.5: Coverage probability for 3-D BPP scenario: N aerial-BSs are uniformly distributed in a finite cylinder with height $\mathrm{H_C}$ and radius r_D ($h_\mathrm{A} = 300$ meters and $T = -5$ dB).

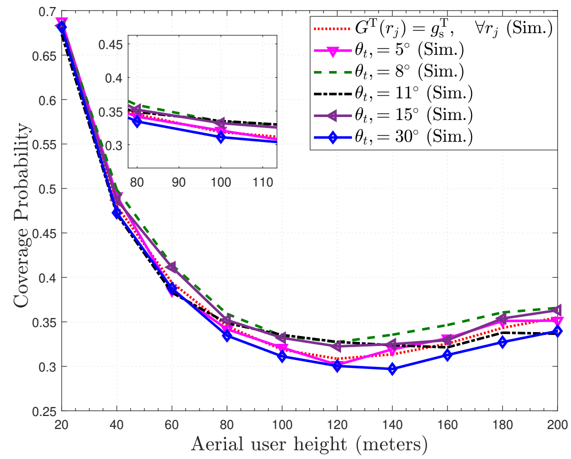

Fig. 3.6: Coverage probability versus aerial user height for different terrestrial-BS tilt-angles for $\theta_\mathrm{B}^\mathrm{T} = 30°$.

is, an aerial network with a dense deployment of aerial-BSs, where their heights and spacing are comparable, does not necessarily exhibit the same performance as the aerial network in this work. This is because the assumption concerning order of magnitude differences between r_D and $\mathrm{H_C}$ is violated, and, therefore, revisiting the performance analysis using more comprehensive models is required. Indeed, under the assumption $r_\mathrm{D} \gg \mathrm{H_C}$, Fig. 3.5 shows that the complexity from assuming a 3-D BPP network can be avoided by adopting a 2-D BPP network with a fixed height without compromising the performance accuracy or correctness. Finally, we can affirm that the assumption of fixed heights of aerial-BSs is legitimate enough to enable the tractability of the analysis.

Fig. 3.6 illustrates the coverage probability for different terrestrial-BS tilt-angles. The performance of VHetNets that assume different θ_t is close enough to the performance of the system, assuming that the aerial user is always serviced by the terrestrial-BS antenna sidelobes $G^\mathrm{T}(r_j) = g_\mathrm{s}^\mathrm{T}$, $\forall\ r_j$. This observation illustrates well the assumption that terrestrial-BSs cover aerial users mainly with their antenna sidelobes, since these are usually down-tilted toward terrestrial users. Further, as we pointed out, this assumption is the key enabler of the tractability of the association probabilities analysis.

In Fig. 3.7, we compare the coverage probability with different aerial user heights with OSS and N-OSS policies. Under the N-OSS policy, as the aerial user height increases, more terrestrial-BSs come within LoS of the aerial user, which increases the terrestrial interference at a greater rate than the increase in the desired signal power. Under the OSS policy, a different trend can be observed at low aerial user heights, i.e., the coverage probability increases. This is because at very low aerial user heights, the improvement in the desired signal power becomes greater than the increase in the terrestrial interference (since the aerial user may be in LoS with few terrestrial-BSs while terrestrial interference is dominated by NLoS terrestrial-BSs). However, with a further increase in the aerial user height, the interference received from the LoS terrestrial-BSs dominates, which degrades the coverage probability. Indeed, the significant difference in coverage probability under N-OSS and OSS policies is due to the heavy interference that the aerial user experiences under the N-OSS policy which includes aerial and terrestrial interferers alike. Under the OSS policy, by contrast, the aerial user is subject to interference only from BSs that belong to the same network (terrestrial or aerial) as its serving BS. It should also be mentioned that under the assumption that the C2A links are all LoS links, the coverage probability converges to the actual coverage probability.

Fig. 3.8 shows the coverage probability versus the density of the terrestrial-BSs for different aerial user heights and beamwidths under the OSS and N-OSS policies. Under the N-OSS policy, we notice that the coverage probability decreases as the density of terrestrial-BSs increases due to the increase in the terrestrial interference (more LoS terrestrial-BSs exist as the aerial user height increases). We can also observe that for a given density of terrestrial-BSs and regardless of the q_{A}, the coverage probability decreases as the aerial user height increases due to the increase in the terrestrial interference (terrestrial interference is dominated by LoS terrestrial-BSs). By contrast, under the OSS policy and at a high aerial user height (250 meters), the density of the terrestrial-BSs has no impact on the coverage probability, since the aerial user is always associated with an aerial-BS according

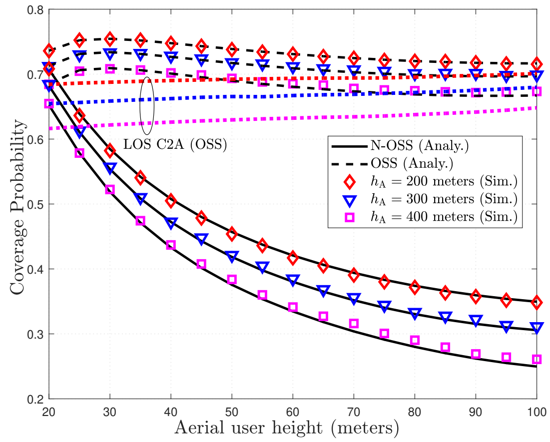

Fig. 3.7: Coverage probability versus aerial user height.

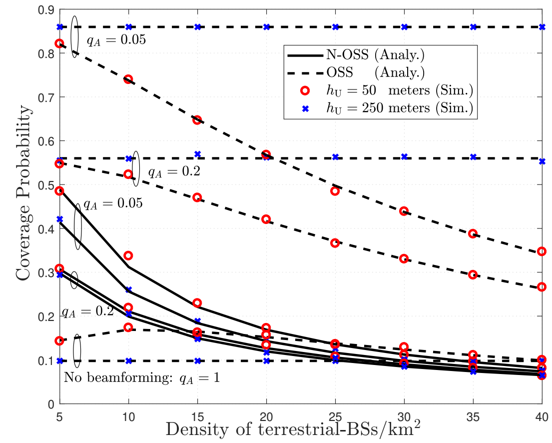

Fig. 3.8: Coverage probability versus terrestrial network density ($h_A = 300$ meters).

to Fig. 3.3, and thus, it does only receive interference from aerial-BSs. However, a similar trend is not observed if the aerial user is close to the terrestrial-BSs. For instance, at a low aerial user height (50 meters), the coverage probability decreases as the density of the terrestrial-BSs increases, since the aerial user may be associated with a terrestrial-BS, and so increasing the density of terrestrial-BSs increases the terrestrial interference. Overall, aerial BSs with more directed beams (smaller beamwidth implies smaller q_A) improves the coverage probability because it decreases the aerial interference power.

We plot the coverage probability versus the number of aerial-BSs for different aerial user heights in Fig. 3.9. The approximation of the coverage probability using the tight lower bound of the Gamma distribution's CCDF is in a good agreement with the exact performance. Generally, increasing the number of aerial-BSs decreases the coverage probability due to the fact that the increase in the aerial interference is greater than the increase in the desired signal. However, at high aerial user heights (e.g., 250 meters) and low aerial-BS numbers, the coverage probability increases as the number of aerial BSs increases. This is because the increase in aerial interference power is low (small number of aerial-BSs) compared to the improvement in the desired aerial signal. Overall, denser aerial-BSs decreases the coverage probability especially at low aerial user heights.

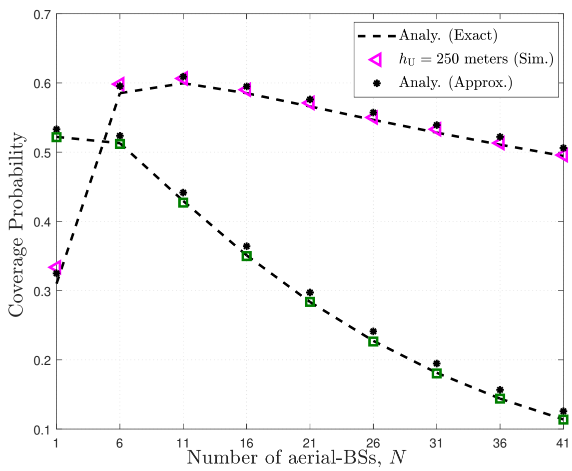

Fig. 3.9: Coverage probability versus number of aerial-BSs with $r_\mathrm{D} = 1$ km.

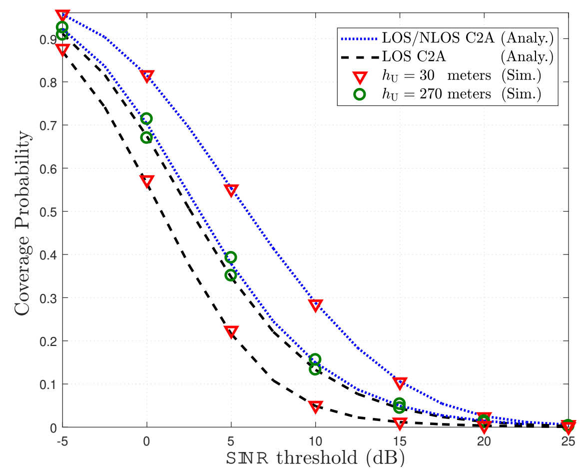

Fig. 3.10: Coverage probability versus SINR threshold with $h_\mathrm{A} = 300$ meters.

The validation of the LoS C2A assumption, which is presented in Section 3.3.6, is shown in Fig. 3.10. At low aerial user heights (e.g., $h_\mathrm{U} = 30$ meters), LoS C2A assumption is not a good approximation. This is because of the high likelihood of obstructions (NLoS links) between the aerial user and terrestrial-BSs. However, at elevated heights (e.g., $h_\mathrm{U} = 270$ meters), the aerial user is very likely to be in LoS with terrestrial-BSs (no or a few NLoS terrestrial-BSs exist) which justifies the correctness and accuracy of the LoS C2A assumption.

In Fig. 3.11, we show the accuracy of the average achievable rate approximation given in (3.41). NLoS links are assumed to follow Rayleigh fading, $m_N = 1$, whereas LoS links follow Nakagami-m with $m_L = 2$. We illustrate the average achievable rate for different fading parameter m_A for the A2A channels. According to the figure, the approximate rate derived in (3.41) matches very closely the exact analytical results for a smaller fading parameter m_A. As the latter increases, the approximation in (3.41) becomes an upper bound for the exact average achievable rate. Moreover, as the aerial-BSs height increase, the rate decreases. This can be explained by the fact that the power signal received from the aerial-BSs is weakened by the high path-loss, whereas the aggregate interference power received from the terrestrial-BSs remains the same.

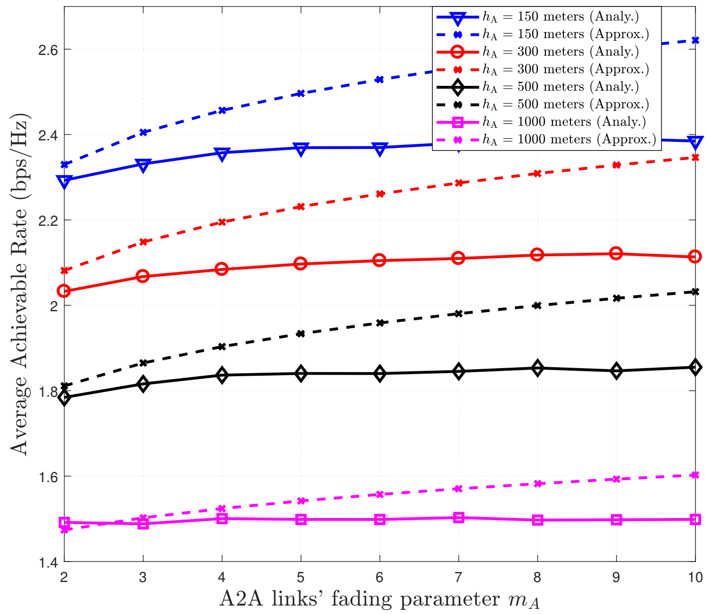

Fig. 3.11: Average achievable rate versus fading parameter m_A for A2A links, where $h_{\mathrm{U}} = 50$ meters.

3.6 Conclusion

Using stochastic geometry tools, we proposed a complete framework to analyze the coverage probability and rate of a typical aerial user served by a network of aerial-BSs and LoS/NLoS terrestrial-BSs. Useful distance distributions between the aerial user and its nearest terrestrial-BSs (LoS and NLoS) and aerial-BS were derived, which enabled the computation of the association probabilities of the typical aerial to terrestrial and aerial networks. Exact and approximations of the coverage probability and average achievable rate were presented assuming Nakagami-m fading for all C2A and A2A channels. Simulations revealed that the approximations of the coverage probability and average achievable rate agree very well with the exact expressions, especially with a small fading parameter. Simple expressions were presented under the assumption of only LoS transmissions in the C2A links. Several conclusions can be drawn from the simulations and evaluated analytical expressions:

- The association probabilities of an aerial user with an aerial-BS or terrestrial-BS depend on the height of the aerial user, the height of the aerial-BS, and the environment. For instance, the aerial user tends to connect to an aerial-BS when the former is hovering at a very low height and in a dense environment. It was also shown that an optimum aerial user height exists that maximizes the association probability to a terrestrial-BS. As the aerial user's height increases, the terrestrial-BS is no longer able to provide enough signal power due to high path-loss, which means the aerial user will then certainly be served by an aerial-BS.

- Simulation results show that the aerial user receives strong interference signals from LoS terrestrial-BSs and aerial-BSs, which degrade the coverage probability and rate. Orthogonal spectrum sharing between terrestrial and aerial networks considerably increases the coverage and rate performance of the aerial user. The simulations shows that an optimum height exists for which the coverage probability of the aerial user is maximized.

- It was also shown that employing directive beamforming at LoS aerial-BSs is essential in the operation of VHetNets as it decreases the aggregate power of aerial-BSs interference, and as a result it increases the aerial user coverage substantially. Other interference mitigation techniques might also be deployed to improve the aerial user operation.

- The results further show that aerial users at elevated heights are mainly in LoS with the terrestrial-BSs (no or a few NLoS links exist). Thus, the analysis can be simplified by assuming two tiers of BSs (i.e., LoS terrestrial-BSs and aerial-BSs). The simulation proves that this approximation is accurate at elevated heights and matches well the performance with LoS/NLoS C2A links. However, this approximation is not valid for low aerial user heights where NLoS links are more likely to exist and cannot be dismissed in the performance evaluation.

- Finally, it can be concluded from the results that increasing the density of the aerial-BSs may or may not degrade the performance, depending on the height of both the aerial-BSs and the aerial user. As we saw, a denser aerial network decreases the coverage probability of the aerial user, especially when it hovers at low heights.

Chapter 4

On the Optimal 3D Placement of a UAV Base Station for Maximal Coverage of UAV Users

4.1 Introduction

The number of UAVs is expected to skyrocket in the near future according to reports from the US federal aviation administration (FAA). Based on statistics of March 2020, slightly over 1.5 million UAVs are registered in the US, and the number is projected to increase exponentially in the upcoming years, as UAVs are becoming an important part of the every-day's life [62]. UAVs are expected to be part of the 5G wireless networks in two ways: 1) as an aerial base station (UAV-BS) that provides cellular connectivity [36] or 2) as an aerial user (UAV-UE) [63]. Due to their flexible deployment, UAV-BSs (a.k.a., UxNBs in 3GPP terminology [37]), can provide in-demand wireless broadband in temporary events or ubiquitous cellular coverage in hard-to-access remote areas [36]. Meanwhile, UAV-UEs

This work has been published in IEEE Globecom 2020 proceedings: **N. Cherif**, W. Jaafar, H. Yanikomeroglu, and A. Yongacoglu, "On the optimal 3D placement of a UAV base station for maximal coverage of UAV users", *IEEE Global Communications Conference* (Globecom), Taipei, Taiwan, Dec. 2020, pp. 1-6.

are used to accomplish new services and tasks, such as flying taxis, package delivery, video surveillance, aerial security inspection, wireless sensors data collection, etc. To do so, UAV-UEs require a reliable connectivity to the wireless network. Since most terrestrial BSs are down-tilted, their vertical coverage is rather patchy and does not satisfy the stringent requirements of UAV-UEs operations [2, 44]. In addition, hard-to-access remote areas may not have terrestrial BSs, hence, UAV-UEs would be left without any cellular connectivity to fulfill their tasks. Consequently, providing ubiquitous aerial coverage using UAV-BSs becomes a key enabler of reliable UAV-UEs communications. Hence, a comprehensive aerial coverage planning using UAV-BSs is urgently needed to enable UAV-UEs based services.

Several works on UAV-based wireless communications have investigated challenges linked to the efficient deployment of UAV-BSs to serve terrestrial users [64, 65]. For instance, the authors of [13] developed an efficient algorithm for 3D UAV-BS placement to serve terrestrial users. Then, they extended their study in [14] to the impact of the Quality-of-Service (QoS) irregularity on the optimal deployment of the UAV-BS. In [8], the authors proposed an efficient algorithm to maximize the sum-rate of terrestrial users by jointly optimizing the UAV-BSs wireless backhaul bandwidth and the wireless link association between terrestrial users and UAV-BSs. Also, authors in [66] investigated the joint placement and power allocation of a UAV-BS to maximize the coverage of terrestrial users. Finally, the authors of [30] studied the efficient deployment of multiple UAV-BSs for terrestrial coverage using the circle packing theorem.

Literature on cellular-connected UAVs, i.e., UAV-UEs, has been mainly focusing on reutilizing the terrestrial network as the exclusive communications provider to UAV-UEs. For instance, authors of [10] derived the connectivity performance of a typical UAV-UE served by a network of terrestrial BSs, by leveraging tools from stochastic geometry. The same authors gave interesting insights and design recommendations in [11] for UAV-UEs deployment under the assumption of exclusive cellular coverage provided by terrestrial networks.

Recently, we investigated in [17, 44] the coverage probability of UAV-UEs in hybrid terrestrial/aerial networks, called vertical heterogeneous networks (VHetNets). We showed that in VHetNets, UAV-UEs are more likely to be served by UAV-BSs since terrestrial BSs do not provide enough power to UAV-UEs at high elevation angles. Moreover, it was concluded that directional antennas are essential in deploying UAV-BS, especially because they substantially mitigate the aggregated aerial interference. Recently, the authors of [63, 67] proposed a novel wireless network architecture of UAVs, where the optimal 3D cell association, i.e., between UAV-UEs and UAV-BSs, is developed in order to minimize the average latency at UAV-UEs. In their study, UAV-BSs were equipped with omni-directional antennas, and thus their 3D coverage was modeled as a truncated polyhedron. Yet, the 3D coverage of UAV-UEs using UAV-BSs equipped with directional antennas is still unexplored.

Consequently, we investigate in this Chapter the optimal 3D deployment of a directional-antenna equipped UAV-BS in an aerial system, where UAV-UEs are assumed to be exclusively associated with UAV-BSs. In particular, we formulate the UAV-BS 3D placement problem aiming to maximize the number of covered UAV-UEs, given a spectrum sharing policy with terrestrial networks. Unlike terrestrial networks where all users are typically located at the ground altitude, UAV-UEs fly/hover in the 3D space at different locations and altitudes, with respect to flight regulations. As a consequence, the 3D coverage problem of UAV-UEs is more complex than in its terrestrial counterpart. Nevertheless, we propose a low complexity algorithm that determines the 3D optimal UAV-BS placement to cover the maximal number of UAV-UEs. Since spectrum sharing between aerial and terrestrial networks does affect the co-channel interference at terrestrial UEs, we propose a spectrum-aware UAV-BS 3D placement in the aerial network. The results obtained illustrate the coverage performance superiority of the UAV-BS under an OSS policy over its N-OSS counterpart, where the UAV-BS placement is constrained by an interference-avoidance condition at the terrestrial network. Also, they show distinct behaviors in OSS and N-OSS, given different parameters and configurations, e.g., antenna beamwidth, transmit power, aerial users density, aerial users clustering, and interference condition. Results obtained constitute essential guidelines to the co-existence of exclusive aerial networks with terrestrial networks.

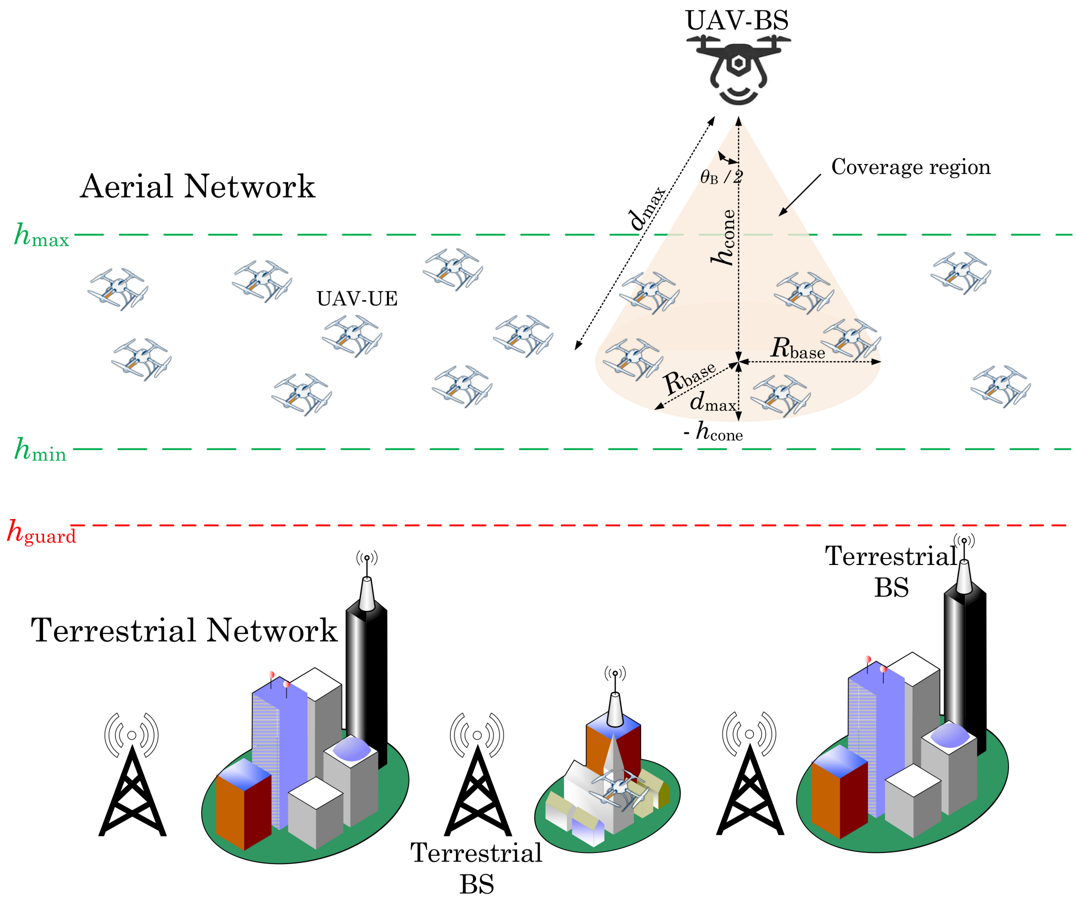

Fig. 4.1: System model.

4.2 System Model

We assume a 3D geographical area in the open sky, delimited by two altitude levels, namely $h_{\min}$ and $h_{\max}$, as shown in Fig. 4.1. In this area, a set $\mathcal{U}$ of UAV-UEs fly/hover at different altitudes. It is worth mentioning that according to the 3GPP report in [2], UAV-UEs cannot operate at altitudes above 300 meters. Moreover, the UAV-UEs are assumed to have the same power sensitivity $P_{\min}$, i.e., any UAV-UE succeeds in decoding a received signal when the latter's power is above $P_{\min}$. Let $\mathbf{q}_i = [x_i, y_i, z_i]$ be the 3D location of the i^{th} UAV-UE belonging to the set $\mathcal{U}$, such that $h_{\min} \leq z_i \leq h_{\max}$.

We assume that a directional-antenna equipped UAV-BS will be deployed to serve the UAV-UEs. Its antenna gain (in dB) is given by [30, eq (1)]

$$G = \begin{cases} G_{3\text{dB}}, & -\frac{\theta_{\text{B}}}{2} \leqslant \psi \leqslant \frac{\theta_{\text{B}}}{2}, \\ g_{\text{s}}, & \text{otherwise}, \end{cases} \tag{4.1}$$

where $\frac{\theta_{\text{B}}}{2}$ is the UAV-BS antenna's half beamwidth (in degrees), ψ is the sector angle, $G_{3\text{dB}} \approx \frac{29000}{\theta_{\text{B}}^2}$ is the main-lobe gain, and g_{s} is the side-lobe antenna gain.

In this work, we optimize the 3D location of the UAV-BS, designated by $\mathbf{q}_{\text{BS}} = [x_{\text{BS}}, y_{\text{BS}}, z_{\text{BS}}]$, in order to serve the maximal number of UAV-UEs. Intuitively, the UAV-BS would be placed above the UAV-UEs such that its antenna is tilted-down towards them in order to provide cellular connectivity for their operations. Specifically, the altitude of the UAV-BS should be at least $z_{\text{BS}} \geq h_{\max}$. Notably, 3GPP limits the altitude for UAV-UEs to a maximum of 300 meters, whereas UAV-BSs altitudes can reach few kilometers [2, 37]. Finally, we assume that the UAV-BS equivalent effective isotropic radiated power (EIRP), denoted P_{T}, is written as

$$P_{\text{T}} = P_t(\theta_{\text{B}}) + G_{3\text{dB}}, \tag{4.2}$$

where $P_t(\theta_{\text{B}})$ is the transmit power associated to the beamwidth of the directional antenna. From (4.1), we note that a larger antenna beamwidth θ_B results in a smaller 3 dB gain $G_{3\text{dB}}$, thus $P_t(\theta_B)$ has to be increased in order to maintain a fixed P_{T}.

When the UAV-BS communicates with the i^{th} UAV-UE, the received power can be expressed by

$$P_i = P_{\text{T}} - \underbrace{10n \log_{10}\left(\frac{4\pi f_c d_i}{c}\right)}_{=L_i} \geq P_{\min}, \tag{4.3}$$

where n is the pathloss exponent, f_c denotes the carrier frequency, d_i is the distance between the i^{th} UAV-UE and the UAV-BS, and L_i is the pathloss experienced by the i^{th} UAV-UE. The inequality in (4.3) ensures that the received power is above the sensitivity threshold. By taking the equality in (4.3), a pathloss maximal threshold can be defined as

$$L_{\text{th}} = P_{\text{T}} - P_{\min} \geq L_i. \tag{4.4}$$

By substituting L_i in (4.4) by its expression in (4.3), and after some mathematical manipulations, we can define the 3D coverage region, denoted $\mathcal{C}_{\text{in}}$, by a maximal distance between the UAV-BS and UAV-UEs, given by

$$d_{\max} = \frac{c}{4\pi f_c}\, 10^{\frac{L_{\text{th}}}{10n}}. \tag{4.5}$$

Since aerial networks would co-exist with terrestrial networks, the interference component generated by the deployment of UAV-BSs and affecting the terrestrial users may be non-negligible, and hence requires particular adjustments of the aerial network. In this context, we distinguish two spectrum sharing policies between the aerial and terrestrial networks: 1) OSS, where the UAV-BS communicates with its users at a different frequency band than the terrestrial BSs, and 2) N-OSS, where the aerial and terrestrial networks operate at the same frequency band. Under the OSS policy, terrestrial users won't experience interference from the UAV-BS, even if the latter operates at a relatively low altitude or high transmit power. However, under N-OSS, a regulatory altitude, called h_{guard}, must be respected when deploying the UAV-BS, in order to prevent any undesired and additional interference at terrestrial users. h_{guard} can be seen as the highest altitude at which a terrestrial user can be located. Hence, the received interference power at any terrestrial user has to be lower than a certain threshold, called Δ.[1] Specifically, we have

$$P_{\text{T}} - 10n \log\left(\frac{4\pi f_c \left(z_{\text{BS}} - h_{\text{guard}}\right)}{c}\right) \leq \Delta, \tag{4.6}$$

where $z_{\text{BS}} - h_{\text{guard}}$ is the smallest distance that can separate the UAV-BS from a terrestrial user, i.e., the latter is located directly below the UAV-BS at altitude h_{guard}. According to (4.6), the UAV-BS altitude has to respect the condition

$$z_{\text{BS}} \geq \frac{c}{4\pi f_c}\, 10^{\frac{P_{\text{T}}-\Delta}{10n}} + h_{\text{guard}} = \underbrace{d_{\max}\, 10^{\frac{P_{\min}-\Delta}{10n}}}_{=d'_{\max}} + h_{\text{guard}}. \tag{4.7}$$

Based on (4.7), the minimum altitude of the UAV-BS, when following a N-OSS policy, depends on both the receiver sensitivity of UAV-UEs and the tolerated interference level at terrestrial users.

UAV-BS Coverage Region

Based on (4.4)–(4.5), we infer that the 3D coverage region of the UAV-BS $\mathcal{C}_{\text{in}}$ is composed of two volumes, as illustrated in Fig. 4.1:

[1]This power threshold can be seen as the peak tolerated interference by any terrestrial user, under the assumption that transmissions in the terrestrial network are continuous [68].

- A 3D cone with the UAV-BS placed at its tip. The cone's opening angle is θ_{B} and its height, denoted h_{cone}, is

$$h_{\mathrm{cone}} = d_{\max} \cos\left(\theta_{\mathrm{B}}/2\right), \tag{4.8}$$

whereas its base's radius, R_{base}, can be written as

$$R_{\mathrm{base}} = d_{\max} \sin\left(\theta_{\mathrm{B}}/2\right). \tag{4.9}$$

- A faced-down half ellipsoid with radii $(R_{\mathrm{base}}, R_{\mathrm{base}}, d_{\max} - h_{\mathrm{cone}})$, and its center placed at coordinates $\mathbf{q}_{\mathrm{elp}} = [x_{\mathrm{BS}}, y_{\mathrm{BS}}, z_{\mathrm{BS}} - h_{\mathrm{cone}}]$, where the ellipsoid equation is given by

$$\frac{(x - x_{\mathrm{BS}})^2}{R_{\mathrm{base}}^2} + \frac{(y - y_{\mathrm{BS}})^2}{R_{\mathrm{base}}^2} + \frac{(z - z_{\mathrm{BS}} + h_{\mathrm{cone}})^2}{(d_{\max} - h_{\mathrm{cone}})^2} = 1. \tag{4.10}$$

In the next section, we formulate the 3D placement problem, then we propose an algorithm that places the UAV-BS at the best location, which allows covering the maximal number of UAV-UEs. The 3D UAV-BS deployment depends on the adopted spectrum sharing policy, as it will be shown below.

4.3 Optimal UAV-BS 3D Placement for Maximum UAV-UEs Coverage

Received interference at the terrestrial users from the UAV-BS depends on the latter's 3D placement and/or transmit power. Its deployment should be carefully planned, given the adopted spectrum sharing policy. In the subsequent sections, we investigate the 3D optimal placement under OSS and N-OSS policies.

4.3.1 UAV-BS 3D Placement Under OSS Policy

Under the OSS policy, The UAV-BS altitude z_{BS} is not restricted, as it doesn't result in any interference at the terrestrial users.

Remark 4.1. The i^{th} UAV-UE falls into the UAV-BS coverage region $\mathcal{C}_{\text{in}}$ if it satisfies the two following conditions:

$$c_1 : \ \|\mathbf{q}_i - \mathbf{q}_{\text{BS}}\| \leq d_{\max} \tag{4.11a}$$

$$c_2 : \ \cos\left(\frac{\theta_B}{2}\right) \leq \frac{|z_i - z_{\text{BS}}|}{\|\mathbf{q}_i - \mathbf{q}_{\text{BS}}\|}, \tag{4.11b}$$

where $\|\cdot\|$ is the Euclidean norm and $|\cdot|$ is the absolute value operations.

According to (4.11a), the i^{th} UAV-UE is within the region $\mathcal{C}_{\text{in}}$ when it is distant from the UAV-BS by at most $d_{\max}$. Meanwhile, (4.11b) ensures that the elevation angle between the i^{th} UAV-UE and UAV-BS is below the UAV-BS antenna half-beamwidth $\frac{\theta_{\text{B}}}{2}$.

Let c_i be the binary variable that indicates whether the i^{th} UAV-UE is in $\mathcal{C}_{\text{in}}$ or not, i.e., $c_i = 1$ when it is in the coverage region of the UAV-BS, and $c_i = 0$ otherwise. Consequently, the UAV-BS coverage maximization problem can be formulated as a mixed integer non-linear problem (MINLP) as follows:

$$\max_{\mathbf{q}_{\text{BS}}, \mathbf{c}} \quad \sum_{i \in \mathcal{U}} c_i \tag{P1}$$

$$\text{s.t.} \quad c_i \times \|\mathbf{q}_i - \mathbf{q}_{\text{BS}}\| \leq d_{\max}, \forall i \in \mathcal{U}, \tag{P1.a}$$

$$c_i \times \|\mathbf{q}_i - \mathbf{q}_{\text{BS}}\| \leq \frac{|z_i - z_{\text{BS}}|}{\cos\left(\frac{\theta_{\text{B}}}{2}\right)}, \forall i \in \mathcal{U}, \tag{P1.b}$$

$$c_i \in \{0, 1\}, \forall i \in \mathcal{U}, \tag{P1.c}$$

where $\mathbf{c} = [c_1, \ldots, c_U]$, and U is the total number of UAV-UEs. In order to guarantee the feasibility of the constraints (P1.a)–(P1.b) when $c_i = 0$, we rewrite them as follows [13]:

$$c_1 : \ \|\mathbf{q}_i - \mathbf{q}_{\text{BS}}\| \leq d_{\max} + N(1 - c_i), \ \forall i \in \mathcal{U} \tag{4.13a}$$

$$c_2 : \ \|\mathbf{q}_i - \mathbf{q}_{\text{BS}}\| \leq \frac{|z_i - z_{\text{BS}}|}{\cos\left(\frac{\theta_{\text{B}}}{2}\right)} - N(1 - c_i), \ \forall i \in \mathcal{U}, \tag{4.13b}$$

where N is a very large number. The complexity of solving (P1) arises from the dependency between $\mathbf{q}_{\text{BS}}$ and z_{BS} in constraint (4.13b). To tackle this issue, we propose to decouple the 2D UAV-BS location and its altitude's optimization. Indeed, for a specific UAV-BS altitude z_{BS}^1, (P1) reduces to a 2D UAV-BS location optimization problem. Then, exhaustive search over the altitude allows to find the optimal solution to (P1). The 2D optimization problem can be written as

Algorithm 4.1 3D UAV-BS placement under OSS policy

Input: $P_{\mathrm{T}}, \theta_{\mathrm{B}}, P_{\min}, f_c, h_{\min}, h_{\max}$

Output: $(\mathbf{q}_{\mathrm{BS}}^{\mathrm{opt}}, \mathbf{c}^{\mathrm{opt}})$

1: Compute $d_{\max}$ using (4.5)
2: **for** $z_{\mathrm{BS}}^1 \in [h_{\max}, h_{\max}+d_{\max}]$ **do**
3: Solve (P2), get $(\bar{\mathbf{q}}_{\mathrm{BS}}^1, \bar{\mathbf{c}}^1)$, and store it in a vector $\mathbf{v}$
4: **end for**
5: Select the best element in $\mathbf{v}$ that maximizes $\sum_{i\in\mathcal{U}} c_i$
6: Return $(\mathbf{q}_{\mathrm{BS}}^{\mathrm{opt}}, \mathbf{c}^{\mathrm{opt}})$ as the best element in $\mathbf{v}$.

$$\max_{x_{\mathrm{BS}}, y_{\mathrm{BS}}, \mathbf{c}} \quad \sum_{i\in\mathcal{U}} c_i \tag{P2}$$

$$\text{s.t.} \quad \|\mathbf{q}_i - \mathbf{q}_{\mathrm{BS}}^1\| \leq d_{\max} + N(1-c_i), \forall i \in \mathcal{U} \tag{P2.a}$$

$$\|\mathbf{q}_i - \mathbf{q}_{\mathrm{BS}}^1\| \leq \frac{|z_i - z_{\mathrm{BS}}^1|}{\cos\left(\frac{\theta_{\mathrm{B}}}{2}\right)} - N(1-c_i), \forall i \in \mathcal{U} \tag{P2.b}$$

$$c_i \in \{0,1\}, \forall i \in \mathcal{U}, \tag{P2.c}$$

where $\mathbf{q}_{\mathrm{BS}}^1 = [x_{\mathrm{BS}}, y_{\mathrm{BS}}, z_{\mathrm{BS}}^1]$. Since (P2.a)-(P2.b) constraints are convex, (P2) can be solved using MOSEK parser in the CVX package of Matlab [69]. Assuming that $(\bar{\mathbf{q}}_{\mathrm{BS}}^1, \bar{\mathbf{c}}^1)$ is the optimal solution of (P2) for a given z_{BS}^1, then (P1) can be solved iteratively using Algorithm 4.1, detailed above. In line 2 of Algorithm 4.1, z_{BS}^1 is in the range $[h_{\max}, h_{\max}+d_{\max}]$. Without loss of generality, $d_{\max} \geq h_{\max} - h_{\min}$, thus $z_{\mathrm{BS}}^1 = h_{\max}$ ensures that the vertical coverage of the UAV-BS is deep enough to cover even UAV-UEs flying/hovering at the lowest authorized altitude $h_{\min}$. In contrast, when $z_{\mathrm{BS}}^1 = h_{\max} + d_{\max}$, the coverage area of the UAV-BS is tangent to the horizontal plan at altitude $h_{\max}$, i.e., only a few users flying/hovering at $h_{\max}$ can be covered.

4.3.2 UAV-BS 3D Placement Under N-OSS Policy

Under the N-OSS policy, the UAV-BS coverage region is restricted in order to respect the tolerated interference level at terrestrial users. In this case, the UAV-BS' total transmit power, P_{T}, should be carefully adjusted to ensure that the UAV-BS hovers at an altitude of at least $h_{\max}$[2] as described in Fig. 4.1. Thus, the UAV-BS total transmit power should be no smaller than $P_{\mathrm{T}}^{\mathrm{low}}$ expressed by

$$P_{\mathrm{T}}^{\mathrm{low}} = 10n \log\left(\frac{4\pi f_c \left(h_{\max} - h_{\mathrm{guard}}\right)}{c}\right) + \Delta. \tag{4.15}$$

Since the UAV-BS altitude cannot exceed $d_{\max} + h_{\max}$[3], the UAV-BS total transmit power cannot exceed $P_{\mathrm{T}}^{\mathrm{high}}$, which is given by

$$P_{\mathrm{T}}^{\mathrm{high}} = 10n \log\left(\frac{4\pi f_c \left(h_{\max} - h_{\mathrm{guard}}\right)}{c \times \Omega}\right), \tag{4.16}$$

where $\Omega = 10^{-\frac{\Delta}{10n}} - 10^{-\frac{P_{\min}}{10n}}$.

Proof. The above result follows from substituting (4.4)–(4.5) into (4.7), where equality is taken for $z_{\mathrm{BS}} = d_{\max} + h_{\max}$. □

Finally, using (4.15)–(4.16), we have $P_{\mathrm{T}}^{\mathrm{low}} \leq P_{\mathrm{T}} \leq P_{\mathrm{T}}^{\mathrm{high}}$.

The UAV-BS 3D placement problem in N-OSS can be formulated as in (P1) with the additional optimization parameter P_{T} and constraints (4.7), (4.15), and (4.16). Unlike OSS policy, the UAV-BS EIRP should be optimized to guarantee two conditions: 1) the UAV-BS coverage region is maximized, and 2) imposed spectrum-sharing interference condition is respected. Subsequently, a similar approach as in Algorithm 4.1 can be followed to solve it. The proposed approach is presented in Algorithm 4.2, where $P_{\mathrm{T}}^{1} \in [P_{\mathrm{T}}^{\mathrm{low}}, P_{\mathrm{T}}^{\mathrm{high}}]$ and $z_{\mathrm{BS}}^{1} \in [h_{\max}, d_{\max} + h_{\max}]$.

4.4 Simulation Results

In our simulations, we consider a 3 km × 3 km area. Unless stated otherwise, we assume that $P_{\mathrm{T}} = 30$ dBm, $f_c = 2$ GHz, $P_{\min} = -70$ dBm, $\theta_{\mathrm{B}} = 60°$, $h_{\min} = 100$ meters, $h_{\max} = 300$ meters, $h_{\mathrm{guard}} = 50$ meters, and $\Delta = -73$ dBm. Also, simulations are averaged for 500

[2]Being at least at $h_{\max}$ with a sufficient coverage depth, $d_{\max}$, ensures a maximized vertical coverage.

[3]Above this altitude, the coverage performance is null since no UAV-UE flies/hovers at altitudes higher than $h_{\max}$.

Algorithm 4.2 3D UAV-BS placement under N-OSS policy

Input: $\theta_{\mathrm{B}}, P_{\min}, f_c, h_{\min}, h_{\max}, h_{\mathrm{guard}}, \Delta$

Output: $(\mathbf{q}_{\mathrm{BS}}^{\mathrm{opt}},\ \mathbf{c}^{\mathrm{opt}},\ P_{\mathrm{T}}^{\mathrm{opt}})$

1: Compute $P_{\mathrm{T}}^{\mathrm{low}}$ and $P_{\mathrm{T}}^{\mathrm{high}}$ using (4.15) and (4.16) resp.
2: **for** $P_{\mathrm{T}}^{1} \in [P_{\mathrm{T}}^{\mathrm{low}}, P_{\mathrm{T}}^{\mathrm{high}}]$ **do**
3: Compute $d_{\max}$ and $d'_{\max}$ using (4.5) and (4.7) resp.
4: **for** $z_{\mathrm{BS}}^{1} \in [h_{\max}, h_{\max} + d_{\max}]$ **do**
5: Solve (P2), get $(\bar{\mathbf{q}}_{\mathrm{BS}}^{1}, \bar{\mathbf{c}}^{1})$, and store it in vector $\mathbf{v}$
6: **end for**
7: Select the best element in $\mathbf{v}$ that maximizes $\sum_{i\in\mathcal{U}} c_i$ and store it with P_{T}^{1} in a vector $\mathbf{u}$
8: **end for**
9: Select the best element in $\mathbf{u}$ that maximizes $\sum_{i\in\mathcal{U}} c_i$
10: Return $(\mathbf{q}_{\mathrm{BS}}^{\mathrm{opt}},\ \mathbf{c}^{\mathrm{opt}},\ P_{\mathrm{T}}^{\mathrm{opt}})$ as the best element in $\mathbf{u}$.

UAV-UEs scenarios. For the UAV-UEs distribution per volume unit (km^3), we assume two point processes:

- Homogeneous Poisson point process (HPPP) for UAV-UEs uniform distribution in the 3D area delimited vertically by $h_{\min}$ and $h_{\max}$, with density λ UAV-UEs/km^3.
- Matérn cluster point process (MCPP) requiring two overlaying point processes: 1) a HPPP with density λ_P/km^3 as the *parent* cluster heads, and 2) a *daughter* HPPP with density λ_D of UAV-UEs belonging to a sphere with radius r_D centered at each *parent* cluster head. MCPP mimics the heterogeneity of the UAV-UEs distribution, where a higher λ_D means more clustered UAV-UEs.

4.4.1 UAV-BS Coverage Performance Under OSS Policy

Fig. 4.2 presents the optimal coverage performance of the UAV-BS under OSS policy.

Fig. 4.2(a) shows the average maximum number of covered UAV-UEs (a.k.a. coverage performance) as a function of UAV-BS altitude z_{BS}^{1}, for different θ_B and HPPP λ values.

Under OSS, an optimal altitude can be reached, which does not depend on the distribution of the UAV-UEs λ. However, as the UAV-BS antenna's beamwidth θ_B increases, the UAV-BS hovers at a lower altitude to cover more UAV-UEs.

In Fig. 4.2(b), the impact of the UAV-BS antenna's beamwidth θ_B, for different L_{th} is investigated, given an MCPP UAV-UEs distribution. As θ_B or L_{th} increases, the coverage performance improves. The same occurs when λ_D is high, i.e., UAV-UEs clusters are denser. Moreover, the transmit power $P_t(\theta_B)$ of the UAV-BS is evaluated using (4.2). When θ_B is higher, $G_{3\text{dB}}$ decreases, thus increasing $P_t(\theta_B)$, i.e., covering more UAV-UEs using a wide-beamwidth antenna comes at the expense of a higher transmit power.

Fig. 4.2(c) compares the coverage performance of our proposed algorithm to that of two benchmarks, namely "minimum sum distance" proposed in [66] where the UAV-BS placement is determined for minimum pathloss to all UAV-UEs, and "random placement" where the UAV-BS location is randomly selected. The coverage performance is evaluated as a function of the MCPP density λ_D, and for different MCPP λ_P values. We found that UAV-UEs clustering, i.e., higher λ_D and λ_P, improves the coverage performance for all UAV-BS placement approaches. Nevertheless, our algorithm significantly outperforms both benchmarks.

4.4.2 UAV-BS Coverage Performance Under N-OSS Policy

Fig. 4.3 presents the optimal coverage performance of the UAV-BS under N-OSS policy.

In Fig. 4.3(a), we show the coverage performance as a function of the UAV-BS altitude, given a HPPP UAV-UEs distribution. For any (P_{T}, θ_B, λ) setup, the optimal altitude is always the smallest allowed one, which is given by (4.7). This is expected since increasing the altitude can only reduce the overlapping area between the coverage region and the operating UAV-UEs' air corridor, thus reducing the number of covered UAV-UEs. This interesting outcome allows to reduce the steps taken in Algorithm 4.2 by omitting step 4, and calculating the best altitude for a given P_{T} using (4.7) instead.

Fig. 4.3(b) studies the impact of P_{T} on the coverage performance, for different θ_B and λ. For any (θ_B, λ) setup, an optimal P_{T} value can be obtained, which maximizes the coverage performance. Also, as θ_B reduces, i.e., narrower antenna beamwidth, more transmit power is required to cover the maximal number of UAV-UEs. Indeed, the loss in horizontal coverage (wider θ_B) is compensated by a deeper vertical coverage (higher P_{T}), with respect to the interference condition Δ (i.e., moving to a higher altitude as shown in Fig. 4.3(a)). Therefore, a low-altitude UAV-BS uses less transmit power for connectivity to UAV-UEs, while keeping its interference at the terrestrial users lower than Δ.

Finally, the impact of the regulatory altitude, h_{guard}, on the coverage performance is illustrated in Fig. 4.3(c). A more relaxed regulatory altitude for terrestrial users, i.e., smaller h_{guard}, increases the average maximum number of covered UAV-UEs. Indeed, the UAV-BS would move with more flexibility in order to increase the overlapping area between its coverage region and the UAV-UEs' air corridor. Furthermore, wider UAV-BS antenna beamwidth always provides a better coverage performance independently from the regulatory altitude. Eventually, under the N-OSS policy, the regulatory altitude h_{guard} and the peak tolerated interference at terrestrial users Δ should be carefully considered as they significantly impact the 3D UAV-BS placement and coverage performance.

4.5 Conclusion

In this Chapter, we studied the 3D placement problem of a directional-antenna equipped UAV-BS, aiming to maximize the number of flying/hovering UAV-UEs under its coverage region. The problem is formulated under two spectrum sharing policies, OSS and N-OSS, where frequency resources are either shared orthogonally or non-orthogonally between the aerial and terrestrial networks. Then, we solved the 3D UAV-BS placement using an iterative approach, where the horizontal 2D location of the UAV-BS is optimized for each explored altitude, and finally the altitude demonstrating the best coverage performance is selected. Simulation results have shown that under OSS policy, the UAV-BS hovers at low altitudes when its antenna's beamwidth is large. Also, we found that differences in UAV-UEs location distributions affect the performance of the UAV-BS. Indeed, the coverage performance improves when more UAV-UEs are clustered together. On the other hand, under N-OSS policy, the optimal UAV-BS altitude is always the lowest authorized one. Moreover, UAV-BS transmit power has to be optimized for maximum 3D coverage, while satisfying the interference condition on the terrestrial network. Finally, N-OSS results showed that a narrower UAV-BS antenna beamwidth is compensated by a higher transmit power and altitude.

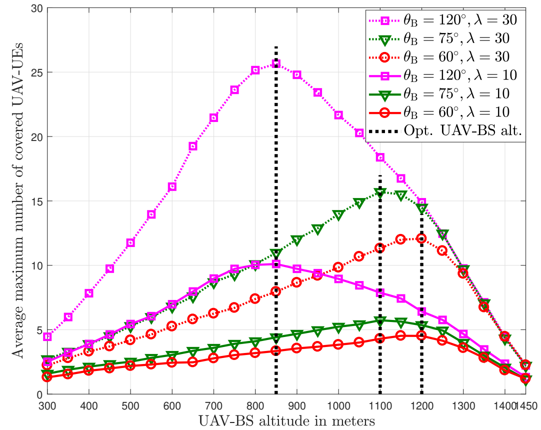

(a) Avg. max. number of covered UAV-UEs vs. UAV-BS altitude.

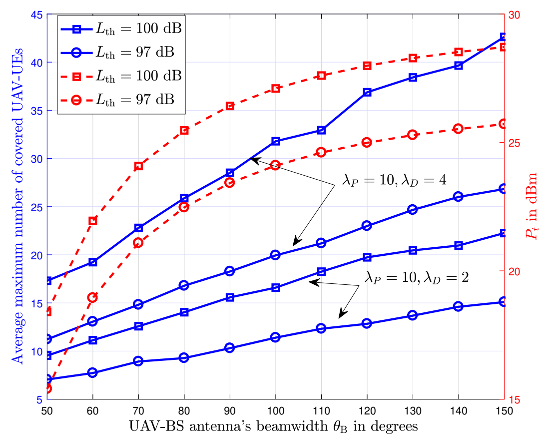

(b) Avg. max. number of covered UAV-UEs vs. UAV-BS antenna beamwidth.

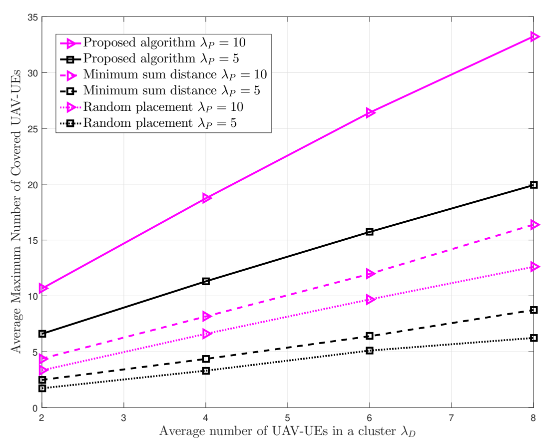

(c) Avg. max. number of covered UAV-UEs vs. distribution of UAV-UEs.

Fig. 4.2: UAV-BS coverage performance under OSS policy.

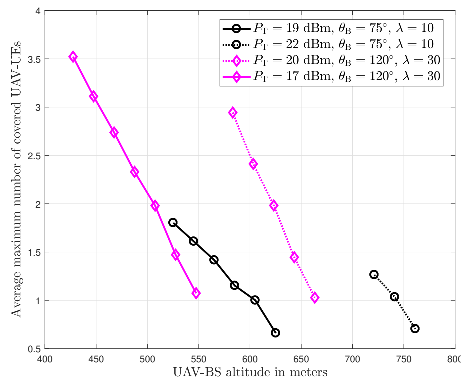

(a) Avg. max. number of covered UAV-UEs vs. UAV-BS altitude.

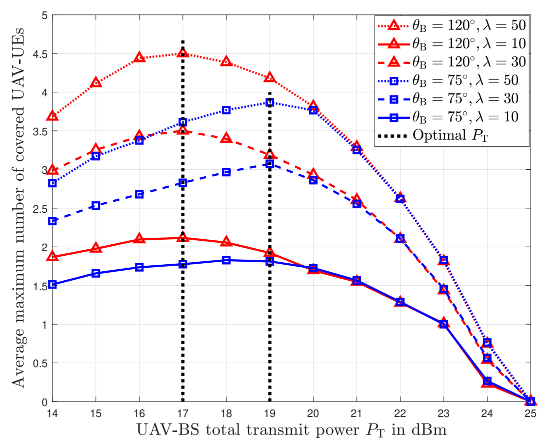

(b) Avg. max. number of covered UAV-UEs vs. UAV-BS total transmit power.

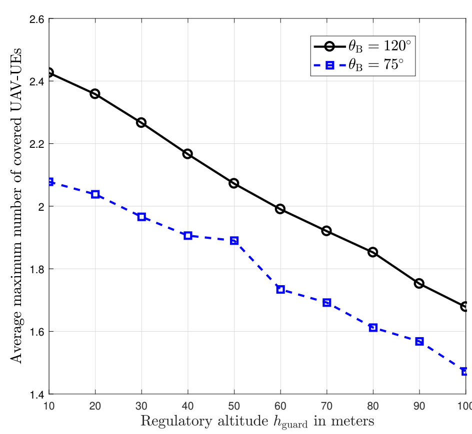

(c) Avg. max. number of covered UAV-UEs vs. the N-OSS regulatory altitude.

Fig. 4.3: UAV-BS coverage performance under N-OSS policy.

Chapter 5

3D Aerial Highway: The Key Enabler of the Retail Industry Transformation

5.1 Introduction

Unmanned aerial vehicles (UAVs) are earning momentum in a wide range of applications, such as search-and-rescue, surveillance, and on-demand cellular connectivity [5]. Specifically, UAVs contribute in solving the logistics of the delivery industry [70]. With the proliferation of online shopping, an increasing amount of cargo has to be delivered in a timely manner. For instance, Amazon, FedEx, and UPS are delivering approximately 2.5, 3, and 4.7 billion US packages every year, respectively. With already congested roads, delayed truck deliveries complicate tight deadlines.

Alternatively, UAV technology is seen as an eco-friendly and cheaper mean of delivery for light-weight cargo [71]. Indeed, UAVs fly for moderate/long distances collision-free, due

This work has been published in IEEE Communications Magazine: **N. Cherif**, W. Jaafar, H. Yanikomeroglu, and A. Yongacoglu, "3D aerial highway: The key enabler of the retail industry transformation", *IEEE Communications Magazine*, vol. 59, no. 9, pp. 65-71, September 2021.

to sophisticated sense-and-avoid techniques. Also, using cargo-UAVs cuts delivery costs by at least 66% [72].

Amazon is pioneering development of UAV-based platforms for goods delivery in hard-to-reach and remote areas with “Amazon Prime Air”. Through project “Skyways”, Airbus validated the feasibility of end-to-end UAV-based parcel delivery for shore-to-ship missions dedicated to enhanced maritime logistics. Moreover, they demonstrated successful cargo delivery in dense urban environments. Food delivery industry is also seizing the opportunity to modernize operations in cities. For instance, UberEats started testing a UAV-based delivery system over San Diego in 2019. Obviously, the fast integration of UAV technology into different sectors shows that, within few years, UAV-based delivery will be operating not only in remote areas, but also in dense urban centres. This will create a high volume of cargo to deliver via airspace and in a stringent time frame. Hence, coordinated cargo-UAV operations is needed to guarantee the safety and fluidity of aerial traffic.

In this context, handful research papers investigated the problem of designing efficient UAV routes. Specifically, [73] proposed a safe drone highways network that eliminates the risk of UAV accidents, while a more agile UAV routes implementation, using evolutionary computing, has been presented in [74]. Finally, an urban logistics airport for UAVs was discussed in [75], where the authors proposed UAV flow control based on graph theory. Yet, to the best of our knowledge, none of the works presented a complete design process of coordinated UAV routes for massive cargo delivery operations.

Since there are more degrees-of-freedom in planning routes in airspace than on the ground, we define a *3D aerial highway* as a set of aerial routes that cargo-UAVs must follow to fly from one location to another. For simplicity, the term “route” is similar to a highway, street, or avenue in a road network, whereas “aerial highways” is similar to the road network itself. The “creation” of 3D aerial highways depends mainly on the cellular connectivity of its routes. Indeed, cargo-UAVs require a reliable communication link for the following tasks. First, combined with a global positioning system, it allows for accurate UAV positioning and precise landing. Also, C&C exchanges are critical for the safety and security of UAVs, as the latter report in real-time any physical or cyber-physical anomaly to the control center. Finally, UAVs can periodically map the area to identify any on-going urban changes that may impact the highways design.

Several research works shed light on potential network architectures to connect UAVs [10,44,45]. For instance, relying on terrestrial networks for aerial coverage has been extensively investigated, and realistic channel models for cellular ground-to-air channels standardized by the Third Generation Partnership Project (3GPP) TR 36.777. Results suggest that terrestrial networks may not be adequate to provide ubiquitous connectivity to cargo-UAVs. Subsequently, different architectures were proposed, including vertical heterogeneous networks (VHetNets) [44] and standalone aerial networks enabled by UAV base stations (UAV-BSs) [45]. Given the particular characteristics of cargo-UAV operations, it is not yet established which network architecture is the most suitable for providing seamless and ubiquitous communications in 3D aerial highways.

To ensure the safe operations of large-scale cargo-UAV systems in aerial highways, a non-negligible amount of data has to be collected and analyzed, including logs on cargo-UAV missions. The latter can be analyzed by artificial intelligence agents and used to update the aerial highways.

To fully exploit the potential of UAVs for cargo delivery, we propose here a design process of 3D aerial highways. In addition, we discuss concerns related to the 3D aerial highways paradigm, describe our vision, and study the suitability of different cellular networks for cargo-UAV operations.

5.2 3D Aerial Highways: Description and Concerns

5.2.1 Description

Unlike conventional highways, 3D aerial highways define virtual routes in the airspace. They can be designed in urban, rural or hard-to-reach areas. For example, Fig. 5.1 illustrates 3D aerial highways above an urban area, where cargo-UAVs travel between the retailer warehouse and consumers. These routes are strategically planned at differ-

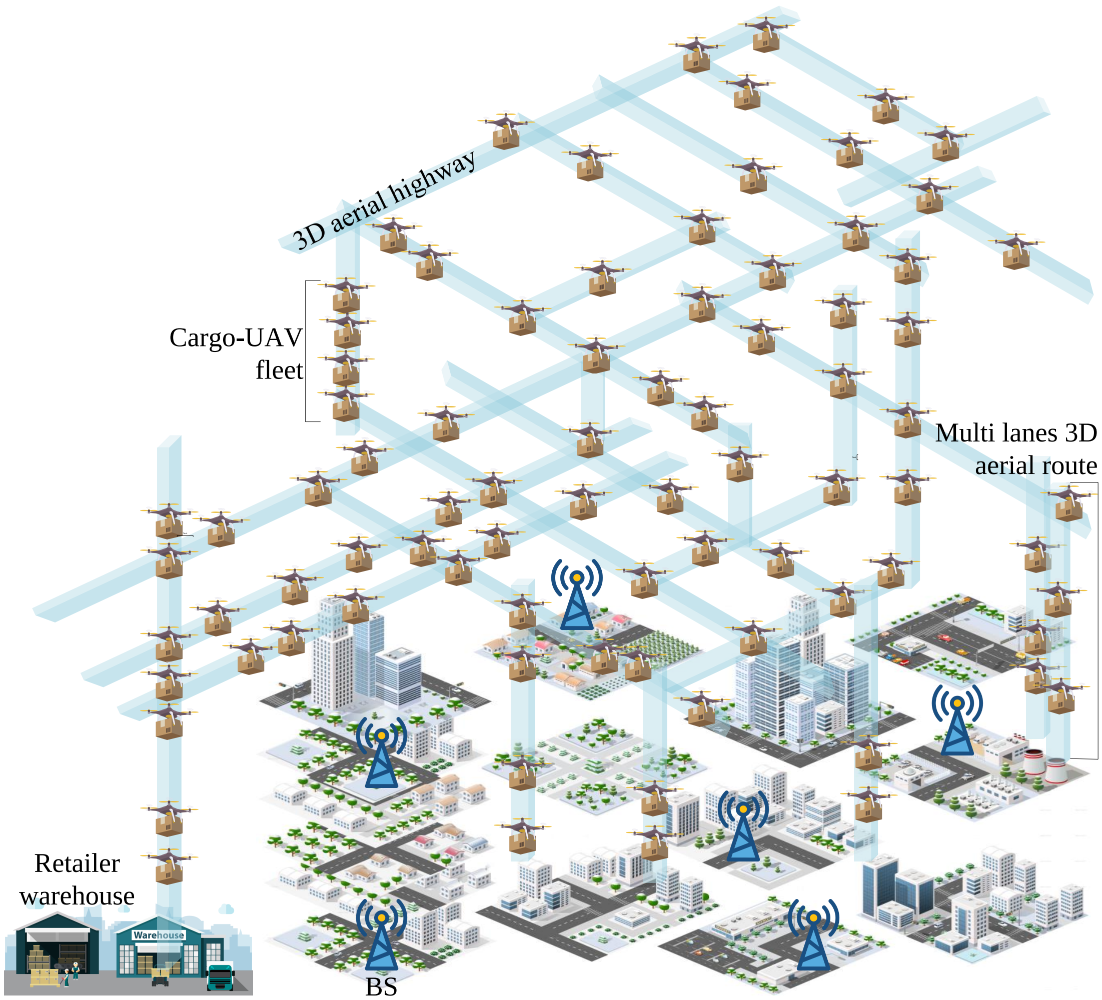

Fig. 5.1: A 3D aerial highway design.

ent altitudes according to specific criteria, e.g., cargo-UAV type, properties, and payload. Moreover, vertical routes are designed for easy transitions and uninterrupted cellular connectivity.

3D aerial highways present attractive characteristics. First, they are flexible and easily reconfigurable. Such qualities are handy in case of cellular network failures or out-of-control ground/sky layout modifications. Also, energy-efficient command-and-control can be achieved using cargo-UAV swarms. When a cargo-UAV fleet is deployed in an area, UAVs heading in the same direction can delegate a cargo-UAV to monitor all C&C exchanges, thus reducing the fleet's communications with the control center to a minimum. Finally, aerial highways can support different retailers.

5.2.2 UAV Regulations

Regulatory authorities developed guidelines for UAV usage that establish maximum UAV weight and altitude, purpose, and minimum spacing from individuals and sensitive services [12, Table I]. However, most guidelines apply to recreational UAVs only. Regulations for commercial UAVs should be more stringent, especially when carrying heavy loads as it may present safety risks. Hence, aerial highways above dense areas require adhering to several restrictions, e.g., no-fly zones, and safe flying above pedestrians and sensitive buildings.

5.2.3 Public Safety

Unlike conventional aviation operations, UAVs more likely experience failures. Studies demonstrated that UAV accident rates are very high, due to collisions with structures, aircraft, etc [76].

To reduce them, authorities limited the maximum UAV payload (below 30 kg) and flying altitude (below 122 m). When maliciously used, UAVs can trigger public service disruptions. For instance, more than 140,000 travellers were blocked due to UAV sighting at Gatwick Airport, UK in Dec. 2018. This incident revealed the extent to which UAVs can endanger daily life.

5.2.4 Privacy and Security

As UAV technology developed new applications, the privacy of individuals and communities become under threat. Indeed, cargo-UAVs equipped with sophisticated sensors and cameras are sensing and collecting data, such as location addresses and aerial photos. This data can be hacked or stored in offshore unsecured data-centres. Retailers, who operate their online deliveries via cargo-UAVs, are responsible for securing collected data and protecting it from cyber-attacks. Thus, the cargo-UAVs manager must deploy the most advanced and secured C&C exchange protocols, e.g., data encryption and blockchain-based data transmission, to guarantee not only the privacy and security of cargo-UAV data, but also the safety of humans and properties on the ground.

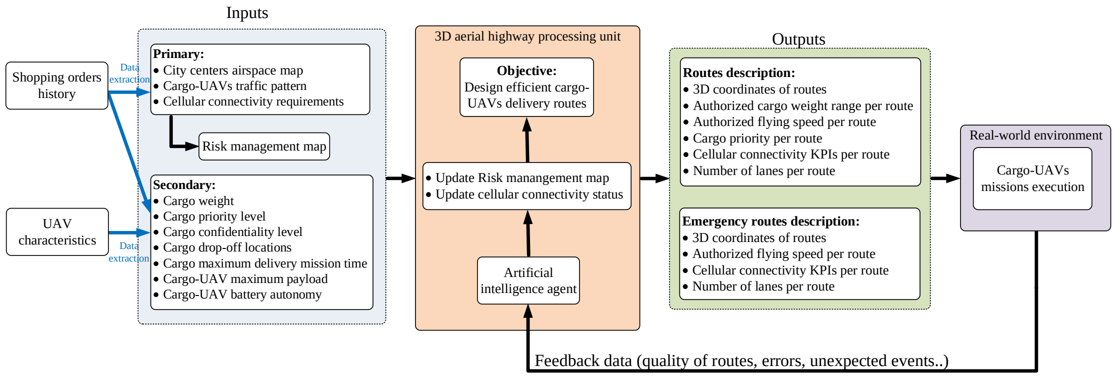

Fig. 5.2: Our vision of the 3D aerial highway design process.

5.2.5 Social Acceptability

The emergence of UAV-based applications has generated different responses from the public, which depended on the use-case. Specifically, risk assessment, privacy concerns, and job security impact, are the main factors influencing the social acceptability of the UAV technology. For instance, UAVs are positively perceived by farmers as they contribute for food security. However, their use in urban areas can be unwelcome due to impact on job losses and risk to properties and individuals. In a recent survey conducted on the public perception of UAVs [76], the respondents did not overrate the risk and threat of UAVs, compared to manned aircraft. However, privacy issues, military use, and UAV misuses emerged as prevalent concerns. The authors concluded that the perception of UAVs has yet to be formed and, as the technology matures, its acceptability will evolve positively.

5.3 3D Aerial Highway: Our Design Vision

Enabling massive cargo-UAV delivery requires rigorous 3D aerial highway design, where several parameters are considered. This design system sets up the regulatory routes that UAVs must follow when the latter plan their missions. This role can be attributed to a country's regulations entity, such as the FAA in the US. Due to the large sky volume to cover, the design process cannot be handled by a unique central entity. Alternatively, smaller geographical areas can be defined where several design entities can be deployed and each one manages the 3D aerial highways design in its specific geographical area. In such systems, neighbouring design entities exchange data in order to align their highways at the edges of their areas.

In Fig. 5.2, we depict the envisioned 3D aerial highway design process, including a description of the input parameters, processing unit, and output metrics.

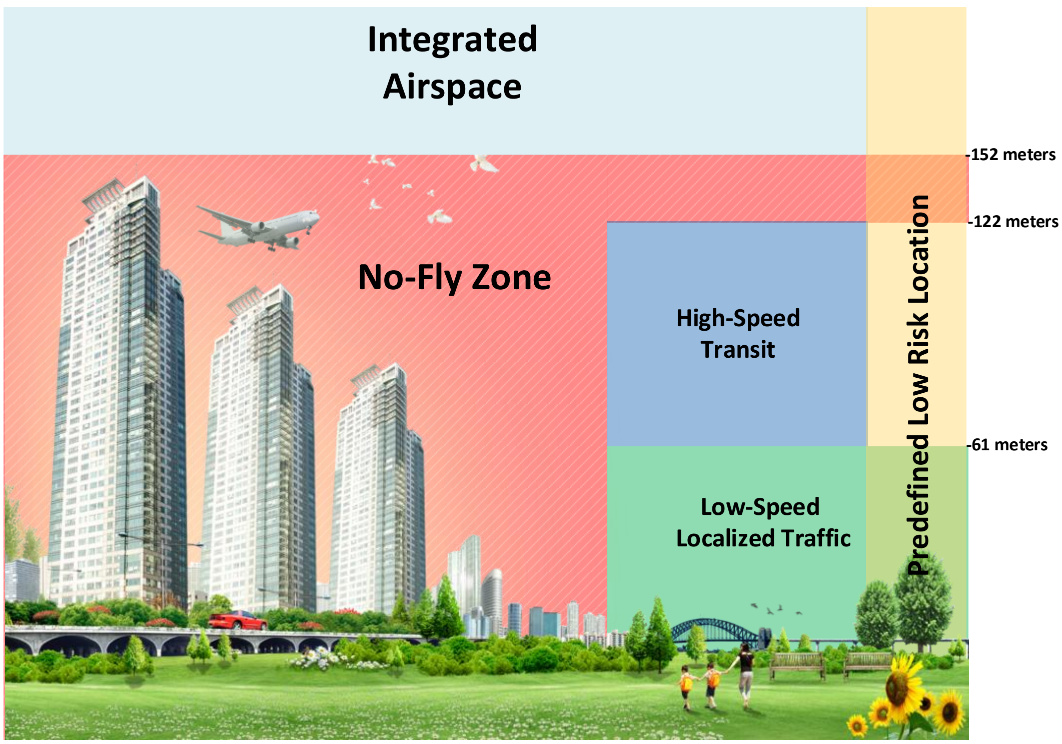

Fig. 5.3: Amazon's airspace segregation model.

5.3.1 Inputs

The 3D aerial highways design follows a two-step process, which rely on input data of high and low importance. Highly important data, called primary data, drives the selection of the airspace locations to serve as aerial routes, while data of low importance, a.k.a., secondary data, leads the association of the selected aerial routes to different cargo characteristics and UAV capabilities.

5.3.1.1 Primary Inputs

They are fundamental in defining the potential locations of aerial highways. They include:

- **City centres airspace map:** It is a mixture of the urban topography (i.e., buildings, streets) and defined areas of the airspace. These areas can be delimited as suggested by Amazon (Fig. 5.3). Specifically, cargo-UAVs operating beyond visual line-of-sight (BVLoS) travel in the "High-Speed Transit Zone", while recreational activities occur in the "Low-Speed Localized Traffic Zone". The airspace between 122 m and 152 m is a permanent "No-Fly Zone", except for emergencies. Finally, Amazon's model includes "Predefined Low Risk Locations", which are areas with minimal threat to individuals and properties, e.g., wooded areas and deserted fields.

- **Cargo-UAVs traffic pattern:** From shopping order history, traffic pattern can be extracted, which characterizes the density of order traffic by area. Thus, an area where the number of shopping orders is higher than average should be supplied by a higher number of routes to avoid aerial congestion.

- **Cellular connectivity requirements:** For BVLoS operations, reliable cellular connectivity would allow C&C data exchange and cargo-UAV continuous localization, thus preventing any issue during missions. Connectivity requirements include mainly end-to-end communication delay (tens of milliseconds), and tolerable disconnectivity rate of the itinerary, defined as the ratio of disconnected flight duration to total flight time.

- **Risk management map:** Cargo-UAVs face several risks during delivery, such as physical attacks by projectiles or birds, or cyber attacks by aerial and ground adversaries. To reduce these risks, a *risk management map* is created and periodically updated based on feedback from cargo-UAVs. This map is designed and then readjusted to address public concerns by allowing cargo-UAVs to travel only in safe and secured routes.

5.3.1.2 Secondary Inputs

They are required to organize the potential routes. They are composed of:

- **Cargo weight:** Depending on the cargo weight, the latter will be assigned to a specific type of UAV that handles it and will follow an itinerary composed of routes dedicated to this range of weights.

- **Cargo priority level:** Cargo may have different priority levels (e.g., standard, premium, or urgent), causing the delivery to be scheduled differently and/or put on a different priority itinerary. For instance, premium cargo can be delivered in a shorter time by traveling in more direct priority routes, while urgent cargo have access to routes in the "No-Fly Zone".

- **Cargo confidentiality level:** Cargo content may have different levels of confidentiality. Delivering official documents to citizens (e.g., passports, government ID) should be treated with high security measures. As such, UAVs must be equipped with high-end encryption protocols and use the safest aerial routes to guarantee mission integrity.

- **Cargo drop-off locations:** Aerial routes are expected to link the retailer warehouse to any possible shipping address within the UAV's flying range. For neighborhoods with heavy delivery traffic and hard access to private addresses, a common "drop-off location" can be established within a walking distance to simplify the delivery process.

- **Cargo maximum delivery mission time:** According to Amazon, consumers expect delivery within two hours or the same day.

  Consequently, significant pressure is put on the delivery process, where the maximum cargo-UAV delivery time, since leaving the warehouse until delivery, becomes crucial to the end-to-end shopping experience.

- **Cargo-UAV maximum payload:** Available UAVs for cargo transportation have different payload capabilities, ranging from few hundred grams to hundreds of kilograms. However, current regulations limited the total payload of the UAV, including cargo, to 30 kg, due to safety concerns of heavy-weight cargo. Subsequently, routes for different ranges of cargo weights, shapes, and solidity have to be defined.

- **Cargo-UAV battery autonomy:** The on-board battery lifetime is a limitation to consider in the design of aerial routes. Intuitively, more direct routes should be designed for farther drop-off locations.

5.3.2 3D Aerial Highway Design Processing Unit

The processing unit is the core of the 3D aerial routes design system. Its main role is to design and sustain the aerial highways. The process of designing aerial highways undergoes two steps as follows:

1. **Initial design:** Based on the input data, the processing unit designs 3D aerial highways, which are identified with start and end 3D coordinates. This process is conducted while aiming to maximize a multi-objective function that involves utility functions reflecting the stability of aerial highways in terms of safety, security, connectivity, and taking into account cargo characteristics and UAV capabilities.

2. **Design update:** Since several cargo-UAV related parameters may change over time, such as the city landscape, the shopping patterns, the cellular connectivity, and the security risk, 3D aerial highways must be regularly reconfigured to keep sustaining the cargo-UAV operations efficiently. Practically, unexpected events and changes are fed back to the processing unit via the cargo-UAVs and analyzed using artificial intelligence. Specifically, reinforcement learning algorithms can be leveraged to understand the varying 3D aerial highways environment, optimize their creation and modification over time, and maximize the related multi-objective function.

5.3.3 Outputs

The processing unit produces several metrics, which are summarized as follows:

- **3D coordinates of routes:** As in road networks, aerial routes are identified mainly by their 3D coordinates. Each route occupies a 3D volume that delimits its boundaries. It can be used for several lanes with smaller 3D volume dimensions. The definition of a route's volume depends on the collision risk level of the area underneath it.

- **Cargo priority per route:** Each aerial route is assigned a priority level that, for convenience, would allow flying cargo with the same priority or higher.

- **Authorized cargo weight range per route:** Each aerial route supports a range of UAV payloads depending on altitude and regulations. For instance, heavy-payload UAVs travel in low-risk areas, i.e., with minimum ground damage risk for pedestrians and properties.

- **Authorized flying speed per route:** UAVs may move along aerial highways at different speeds due to their characteristics. To reduce collision risk, routes can be divided for different speed ranges, e.g., fast, moderate, and slow, within the regulation limits.

- **Cellular connectivity KPIs per route:** Each route will be characterized by cellular connectivity KPIs, that are expected to exceed the requirements provided by inputs.

- **Number of lanes per route:** Dense neighborhoods may have a large number of cargo deliveries, thus, aerial routes may need to support this substantial number. Hence, designing several lanes per route shortens the delivery time. To avoid collisions between cargo-UAVs in adjacent lanes, the 3D volume of each lane should be delimited to the size of cargo-UAVs, while providing enough motion flexibility to avoid dynamic obstacles, e.g., birds and kites, within the lane's limits.

- **Emergency routes:** For unexpected events, e.g., extended cellular disconnectivity and UAV malfunctioning, the cargo-UAV should rapidly update its itinerary and switch to the reserved emergency route for safe pull-back to a designated ground station. Moreover, due to their robust communication links and high-level safety, with respect to the *Risk management map*, emergency routes can be used to transport critical supplies in case of natural disasters or life-threatening situations.

5.4 Cellular Connectivity for 3D Aerial Highways: A Close Look

In this section, we focus on cellular connectivity of cargo-UAVs in 3D aerial highways. Specifically, we discuss different architectures that guide the design of aerial highways for massive cargo-UAV operations.

5.4.1 Existing Terrestrial Network

Since terrestrial networks were designed to cover terrestrial users, their aerial coverage is unreliable as there are many coverage holes in the sky. Moreover, UAV may be affected by the strong line-of-sight (LoS) interference from other terrestrial-BSs (3GPP TR 36.777).

In Fig. 5.4, we depict the aerial coverage of terrestrial BSs for a cargo-UAV, where the downlink communication is considered successful when the SIR is above a threshold of 5 dB. We can see that there are most likely gaps in aerial coverage. Moreover, we notice that the cargo-UAV is served by BS antenna's side-lobe, e.g., BS 10.

5.4.2 Dedicated Terrestrial Network

As in aviation, where all communications are supported by dedicated terrestrial networks, cargo-UAVs traveling in 3D aerial highway can be served by a similar cellular network

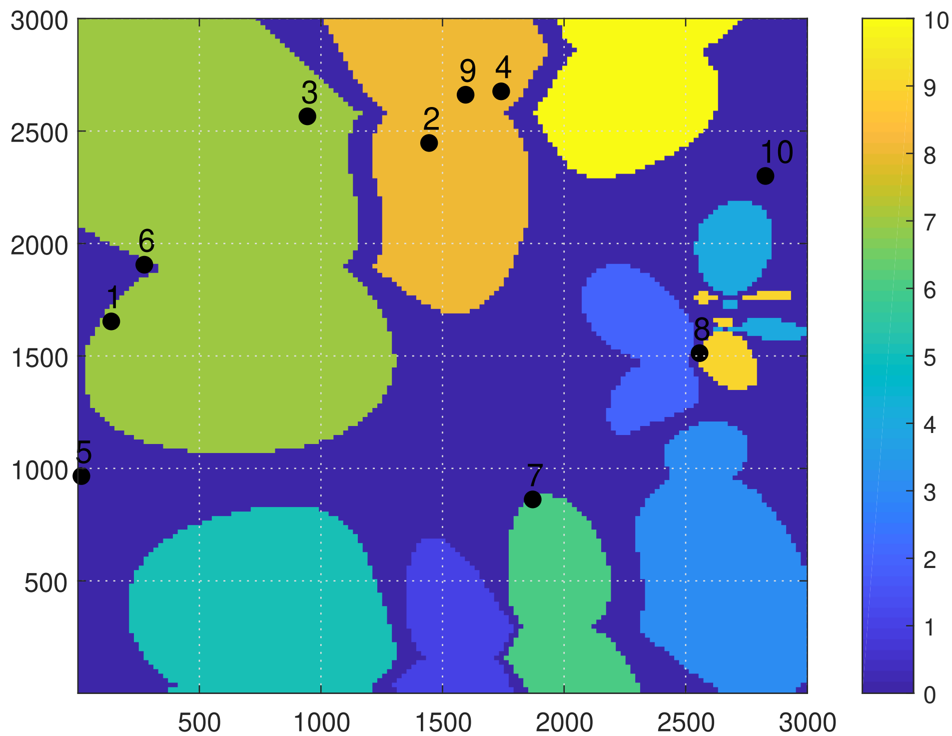

Fig. 5.4: Map of the strongest BS signal per cargo-UAV position. Area of 3000×3000 m^2 in an urban macro (UMa) environment (3GPP 36.777), where 10 terrestrial-BSs with 3D antenna radiation patterns are deployed (3GPP 38.901). Cargo-UAVs fly at 80 meters altitude.

design. To this end, terrestrial-BSs with antennas tilted up to the sky can be deployed to cover aerial routes. However, the coverage of such a dedicated network may face significant challenges when the aerial routes are dynamically reconfigured due to traffic pattern changes or unforeseen events. For instance, when a route starts to be congested with a high number of cargo-UAVs, new lanes and/or routes have to be rapidly configured to support this additional traffic load. The cellular connectivity for the new routes has to be guaranteed, which means that terrestrial-BS coverage of the sky has to be potentially reconfigured. Such flexibility may not be available with a dedicated terrestrial network. Furthermore, this option may not be the most economically attractive due to the need for high capital and operational expenditures.

Table 5.1: Comparison between different types of cellular networks for cargo-UAV connectivity

Type of network	Pros	Cons
Existing terrestrial network	• $0 deployment cost • Mature technology • Reliable backhaul links	• Limited cellular aerial coverage • Fixed deployment of BSs • Complex management for aerial and ground users
Dedicated terrestrial network	• Strong cellular aerial coverage • Mature technology • Reliable backhaul links	• Costly and fixed BS deployment • Complex management for dynamic 3D aerial routes
UAV-BS aerial network	• Easy and quick on-demand deployment • Reliable cellular coverage for aerial routes • Flexible reconfiguration for dynamic 3D aerial routes	• Potentially unstable backhaul links • Limited on-board processing power • Limited flight duration of UAV-BSs
LEO satellite network	• Ubiquitous cellular coverage • Potentially supports low-latency links (LEO round trip delay between 2.66 ms and 13.33 ms [77, Table I])	• Several challenges still unresolved • Potentially unstable backhaul links
HAPS aerial network	• Quasi-static location and operation for long periods of time (up to 6 months) • Reliable wide cellular coverage • Easy location update • Potentially supports low-latency links (HAPS round trip delay between 0.13 ms and 0.33 ms [77, Table I])	• Potentially unstable backhaul links • Limited on-board battery capacity

5.4.3 UAV-BS Aerial Network

Recently, the use of UAV-BSs to provide cellular connectivity has gained attention since promoted as complementary to terrestrial networks in several use-cases. For instance, when a spike in data rate demand occurs due to a temporary event, e.g., a concert or sporting event, UAV-BSs can be easily deployed to support the extra traffic load. In cargo-UAV systems, connectivity can also be supported by UAV-BSs. Specifically, the latter can be placed strategically along aerial routes to provide connectivity. In such a design, the UAV-BS antenna main-lobes have to be aligned with the cargo-UAV routes. When new routes are configured, mobility of UAV-BSs allows to move to more adequate locations, thus guaranteeing connectivity for cargo-UAVs along new routes.

Although UAV-BSs have extra degrees-of-freedom, i.e., deployment flexibility and mobility, they suffer from limited flying times, which complicates their utility. To bypass these constraints, researchers and industry players are investigating several options, including on-demand deployments depending on cargo-UAV traffic, on-the-fly UAV-BS swapping, laser charging, and tethered UAV-BSs that use permanent cables for energy supply and backhauling.

5.4.4 LEO Satellite Network

With the evolution of space technology today, the costs of satellite production and deployment are significantly reduced. This has made LEO satellites more attractive for providing ubiquitous and low-latency communications. SpaceX has taken the lead with Starlink project, which aims to deploy thousands of LEO satellites to provide Internet connectivity worldwide. In the context of 3D aerial highways, such a network design would be beneficial, especially in rural and hard-to-reach areas. However, for UAV applications, LEO communications face several challenges that need to be resolved. For instance, satellite pointing loss due to satellite vibrations or imperfect tracking-and-stabilization mechanisms may affect the quality of communications.

Moreover, LEO user-equipment may be hard to install and operate. Indeed, current LEO user-equipment requires mechanical satellite tracking, which tends to be hard when mounted on an energy-limited and moving UAV. These challenges have yet to be resolved to enable LEO satellite-connected UAVs.

5.4.5 HAPS Aerial Network

An interesting alternative to LEO satellites is a HAPS system, which offers similar performance with fewer constraints. In recent publications, HAPS have been proposed to act as super macro-BSs with large coverage footprints (up to 100 km) [77]. HAPS systems operate in the stratosphere at the typical altitude of 20 km, fueled mainly by solar panels and rechargeable batteries. They can be of different types, such as balloons, blimps, and aircraft [78, Table IV]. They can stay aloft at a quasi-stationary location, thus providing significant benefits over LEO satellites to achieve the goal of ubiquitous connectivity. The deployment of HAPS was initially planned for rural areas and disaster relief applications. However, the economical viability of HAPS is a main concern for its success. For instance, Google's Loon project was recently shut down due to its risky investment and poor turnover. Nevertheless, its legacy is transferred to a more ambitious project, which is the HAPSMobile project. In industry, several HAPS start-ups are leading the way towards high-speed connectivity from the stratosphere, including Thales Alenia Space and Stratospheric Platforms Limited. In the context of 3D aerial highways, HAPS would provide connectivity for a massive number of cargo-UAVs in rural and urban areas, which is expected to generate high income for several HAPS-based applications such as aerial delivery, aerial taxis, and intelligent transportation services. Owing to these capabilities, HAPS systems can act as an adequate cellular connectivity platform for cargo-UAVs traveling in 3D aerial highways, since a HAPS can guarantee a reliable wide coverage with relatively low-latency, especially in densely-populated areas where thousands of cargo-UAVs are expected to be flying around daily. Nevertheless, HAPS main concern lays in its limited on-board energy, needed mainly for propulsion and communication. Hence, advancements in battery technologies will enable the full potential of HAPS in connecting massive cargo-UAV systems and support future "intelligent aerial transportation systems".

5.4.6 Coverage Probability Evaluation

By leveraging tools from stochastic geometry, we present in Fig. 5 the coverage probability performance of a typical cargo-UAV operating in a 3D aerial highway and for different network types, namely the terrestrial LTE and mmWave networks, the HAPS network, and two VHetNets where the first deploys terrestrial LTE BSs and UAV-BSs, while the second uses terrestrial LTE BSs and HAPS. First, the LTE network provides poor coverage at low altitudes. This is mainly due to blockages such as highrise buildings and trees. Starting from altitude 125 m, the coverage probability improves as the communication exhibits a higher LoS. In contrast, the mmWave network, which operates at frequency 38 GHz and leverages 3D beamforming, behaves inversely to the LTE network, i.e., it demonstrates strong performances at low altitudes due to the low path loss and high antenna gains, but exhibits a low coverage probability at high altitudes caused mainly by a higher path loss impact with distance at high frequencies [79]. Using HAPS, the cargo-UAV enjoys a ubiquitous coverage at any altitude due to the HAPS inherent characteristics providing a wide coverage range of dozens to hundreds of kilometers around [78]. Since UAV-BSs complement the terrestrial BSs' coverage, VHetNet (LTE & UAV-BSs) achieves acceptable

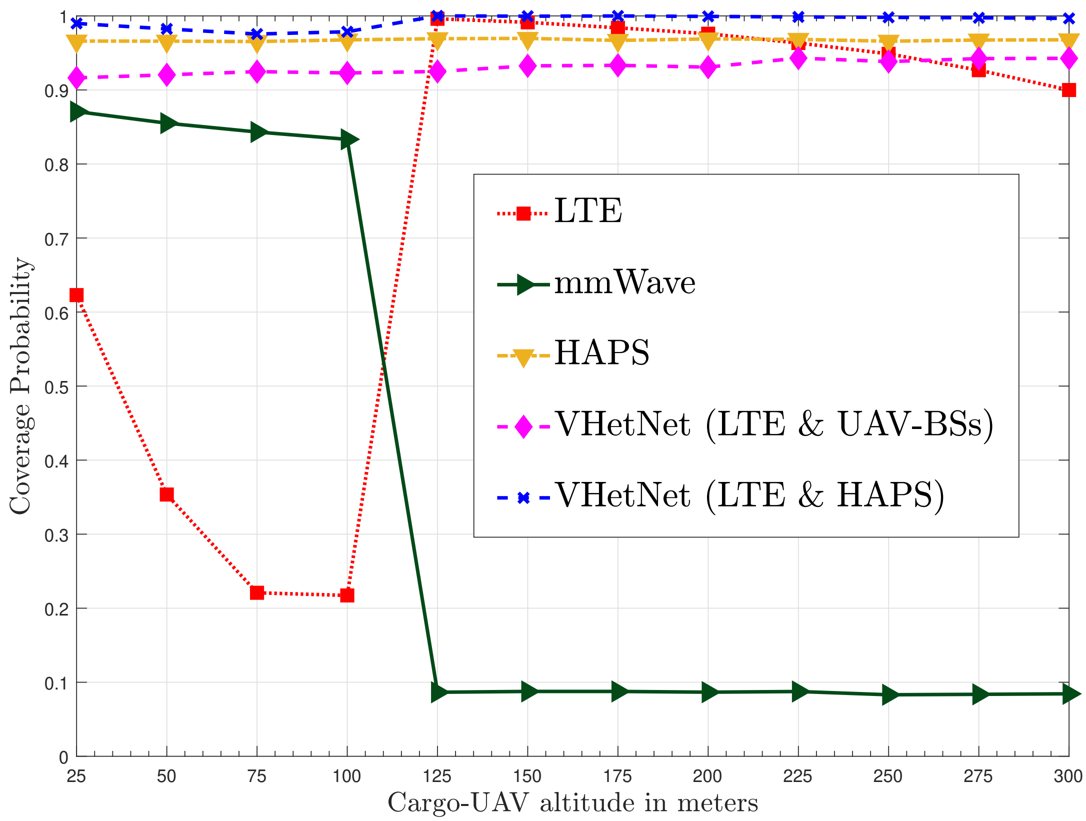

Fig. 5.5: Coverage probability vs. cargo-UAV altitude.

performance, which is close to that of HAPS. Finally, VHetNet (LTE & HAPS) outperforms all network types by providing ubiquitous and reliable coverage at any altitude. Specifically, the latter favors HAPS coverage at low altitudes and LTE coverage at high altitudes, as this strategy guarantees strong LoS communication links. Obviously, if cargo-UAVs have to rely on a single network type for connectivity, the HAPS would be the most adequate choice, while full coverage probability is achieved thorough VHetNet (LTE & HAPS).

In summary, each of these networks has its advantages and drawbacks in providing cellular connectivity for the 3D aerial highway paradigm. Nevertheless, we envision that a practical deployment for cargo-UAVs will be supported by at least two different types of networks, which will provide reliable connectivity and safe operation in the airspace. Specifically, routes can be designed with a prior knowledge of the coverage edges and locations for intra-network and inter-network handovers. Subsequently, a cellular-connectivity strategy can be pre-designed. As the cargo-UAV's trajectory may change during the mission, unexpected disconnectivity events trigger on-board network search to lock on an available network and receive updates for its connectivity strategy. When extended disconnectivity occurs, it must follow the emergency route for the time to reestablish connectivity and update its strategy. For the sake of clarity, we provide the pros and cons of these solutions in Table 5.1.

5.5 Conclusion

In this article, we presented our vision of a 3D aerial highway paradigm, which will be the main enabler of the retail industry transformation. First, we highlighted its main motivations and concerns. Then, we detailed our 3D aerial highway design process that enables the coordinated and dynamic planning of routes for cargo-UAVs. Finally, we discussed the related issue of cellular connectivity and evaluated possible solutions. For 3D aerial highways to operate safely and effectively, we recommend supporting cargo-UAVs with at least two types of wireless networks.

Chapter 6

Disconnectivity-Aware Energy-Efficient Cargo-UAV Trajectory Planning with Minimum Handoffs

6.1 Introduction

Cargo unmanned aerial vehicle (cargo-UAV) is a popular mean of delivery, especially for remote and hard-to-reach areas [18]. Due to the technological advancements that made cargo-UAVs safer and cost-efficient, it is expected that the latter be deployed in dense urban centres [3]. Since cargo-UAVs operate at BVLoS, C&C is crucial in ensuring the safety and security of the mission [12]. The latter relies on cellular networks, which have to be reliable enough for safe operation. Several works have investigated the practicality and feasibility of BVLoS cellular-connected UAVs [80–82].

This work has been published in IEEE ICC 2021 proceedings:**N. Cherif**, W. Jaafar, H. Yanikomeroglu, and A. Yongacoglu, "Disconnectivity-aware energy-efficient cargo-UAV trajectory planning with minimum handoffs", *IEEE International Communications Conference* (ICC), Montreal, Quebec, Canada, Jun. 2021, pp. 1-6.

Reusing the terrestrial networks for cargo-UAV cellular connectivity presents its own set of challenges as these networks were primarily designed to serve ground users only [3]. Although economically attractive, it may be difficult to provide reliable and seamless cellular connectivity to the cargo-UAVs, especially at high altitudes. Indeed, terrestrial base stations (BSs) are down-tilted, which means that cargo-UAVs can be served only through the sidelobes of BS antennas [17, Fig. 6]. Moreover, the cargo-UAV's inherited mobility leads to frequent switching from one serving BS to another, i.e., handoff. As such, an additional amount of information is exchanged, which degrades further the transmission link. Even though the energy consumption related to the communication overhead is relatively small compared to the cargo-UAV's motion energy, handoff events should be kept to the minimum in order to guarantee the C&C stability. Due to the aforementioned factors, occasional cellular disconnectivity can be experienced by cargo-UAVs operating in BVLoS. Depending on the criticality of the mission and the level of autonomy, a cargo-UAV can tolerate an end-to-end disconnectivity rate, defined as the ratio of the time spent disconnected from all cellular BSs to the total mission time.

In order to keep low handoff and disconnectivity rates, cargo-UAV trajectory planning became significantly important in BVLoS missions. This problem has attracted many researchers for the last few years. For instance, the authors of [83] set up a testbed for cellular-connected UAV missions in the sky. Their qualitative study showed that handoff occurs more frequently for UAVs, compared to terrestrial users. Hence, proper UAV motion optimization is needed to reduce handoffs. A cellular disconnectivity-aware trajectory design was proposed in [84]. However, the authors relied rather on a simplistic C2A propagation model that does not reflect the real 3D radiation patterns of BSs. In contrast, the authors of [85] studied the effects of both realistic 3D antenna radiation and limited backhaul on the UAV trajectory planning problem. Yet, this work lacked the insights on the handoff and disconnectivity rates during UAV missions. Recently, reinforcement-learning based trajectory planning solutions have been proposed for energy-efficiency maximization [86], mission time minimization [87], and route distance minimization [88]. However, none of these works has accounted for the UAV energy consumption, cellular disconnectivity, and handoffs, altogether. This has been investigated for the first time in [89], where a multiarmed-bandit based UAV velocity strategy is proposed for a predefined trajectory, and under a weighted handoff rate, cellular disconnectivity, and power consumption objective. However, the trajectory was not optimized with consideration of these factors.

Given the limitations of the aforementioned works, we study in this Chapter the disconnectivity and handoff aware trajectory planning problem for cargo-UAVs. Specifically, we aim to minimize the UAV's energy consumption and handoff rate, with respect to the battery size and disconnectivity rate. Due to the problem's complexity, we propose a dynamic programming (DP) based solution that provides reliable cargo-UAV trajectories. Through simulations, the efficiency of our method is demonstrated. Finally, by evaluating the impact of several parameters, e.g., cellular connectivity conditions and UAV altitude, we provide design guidelines for cargo-UAV operations.

6.2 System Model

We assume a geographical area with its airspace, defined through a 3-dimensional (3D) axes system (x, y, z). As per the 3GPP report [2], a cargo-UAV is allowed to hover/fly at a maximum altitude of 300 m above the ground level. We assume that the cargo-UAV mission is to deliver an item from a retailer's warehouse, located in (x_s, y_s) in the (x, y) plane to a consumer's drop-off location (x_d, y_d). We envision that the cargo-UAV hovers vertically from the warehouse's dockstation until it reaches the desired altitude $h \leq 300$ m at coordinates $\text{START} = (x_s, y_s, h)$, then it travels horizontally with a fixed velocity v to reach the destination point, defined as $\text{END} = (x_d, y_d, h)$. Finally, the cargo-UAV lands vertically to the drop-off location (x_d, y_d).

We assume that the cargo-UAV is exclusively served by the terrestrial cellular network. The latter is constituted of M BSs, where the location of the i^{th} BS is denoted by $(x^i_{\text{BS}}, y^i_{\text{BS}}, z_{\text{BS}})$. The height of the BS depends on the type of environment, which is selected from 35 m, 25 m, and 10 m, for rural macro (RMa), urban macro (UMa), and urban micro (UMi), respectively.

6.2.1 C2A Channel Model

The C2A channel model is outlined in the 3GPP reports [2, 56]. It considers several parameters, including the BS's antenna gain, LoS probability, and path-loss.

6.2.1.1 BS Antenna Gain

As mentioned previously, UAVs in the sky are mainly connected to BSs through the radiating sidelobes. Hence, accurately modelling the BS 3D antenna radiation pattern is needed for accurate trajectory planning. In this work, we adopt the 3GPP antenna pattern model that mimics realistic antenna patterns [56]. That means, each BS is divided into three sectors, where a sector is equipped with cross-polarized antennas to form a uniform linear array (ULA). Each antenna element provides a gain up to $G_{\max}$ (typically 8 dBi) in the direction of the mainlobe. The antenna element pattern is given by [56, Table 7.1.-1], which provides certain gains depending on the azimuth and elevation angles of the cargo-UAV with respect to the BS's location. They are respectively given by

$$G_{\text{az}}(\phi_i) = \min\left\{12\left(\frac{\phi_i}{\phi_{3\text{dB}}}\right), G_m\right\}, \tag{6.1}$$

$$G_{\text{el}}(\theta_i) = \min\left\{12\left(\frac{\theta_i}{\theta_{3\text{dB}}}\right), \text{SLA}\right\}, \tag{6.2}$$

where $\phi_i = \tan^{-1}\left(\frac{h-z_{\text{BS}}}{d_{2D,i}}\right)$ and $\theta_i = \tan^{-1}\left(\frac{y-y^i_{\text{BS}}}{x-x^i_{\text{BS}}}\right)$ are the azimuth and elevation angles between the i^{th} BS and the cargo-UAV. Also, $d_{2D,i}$ is the horizontal distance between the i^{th} BS and the cargo-UAV, while $\phi_{3\text{dB}}$ and $\theta_{3\text{dB}}$ are the 3 dB bandwidths fixed at 65°. Furthermore, G_m and SLA are the thresholds for antenna nulls, fixed to 30 dB. Finally, the antenna element gain in dB is expressed by

$$G(\theta_i, \phi_i) = G_{\max} - \min\left\{-\left(G_{\text{az}}(\phi_i) + G_{\text{el}}(\theta_i)\right), G_m\right\}. \tag{6.3}$$

Assuming N antenna elements at BS i, equally distant by half of the wavelength, the array factor AF of the ULA with a down-tilt of θ_d can be given by [90, eq. (2)]

$$\text{AF}(\theta_i) = \frac{\sin\left(\frac{N\pi}{2}\left(\sin\theta_i - \sin\theta_d\right)\right)}{\sqrt{N}\sin\left(\frac{\pi}{2}\left(\sin\theta_i - \sin\theta_d\right)\right)},\ \forall i = 1, \ldots, M. \tag{6.4}$$

Finally, the array radiation pattern of the i^{th} BS is written by

$$G_i = G(\theta_i, \phi_i) + \text{AF}(\theta_i),\ \forall i = 1, \ldots, M. \tag{6.5}$$

6.2.1.2 LoS Probability

The probability that the cargo-UAV is in LoS condition with the BS depends mainly on the terrestrial environment and the cargo-UAV altitude. For instance, when 22.5 m $< h \leqslant$ 100 m, the probability of LoS, denoted $P_{\text{LoS}}(d_i)$ in UMa is given by [2, Table B-1]

$$P_{\text{LoS}}(d_i) = \begin{cases} 1, & d_{2D,i} \leqslant d_1 \\ \frac{d_1}{d_{2D,i}} + \exp\left(\frac{-d_{2D,i}}{p_1}\right)\left(1 - \frac{d_1}{d_{2D,i}}\right), & d_{2D,i} > d_1, \end{cases} \tag{6.6}$$

where $d_i = \sqrt{d_{2D,i}^2 + (h - z_{\text{BS}})^2}$ is the 3D distance between the cargo-UAV and the i^{th} BS, $p_1 = 4300 \log_{10}(h) - 3800$, and $d_1 = \max\{460 \log_{10}(h) - 700, 18\}$. When 100 m $< h \leq 300$ m, $P_{\text{LoS}}(d_i) = 1$. Finally, the NLoS probability is calculated as $P_{\text{NLoS}}(d_i) = 1 - P_{\text{LoS}}(d_i)$.

6.2.1.3 Pathloss Model

For the sake of simplicity, we follow the probabilistic pathloss model, as defined in [2, Tables B-1 and B-2]. The average pathloss of the channel between the cargo-UAV and the i^{th} BS, denoted L_i, is given by

$$L_i = P_{\text{LoS}}(d_i) L_i^{\text{LoS}} + P_{\text{NLoS}}(d_i) L_i^{\text{NLoS}}, \ \forall i = 1, \ldots, M, \tag{6.7}$$

where L_i^{LoS} and L_i^{NLoS} are the pathlosses related to fully LoS and NLoS communication links, respectively, defined in [2, Tables B-1 and B-2].

6.2.2 Received Power Analysis

Based on the C2A channel model and assuming that the cargo-UAV is equipped with an omni-directional antenna with unit gain, the average received power from the i^{th} BS is given by

$$P_{r,i} = P_T + G_i - L_i, \ \forall i = 1, \ldots, M, \tag{6.8}$$

where P_T is the transmit power of any BS in dBm.

The received power from a BS at any 3D location determines the quality of the transmission link. As discussed in [2], the airspace is an interference-limited environment since

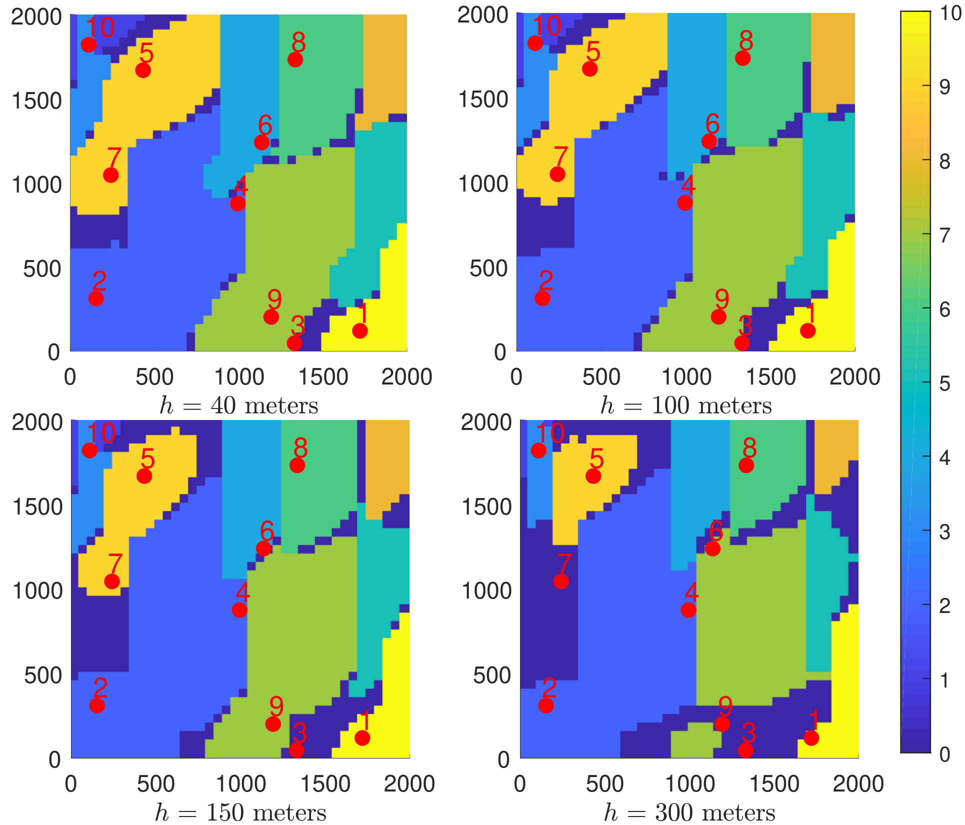

Fig. 6.1: Cellular connectivity heatmap for different cargo-UAV altitudes. Colors denote the IDs of the serving BSs. ID 0 (dark blue) defines the coverage holes ($\theta_d = -10°$, $f_c =$ 2 GHz, $v = 30$ m/s, and $\beta_{\text{th}} = 0$ dB).

a cargo-UAV may have cleared LoS conditions with several BSs using the same frequency resource at the same time[1]. Thus, we assume for simplicity that the cellular connectivity depends solely on the level of the SIR, defined by

$$\mathsf{SIR}_i = \frac{P_{r,i}}{\sum\limits_{j=1, j\neq i}^{M} P_{r,j}}, \ \forall i = 1, \ldots, M. \tag{6.9}$$

One location is presumed a *coverage hole* if SIR falls below a predefined threshold β_{th}.

Using (6.8), we depict in Fig. 6.1 the 3D cellular coverage of 10 BSs at different cargo-UAV altitudes. We assume here an area of 2×2 km^2, and the coverage at any 3D location

[1]In this Chapter, we investigate the full interference scenario. Nevertheless, frequency planning can be considered to reduce the number of inter-cell interferers.

is provided by the BS with the strongest SIR, i.e., $\mathsf{SIR} = \max_{i=1,\ldots,M} \mathsf{SIR}_i$. We notice that the coverage area of the BS 10 at the north-east corner (clear yellow color) is located at the south-east corner of the map. This observation corroborates the fact that BSs serve cargo-UAVs using the sidelobes. Moreover, the coverage holes widen while the coverage areas shrink as the cargo-UAV flies higher. This is due to the large pathloss and low antenna gain at high elevation angles.

6.2.3 Cargo-UAV Energy Model

The energy consumed by a cargo-UAV depends on its size, weight, and power (SWAP), in addition to its motion and communication regimes [91]. It is composed of the propulsion energy, needed for flying, and of the communication energy, for C&C operations. Typically, communication energy is very small compared to the propulsion energy, and thus, can be neglected. Using a rotary-wing cargo-UAV, the propulsion power can be given by [75]

$$\begin{aligned} P_{\text{prop}}(v) &= \frac{1}{2}\delta_0 \zeta r A v^3 + \sigma_B \left(1 + \frac{3v^2}{U_{\text{tip}}^2}\right) \\ &+ \sigma_I \left(\sqrt{1 + \frac{v^4}{4v_0^4}} - \frac{v^2}{2v_0^2}\right)^{\frac{1}{2}}, \end{aligned} \tag{6.10}$$

where σ_B and σ_I are the blade profile power and induced power, respectively. v_0 is the mean rotor induced velocity and U_{tip} is the speed of the tip of the rotor blade. Also, ζ is the air density, δ_0 is the fuselage drag ratio, r is the rotor solidity, and A is the rotor disc area. Subsequently, the propulsion energy to fly for a distance d is

$$E(v, d) = P_{\text{prop}}(v)\; d/v,\; v > 0. \tag{6.11}$$

We denote by E_C and E_S the initial cargo-UAV energy capacity and emergency reserve energy, respectively. E_C is available for the mission, while E_S is used in emergency pull-backs. Hence, the cargo-UAV available energy to travel between the START and END locations is

$$E_A(v, h) = E_C - E_S - 2E(v, h), \tag{6.12}$$

where $E(v, h)$ is the required energy for tackoff/landing up to/down to the dockstation/drop-off location. Thus, the maximum horizontal travelling distance is given by

$$d_{\max} = vE_A(v, h)/P_{\text{prop}}(v). \tag{6.13}$$

6.3 Problem Formulation

The cargo-UAV mission is to deliver an item from a warehouse to a consumer drop-off location. Assuming that the cargo-UAV flies at a constant speed and altitude h, we aim to design its mission trajectory such that: 1) it consumes the lowest energy, 2) it minimizes the handoff rate, 3) it does not exhibit a cellular disconnectivity rate above a fixed threshold $\alpha_{\max}$ during the mission. Based on the cellular connectivity heatmap shown in Fig. 6.1, a disconnectivity event happens when the cargo-UAV transits to/from an area with BS ID 0 (coverage hole), and the *disconnectivity rate* is calculated as the ratio of the time spent in areas with BS ID 0 to the total mission time. When the cargo-UAV transits from a coverage area to another (with BS IDs $\neq 0$), a handoff event occurs. Then, the *handoff rate* is calculated as the total number of handoff events during the mission. Let $\mathcal{T} = \{\mathbf{q}_1, \ldots, \mathbf{q}_{|\mathcal{T}|}\}$ be the trajectory of the cargo-UAV, defined by the locations $\mathbf{q}_i = (x_i, y_i, h)$. Also, let $\mathcal{S} = \{s_1, \ldots, s_{|\mathcal{T}|}\}$ be the set of BS IDs associated to the cargo-UAV locations in $\mathcal{T}$. Subsequently, the trajectory planning problem can be formulated as follows:

$$\min_{\mathcal{T}} \quad w_1 \sum_{i=1}^{|\mathcal{T}|-1} E(v, d_{i,i+1}) + w_2 \sum_{i=1}^{|\mathcal{T}|-1} \eta_{i,i+1} \tag{P1}$$

$$\text{s.t.} \quad \sum_{i=1}^{|\mathcal{T}|-1} E(v, d_{i,i+1}) \leq E_A(v, h), \tag{P1.a}$$

$$\frac{d_{\text{disc}}}{\sum_{i=1}^{|\mathcal{T}|-1} d_{i,i+1}} \leq \alpha_{\max}, \tag{P1.b}$$

where w_1 and w_2 are weight factors balancing between energy consumption and handoff rate. $d_{i,i+1} = \|\mathbf{q}_i - \mathbf{q}_{i+1}\|$, d_{disc} is the sum of flying distances in coverage holes, and $\eta_{i,i+1}$ is a binary variable reflecting the handoff event, i.e., $\eta_{i,i+1} = 1$ if $s_i \neq s_{i+1}$ and $(s_i, s_{i+1}) \neq (0, 0)$, and $\eta_{i,i+1} = 0$ otherwise. Problem (P1) is NP-hard. Indeed, the latter can be seen as the capacitated vehicle routing problem (CVRP) [92]. The CVRP is described as selecting the route for a vehicle, aiming to serve a group of customers. The vehicle has a limited capacity, which is used to depart from a depot point, serve a number of customers along its route, then return to the same or a different depot point. The objective of the CVRP is to minimize the total transport costs. Logically, the vehicle, customers, and transport costs, can be assimilated by the UAV, BSs, and (energy consumption + handoff rate),

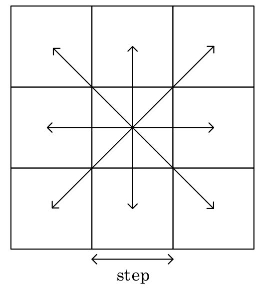

Fig. 6.2: Motion options for the cargo-UAV in one step.

respectively. Since the CVRP is known to be NP-hard [92], then by restriction, (P1) is also NP-hard.

6.4 Proposed Solution: DP Algorithm

In this section, we adopt, similarly to [84], the dynamic programming approach to derive a near-optimal trajectory solution for (P1).

First, we start by dividing the plane (x, y) at altitude h to a grid of cells, numbered from 1 to J. We assume that the cargo-UAV can move in one step from the center of one cell to the center of an adjacent cell in one of the available directions, i.e., one of 8 movements can be realized as shown in Fig. 6.2. We define by $\mathcal{T}_j$, $\mathcal{S}_j$, d^j_{disc}, and E_j the best trajectory to reach cell j (with respect to energy and disconnectivity constraints), the corresponding set of BS IDs, the sum of flying distances in coverage holes to reach cell j when following trajectory $\mathcal{T}_j$, and the associated cargo-UAV consumed energy, respectively. Thus, for any cell j, the objective function can be computed as

$$O_j(t) = \min_{j' \in \mathcal{N}_j} \left\{ O_{j'}(t-1) + w_1 E(v, d_{j',j}) + w_2 \eta_{j',j} \right\}, \tag{6.15}$$

$$\text{such that } E_{j'} + E(v, d_{j',j}) \leq E_A; \ \frac{d^j_{\text{disc}}}{\sum\limits_{i=1}^{|\mathcal{T}_j|-1} d_{i,i+1}} \leq \alpha_{\max},$$

where t is the stage in the optimization process, $\mathcal{N}_j$ is the set of neighbouring cells to cell j, $\eta_{j',j}$ is the binary variable indicating a handoff event, and

$$O_j(t) = w_1 \sum_{i=1}^{|\mathcal{T}_j|-1} E(v, d_{i,i+1}) + w_2 \sum_{i=1}^{|\mathcal{T}_j|-1} \eta_{i,i+1}, \ \forall j. \tag{6.16}$$

Eq. (6.15) states that if the cargo-UAV can reach the j^{th} cell from a neighboring cell while 1) minimizing the objective function, 2) not exceeding the available on-board energy, and 3) not exceeding the disconnectivity rate threshold, then, the new optimal trajectory is from that neighboring cell. When repeated with a sufficient number of iterations, this step provides the optimal trajectory.

In Algorithm 6.1, we present the pseudocode for the DP-based trajectory planning method. In lines 2 and 3, the minimum cost path matrices are initialized and computed. Then, the stage cost matrices are initialized in lines 4 and 5, where the initial cost of the START cell is set to zero. In line 6, we generate the matrix in which we will store the optimal cells indices guaranteeing the smallest costs. Lines 7 to 21 execute the DP algorithm iterations, where the battery, cellular disconnectivity, and handoff constraints are handled in line 13. Then, the solution is refined with a smaller cost at each iteration, as shown in line 14. Finally, the optimal path is extracted recursively in the procedure of lines 22 to 31.

6.5 Simulation Results

In this section, we evaluate the performance of the cargo-UAV DP-based path planning solution. Unless stated elsewhere, we assume here 10 BSs deployed in an UMa environment using the pathloss model of [2, Table B-1]. As shown in Fig. 6.3, the START and END locations for the cargo-UAV mission are selected in the two opposite corners of the map. We set the following parameters to $G_{\max} = 8$ dBi, $\theta_d = -10°$, $P_T = 43$ dBm, $v =$ 30 m/s, $E_C - E_S = 2500$ kJ, and $w_1 = w_2 = 1$. Finally, typical values of the cargo-UAV related parameters are taken from [75, Table I].

In Fig. 6.3, we illustrate the resulting cargo-UAV paths using Algorithm 6.1, given different values of the tolerated disconnectivity $\alpha_{\max}$. The dark blue color refers to the coverage holes, while the other colors correspond to the coverage areas of 10 BSs, located as shown in Fig. 6.1. As $\alpha_{\max}$ decreases, we see that the followed path is longer. Indeed,

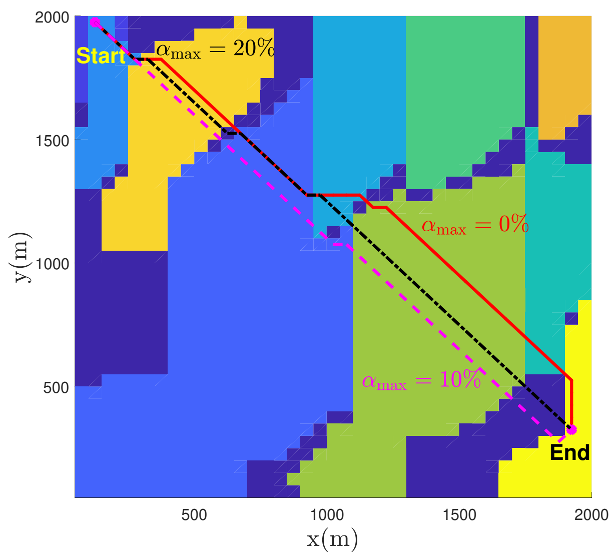

Fig. 6.3: Cargo-UAV paths ($h = 200$ m, different $\alpha_{\max}$).

the UAV needs to make detours in order to avoid partially ($\alpha_{\max} > 0\%$) or completely ($\alpha_{\max} = 0\%$) the coverage holes.

Fig. 6.4 shows the consumed energy rate, defined as the ratio of the consumed energy for the mission to the available energy $E_C - E_S$, for the setup of Fig. 6.3. This performance metric is evaluated as a function of the flying altitude h and for different disconnectivity rates $\alpha_{\max}$. As $\alpha_{\max}$ becomes more stringent, the cargo-UAV consumes more energy in order to execute detours and avoid coverage holes, thus agreeing with the results of Fig. 6.3. Also, the energy consumption increases with the altitude. Indeed, in addition to the energy consumed between START and END locations, the cargo-UAV has to spend more effort in takeoff and landing to reach them.

In Fig. 6.5, we present the handoff rate as a function of h and for different $\alpha_{\max}$, given the setup of Fig. 6.3. We notice no clear trend or correlation can be identified between the handoff rate and the cargo-UAV altitude. However, the handoff rate increases as $\alpha_{\max}$ decreases, given a fixed h. Indeed, as $\alpha_{\max}$ nears zero, i.e., no disconnectivity is allowed, the cargo-UAV is required to follow paths that avoid coverage holes, i.e., it is more likely to trigger handoff events when travelling.

Fig. 6.6 illustrates the average handoff rate (over different cargo-UAV altitudes) as a

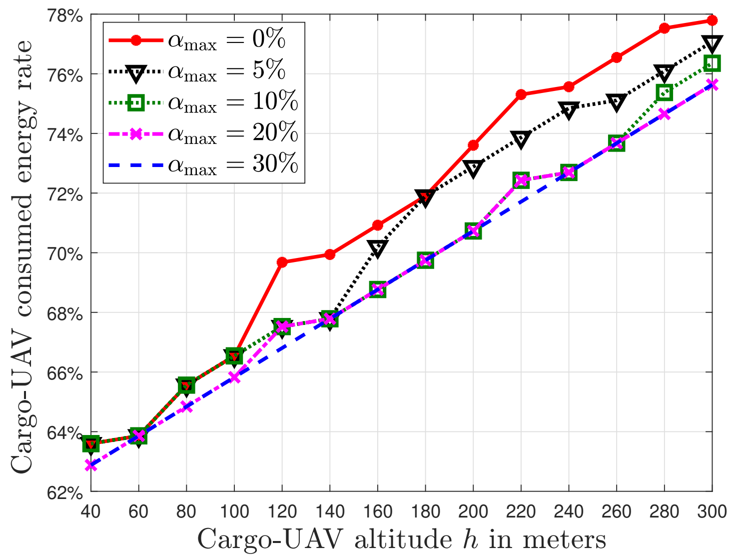

Fig. 6.4: Consumed energy rate vs. h (different $\alpha_{\max}$).

function of $\alpha_{\max}$, and for different SIR threshold values β_{th}. As $\alpha_{\max}$ increases, the handoff rate improves. Indeed, with $\alpha_{\max}$ loosened, the cargo-UAV can cross a higher number of coverage holes, which does not account for handoff events. In contrast, a stringent $\alpha_{\max}$ obligates the cargo-UAV to move only within the BSs' coverage areas, thus increasing the handoff rate. Moreover, the handoff rate degrades as β_{th} decreases. In fact, a small β_{th} means that a small number of (or no) coverage holes are present within the network. Thus, the cargo-UAV experiences frequent handoffs when travelling. Finally, we notice that the average handoff rate is independent from $\alpha_{\max}$ when $\beta_{\text{th}} = -5$ dB. Indeed, for this β_{th} value, no coverage holes are present, and hence no disconnecitvity is encountered in the cargo-UAV path.

We investigate in Fig. 6.7 the average consumed energy rate as a function of $\alpha_{\max}$, for different types of environments, namely UMa, UMi, and RMa, characterized by the BSs density λ, and where the results are averaged over 200 Monte-Carlo realisations of BSs locations. First, the energy performance improves with $\alpha_{\max}$ in any environment type. This is expected since a more direct path is followed by the cargo-UAV for higher $\alpha_{\max}$. Second, RMa achieves the best consumed energy rate for any $\alpha_{\max}$. Indeed, in RMa, a small number of BSs is used, which limits inter-cell interference and hence improves the coverage of the BSs. Consequently, short paths are followed by the cargo-UAV to reach its

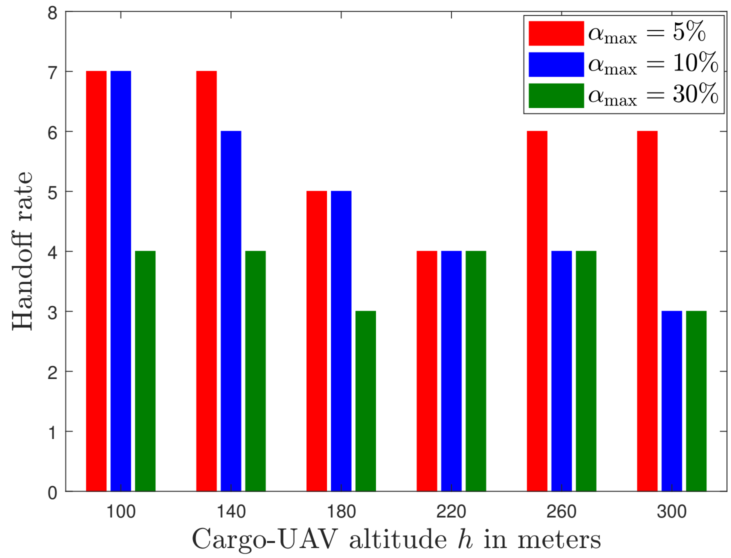

Fig. 6.5: Handoff rate vs. h (different $\alpha_{\max}$).

destination. However, as the environment becomes denser with BSs, the impact of inter-cell interference amplifies due to LoS links, causing a significant degradation to communication channels and coverage areas. Hence, the cargo-UAV has to make detours in order to reach its destination with respect to $\alpha_{\max}$.

6.6 Conclusion

In this Chapter, we investigated the disconnectivity and handoff aware path planning problem for the cargo-UAV, aiming to minimize both its energy consumption and handoff rate. The formulated complex problem is solved using a dynamic programming approach, which achieves optimal flying trajectories. Through simulations, we establish the relationship between cellular disconnectivity and handoff rate for aerial communications. Indeed, a more stringent disconnectivity requirement increases both the handoff rate and the energy consumption due to longer trajectories. Also, the impact study of different parameters provides the following guidelines: 1) Given a high tolerable disconnectivity rate, it is preferable to fly at the lowest permissible altitude in the most direct path to reduce energy consumption, 2) to operate partially or fully independently from the disconnectivity rate, it is encouraged to use a high-sensitive receiver at the cargo-UAV (which corresponds to

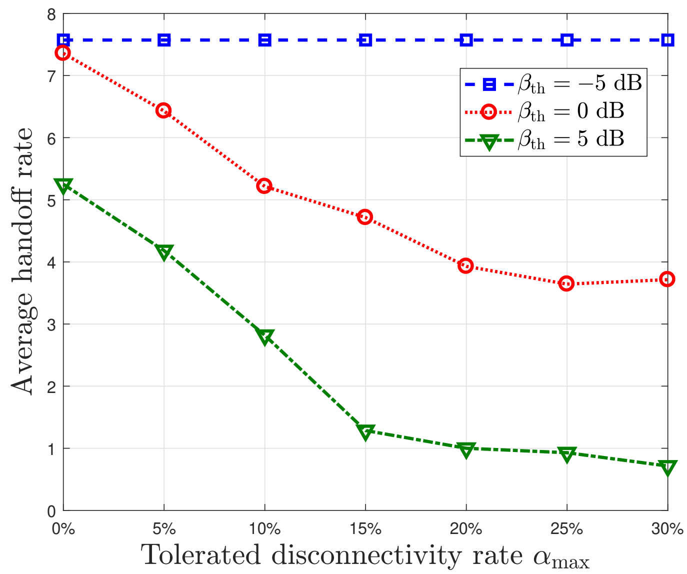

Fig. 6.6: Avg. handoff rate vs. $\alpha_{\max}$ (different β_{th}).

a low β_{th}), however a high handoff rate is expected, and 3) for energy-efficient operation, it is recommended to operate in low-density areas, e.g., RMa, or to redesign the frequency strategy in high-density areas, e.g., UMi, in order to reduce inter-cell interference. In the next Chapter, we investigate the cargo-UAV trajectory planning with a new cell association paradigm, where the cargo-UAV not necessarily associated with the terrestrial-BS with the strongest signal but rather the BS that ensures a reliable service and minimizes the future handoffs event along the trajectory.

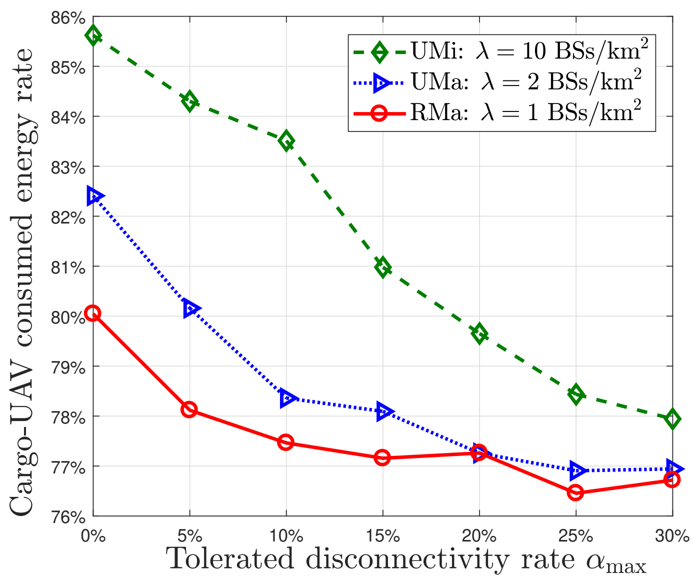

Fig. 6.7: Avg. consumed energy rate vs. $\alpha_{\max}$ ($h = 100$ m, different environments).

Algorithm 6.1 DP-based Trajectory Planning

Input: Matrix $\mathcal{H}$ of size $(M \times N)$ representing cellular connectivity heatmap (e.g., Fig. 6.1), step size γ, v, $\alpha_{\max}$, E_A, $\max_{\text{iter}}$, and START and END locations.

Output: Optimal trajectory $\mathcal{T}^*$.

Compute $d_{\max}$ using (6.13).
Initialize transition matrices T_ν, $\nu \in \{\text{dist}, \text{disc}, \text{ho}\}$ of size $(MN \times MN)$ with ∞.
Compute the cost (dist, disc, ho) from each cell in $\mathcal{H}$ to all other cells and store it in T_ν, $\nu \in \{\text{dist}, \text{disc}, \text{ho}\}$.
Initialize stage cost matrices ($S_{\text{dist}},\ S_{\text{disc}},$ and S_{ho}) of size $[1, M]$ with ∞.
Set the initial cost of the START cell to 0, i.e., $S_\nu(\text{START}) = 0$, $\nu \in \{\text{dist}, \text{disc}, \text{ho}\}$.
Generate the predecessor matrix P_{dist} of size $(M \times \max_{\text{iter}})$ for recursion. % $\max_{\text{iter}}$ is the maximal number of DP iterations
for $q = 2$ to $\max_{\text{iter}}$ **do**
  Store S_ν in predecessor matrix S_ν^{pr}, $\nu \in \{\text{dist}, \text{disc}, \text{ho}\}$.
  for $i = 1$ to M **do**
    for $j = 1$ to N **do**
      Compute the ν cost from cell j to cell i,
      i.e., $\nu_j = T_\nu(j, i) + S_\nu^{\text{pr}}(j)$, $\nu \in \{\text{dist}, \text{disc}, \text{ho}\}$.
      if the previous distance cost is higher than the
computed one, i.e., $\text{dist}_\text{j} \leqslant \text{S}_{\text{dist}}(\text{j})$ **then**
        if $\text{dist}_\text{j} \leqslant \text{d}_{\max}$ & $\frac{\text{disc}_j}{\text{dist}_j} \leqslant \alpha_{\max}$,
& $\text{ho}_j \leqslant S_{\text{ho}}(j)$ **then**
          Update S_ν $S_\nu(j) = \nu_j$, $\nu \in \{\text{dist}, \text{disc}, \text{ho}\}$.
          Store the optimal path from cell j to cell i
          in $P_{\text{dist}}(j, q) = i$.
        end if
      end if
    end for
  end for
  Break if the END cell is reached.
end for
Set the current cell to END cell.
Set st = size$(P_{\text{dist}}, 2)$, index ind=2, and cell = END.
while 1 **do**
  $\mathcal{T}^*(\text{ind} - 1) = \text{cell}$
  cell= $P_{\text{dist}}(\text{ind} - 1, \text{st} - \text{ind} + 1)$
  if cell = START **then**
    $\mathcal{T}^*(\text{ind}) = \text{START}$
    Break
  end if
  Set ind=ind+1.
end while
Return the optimal path stored in $\mathcal{T}^*$, representing the array of cells that the cargo-UAV should visit to reach the END cell.

Chapter 7

RL-Based Cargo-UAV Trajectory Planning and Cell Association for Minimum Handoffs, Disconnectivity, and Energy Consumption

7.1 Introduction

Due to their extreme flexibility and mobility, cargo unmanned aerial vehicles (cargo-UAVs) are gaining a significant share in the delivery market. For instance, Amazon Prime Air service is under development for BVLoS operations. In August 2021, Amazon got the approval of the FAA to operate its UAV fleet. With this milestone, cargo-UAV based delivery is expected to increase in the near future. Hence, cargo-UAV safety and security are paramount for the roll-out of aerial delivery and its public acceptance [3]. To this end, C&C is crucial for the safety of cargo-UAV BVLoS missions. Specifically, C&C data transmission can be supported by terrestrial cellular networks. However, re-utilizing

This work is under review at IEEE Transactions on Vehicular Technologies: **N. Cherif**, W. Jaafar, H. Yanikomeroglu, and A. Yongacoglu, "RL-Based Cargo-UAV Trajectory Planning and Cell Association for Minimum Handoffs, Disconnectivity, and Energy Consumption", under review at *IEEE TVT*.

existing cellular infrastructures for aerial operations brings challenges such as unreliable radio links due for instance to down-tilted antennas of terrestrial BSs) [17]. Besides, the mobility inheritance of cargo-UAVs may lead to frequent switching from one serving cell to another, a.k.a. handoff, hence, resulting in more signaling overhead that degrades the radio link's quality.

To guarantee cellular link reliability and reduce latency in terrestrial networks, authors of [93] proposed a deep learning-based handoff prediction strategy suited for millimiter wave (mmWave) communications. For cellular-connected UAVs, e.g., cargo-UAVs, several works focused on optimizing UAV trajectories for BVLoS operations. For instance, in [83], the authors set up a testbed for cellular-connected UAV missions. The performance of such a system was evaluated in [94] in terms of radio link failure and handoff rate. Moreover, the authors of [95] proposed an RL-based algorithm that balances between handoff rate and radio link quality for a pre-known UAV trajectory. Finally, we investigated for the first time in [96] cargo-UAV trajectory planning with consideration for energy consumption, communication link disconnectivity, and handoffs. Indeed, we proposed dynamic programming-based trajectory planning and studied the impact of several parameters, such as disconnectivity rate, handoff rate, and distribution of BSs in the mission area, on the cargo-UAV energy consumption.

To the best of our knowledge, only [96] investigated cargo-UAV trajectory planning from the perspective of energy consumption, cellular link reliability and handoff, altogether. However, the proposed method therein ignored the problem of cell association and assumed that the cargo-UAV is always associated to the cell with the strongest signal, which may cause frequent handoffs. Consequently, we propose in this work a novel RL-based algorithm for joint trajectory planning and cell association that aims to minimize energy consumption and number of handoff events, while guaranteeing a reliable communication link with the terrestrial network[1].

The remaining of the Chapter is organized as follows. Section II presents the system

[1]The reliability of a communication link can be evaluated in terms of cellular disconnectivity time during the cargo-UAV mission.

model. In Section III, we formulate the related problem. Section IV details the proposed RL-based trajectory planning and cell association algorithm for cargo-UAVs, while simulation results are discussed in Section V. Finally, Section VI concludes the Chapter.

7.2 System Model

We consider a 3D geographical area in the airspace of the city of Leuven, Belgium, centered at coordinates 50°52'45.3"N 4°42'08.1"E, based on a Cartesian coordinates system (x, y, z) [1]. We assume that a cargo-UAV is deployed to deliver an item from a retailer warehouse with coordinates $\mathbf{q}_w = (x_w, y_w, 0)$ to a preset drop-off location $\mathbf{q}_d = (x_d, y_d, 0)$ where the customer is expected to pick it up, e.g., at a community drop-off location or the private customer's porch [3]. The cargo-UAV is expected only to travel either vertically, i.e., at fixed (x, y), or horizontally, i.e., at fixed altitude $z = h$. To safely execute its mission, the cargo-UAV relies on cellular connectivity of the existing terrestrial network for C&C exchanges with a central unit on the ground.

7.2.1 Channel Model

The A2G communication channel model has been defined by 3GPP. It encompasses the BS's antenna gain, LoS probability, and path-loss expressions. For further details on the adopted A2G channel model and its components, we kindly refer the reader to [96, Section II-A].

7.2.2 Received Power Expression

Based on the channel model and assuming that the cargo-UAV is equipped with an omnidirectional antenna with unit gain, the average received power from the i^{th} cell, i.e., the Reference Signal Received Power (RSRP), is given by

$$P_{r,i} = P_T + G_i - L_i, \ \forall i = 1, \ldots, M, \tag{7.1}$$

where P_T is the transmit power of any ground cell in dBm. G_i is the array radiation pattern of the i^{th} cell given by [96, eq.(5)], and L_i is the average pathloss of the channel between the cargo-UAV and the i^{th} cell highlighted in [96, eq.(7)]. Finally, M is the total number of cells in the area. For the sake of simplicity, we assume that frequency planning is optimal, thus eliminating inter-cell interference at cargo-UAVs. Accordingly, the reliability of cellular connectivity depends on the level of RSRP at any potential location in the airspace. For illustrative purposes, we present in Fig. 7.1 the maximum RSRP level at each grid point of the (x, y) plane at different flying altitudes $h \in \{20, 40, 80, 120\}$ meters. At low altitudes, e.g., $h = 20$ meters, scattered coverage holes are more frequent than for $h = 40$ meters. This is due to the presence of more blockages such as buildings, trees, etc., in the Leuven urban area. In contrast, at high altitudes, the significant pathloss cancels-out the benefit of strong LoS radio links, thus leading to wider disconnectivity areas, as shown for instance at $h = 120$ meters.

Leveraging the data presented in Fig. 7.1, the cargo-UAV is considered disconnected when, at its actual location, no cell can guarantee an RSRP equal or higher than a pre-defined RSRP threshold, denoted T_{th}. Moreover, a handoff event occurs when the cargo-UAV is associated with a different cell than the previous one to which it was connected. During a cargo-UAV mission, it is crucial to rarely trigger handoff events, as the latter would destabilize the C&C link and generate an additional amount of overhead data.

7.2.3 Cargo-UAV Energy Consumption Model

The cargo-UAV energy consumption depends on its size, weight, and power, along its movement and communication regimes [91]. It consists of the propulsion energy and the communication energy. Typically, communication energy is very small compared to the propulsion energy, and thus, can be neglected. Using a rotary-wing cargo-UAV, the propulsion energy to fly for a distance d is

$$E(v, d) = P_{\text{prop}}(v)\ d/v,\ v > 0, \tag{7.2}$$

where $P_{\text{prop}}(v)$ is the propulsion power given by [96, eq.(10)] and v is the cargo-UAV velocity. Let E_C and E_S be the initial cargo-UAV energy capacity and emergency reserve

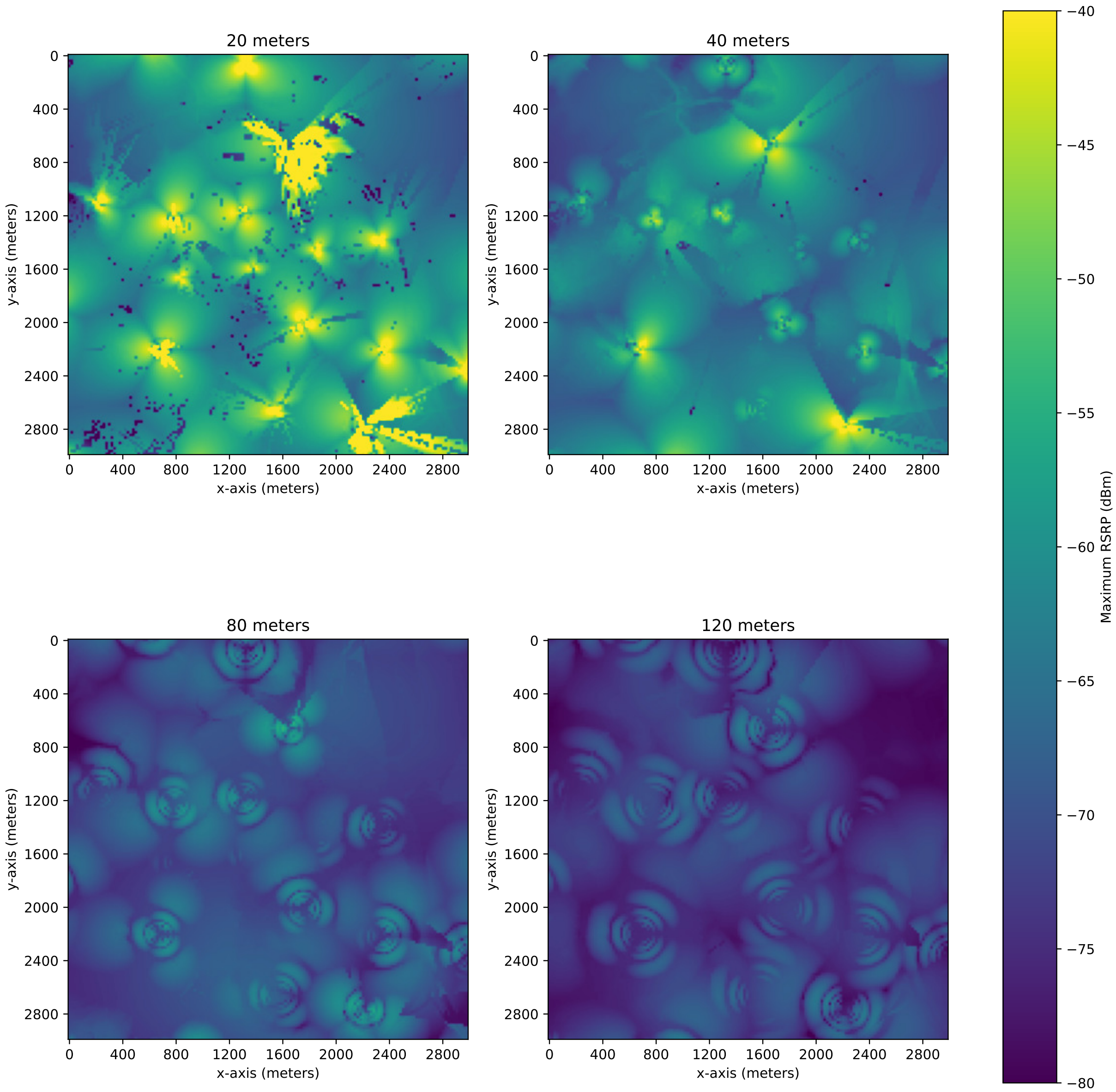

Fig. 7.1: Maximum RSRP heatmap of a part of the city of Leuven, Belgium, for different cargo-UAV altitudes (Area is 3×3 km^2 and $f_c = 1.8$ GHz [1]).

energy, respectively. E_C is available for the mission, while E_S is used for emergency pull-backs. Hence, the cargo-UAV's available energy to travel between the departure and arrival locations is

$$E_A(v,h) = E_C - E_S - 2E(v,h), \tag{7.3}$$

where $E(v,h)$ is the required energy to take-off from the dockstation or to land on the drop-off location.

7.3 Problem Formulation

The cargo-UAV is required to deliver a package from the retailer warehouse (at coordinates $\mathbf{q}_w$) to a consumer drop-off location (at coordinates $\mathbf{q}_d$). Our objective is to achieve this mission while consuming minimum energy, triggering minimum handoff events, while keeping a reliable communication.

Let $\mathcal{T} = \{\mathbf{q}_1, \ldots, \mathbf{q}_{|\mathcal{T}|}\}$ be the trajectory of the cargo-UAV, defined by the locations $\mathbf{q}_i = (x_i, y_i, h)$. Also, let $\mathcal{C} = \{c_1, \ldots, c_{|\mathcal{T}|}\}$ be the set of cell IDs associated to the cargo-UAV locations in $\mathcal{T}$, where $c_i \in \{1, \ldots, M\}$. It is noteworthy that at any grid location in the 2D plane at altitude h, the cargo-UAV receives RSRP measurement reports from all potential serving cells. Finally, we assume that the set of experienced RSRPs along the trajectory are represented by $\mathcal{R} = \{r_1, \ldots, r_{|\mathcal{T}|}\}$. Hence, the joint trajectory planning and cell association problem can be formulated as follows:

$$\begin{aligned} \mathrm{P1}: \min_{\mathcal{T},\mathcal{C}} \quad & w_{\mathrm{en}} \sum_{i=1}^{|\mathcal{T}|-1} E(v, d_{i,i+1}) + w_{\mathrm{sig}} \sum_{i=1}^{|\mathcal{T}|-1} \mathcal{D}(d_{i,i+1}) \\ + \quad & w_{\mathrm{ho}} \sum_{i=1}^{|\mathcal{T}|-1} \eta_{i,i+1} \end{aligned} \tag{P1}$$

$$\text{s.t.} \quad \sum_{i=1}^{|\mathcal{T}|-1} E(v, d_{i,i+1}) \leq E_A(v,h), \tag{P1.a}$$

$$\mathbf{q}_1 = \mathbf{q}_w, \text{ and } \mathbf{q}_{|\mathcal{T}|} = \mathbf{q}_d, \tag{P1.b}$$

where w_{x}, $\mathrm{x} \in \{\mathrm{en}, \ \mathrm{sig}, \ \mathrm{ho}\}$ are the weights balancing between energy consumption, radio link disconnectivity and handoffs, respectively, such that $w_{\mathrm{en}} + w_{\mathrm{sig}} + w_{\mathrm{ho}} = 1$.

We have $d_{i,i+1} = \|\mathbf{q}_i - \mathbf{q}_{i+1}\|$, and $\mathcal{D}(d_{i,i+1}) = d_{i,i+1}$ if $r_i < T_{\text{th}}$ and $r_{i+1} < T_{\text{th}}$; and $\mathcal{D}(d_{i,i+1}) = 0$ otherwise. $\mathcal{D}(d_{i,i+1})$ indicates a travelled distance in a coverage hole, i.e., without connectivity. Finally variable $\eta_{i,i+1}$ reflects the handoff event, i.e., $\eta_{i,i+1} = 1$ if $c_i \neq c_{i+1}$ and $\eta_{i,i+1} = 0$ otherwise.

Problem (P1) can be seen as a CVRP [92]. The CVRP is described as selecting the route for a vehicle with the objective of minimizing the total transport costs. Logically, the vehicle and transport costs can be assimilated in our system by the cargo-UAV and costs of energy consumption, disconnectivity, and handoffs, altogether. Since the CVRP is known to be an NP-hard problem [92], then by restriction (P1) is proved NP-hard.

7.4 Proposed RL-based Trajectory Planning and Cell Association

To solve the cargo-UAV constrained trajectory planning and cell association problem, we propose here an RL-based approach. First, we briefly overview the adopted RL method. Then, the framework for the proposed RL-based trajectory planning and cell association algorithm, including the definition of states, actions, and rewards are detailed.

7.4.1 RL Background

In RL, an agent, i.e., the cargo-UAV, interacts with its environment, i.e., the airspace. Specifically, it executes an action given its current state and the anticipated future reward. At an instant t, the agent in state s takes an action a. Based on (s, a), the agent receives a reward ρ. The process is iteratively repeated to maximize the expected reward over time and reach the end of the mission. The RL algorithm can be presented as a Markov decision process (MDP) defined by the $(\mathcal{S}, \mathcal{A}, \mathcal{P}_{sa}, \beta, \mathcal{W})$ where the set of states is encompassed in $\mathcal{S}$, $\mathcal{A}$ is the set of actions. Moreover, $\mathcal{P}_{sa}$ is the state transition probability of a state $s \in \mathcal{S}$ and an action $a \in \mathcal{A}$. $\beta \in [0, 1)$ is the discount factor. Finally, the reward function of a pair of state-action is $\mathcal{W}$. The optimal policy of the MDP aims to maximize the sum of discounted rewards by associating an optimal action to each state. We adopt here Q-learning to learn the optimal policy for the MDP.

The optimal policy adopted by the agent is the set of actions per state with the highest Q-values. The Q-value is given by the Bellman equation as

$$Q_{t+1}(s,a) = (1-\alpha)Q_t(s,a) + \alpha \left[\mathcal{W}_{t+1} + \beta \max_{a' \in \mathcal{A}} Q_t(s',a')\right], \tag{7.5}$$

where $Q_t(s,a)$ is the Q-value for (s,a) pair at episode (or time instant) t, α is the learning rate, $\mathcal{W}_{t+1}$ is the reward of episode $t+1$, and $Q_t(s',a')$ is the Q-value for state-action (s',a') in episode t.

7.4.2 Proposed RL-based Solution

We present here the proposed RL-based trajectory planning and cell association approach to solve problem (P1). The RL agent hosted by the cargo-UAV periodically collects its state. Then, it determines the best action, in terms of motion and cell association, and performs it. The state, action and reward of the RL agent are defined as follows:

Cargo-UAV's *state* is defined as $s = \{\mathbf{q}_s, c_s\}$ where $\mathbf{q}_s = (x_s, y_s, h)$ is the 3D location of the cargo-UAV in the airspace and $c_s \in \mathcal{C}$ is the corresponding serving cell ID. In state s, an action a is drawn from action space $\mathcal{A}$, which includes pairs of potential motion direction, i.e., east (E), west (W), north (N), south (S), north-east (NE), north-west (NW), south-east (SE), and south-west (SW), and cell IDs. The *reward function* is designed from the objective function of (P1), such that energy consumption, handoffs, and disconnectivity are minimized. Specifically, we express the reward function as

$$\mathcal{W}(s,a) = w_{\text{en}} W_{\text{mo}}(s,a) + w_{\text{sig}} W_{\text{sig}}(s,a) + w_{\text{ho}} W_{\text{ho}}(s,a), \tag{7.6}$$

where

$$W_{\text{mo}} = \begin{cases} -1/\sqrt{2} & \text{if motion direction} \in \{\text{N}, \text{S}, \text{E}, \text{W}\} \\ -1 & \text{otherwise,} \end{cases} \tag{7.7}$$

is the UAV motion (i.e., energy consumption) penalty,

$$W_{\text{ho}} = \begin{cases} 0 & \text{if } c_{s_t} = c_{s_{t+1}} \\ -10 & \text{otherwise,} \end{cases} \tag{7.8}$$

is the handoff cost, and the disconnectivity cost is given by

$$W_{\text{sig}}(s,a) = \begin{cases} 0 & \text{if } \text{RSRP}_{c_{s_{t+1}}} \geq T_{\text{th}} \\ -50 & \text{otherwise.} \end{cases} \tag{7.9}$$

The RL agent should be trained for a sufficient number of episodes to understand the environment dynamics and improve its decision-making, thus reaching the destination in the most efficient way. The proposed RL-based algorithm is presented in Algorithm 7.1. Specifically, the RL agent begins with no knowledge about the environment, i.e., an empty Q-table for all state-action combinations. The action space $\mathcal{A}$ encompasses all combinations of the motion directions and cell IDs at any given grid location of the 2D airspace plane. Then, the Q-table is built through the exploration/exploitation of the environment, making random/optimized actions, and calculating the corresponding reward. The latter is used to update the Q-value of the related state-action pair using (7.5).

These steps are repeated until the destination is reached within an episode. The execution of this algorithm for a sufficient number of episodes ensures convergence towards the optimal policy. The output of Algorithm 7.1 is the best strategy of trajectory and associated cells during the delivery mission.

7.5 Simulation Results

In this section, we assess the performance of the RL-based cargo-UAV trajectory planning with respect to cellular service reliability and handoffs. Hence, we compare our proposed algorithm to other benchmarks, i.e., shortest path and RSRP-aware path planning. The shortest path baseline is mainly calculated while being limited only by the capacity of the on-aboard battery. Hence, the cargo-UAV travels to its destination through the shortest path available while always connecting to the strongest cell along its way. In contrast, the RSRP-aware RL-based trajectory planning algorithm determines the path that increases cellular reliability, i.e., with the lowest cellular disconnectivity time while ignoring handoff events.

Algorithm 7.1 Proposed RL-based Solution

Input: Matrix $\mathbf{H}$ of size $(J \times J \times M')$ is the cellular connectivity heatmap at altitude h where J is the airspace grid length and width and $M' < M$ is the number of cells with the highest RSRPs; step size; cargo-UAV speed v; RSRP threshold T_{th}; Available energy E_A; starting location $\mathbf{q}_w$; arrival location $\mathbf{q}_d$.

Output: Optimal policy; Trajectory $\mathcal{T}$; Serving cells $\mathcal{C}$.

```
Initialize Q-table matrix Q with size (J × J × 8 × M') with 8 × M' is the size of the action space A.
while maximum number of episodes is not reached do
    Initialize T = {q_1} and C = {c_1}.
    while destination is not reached do
        Generate κ ∈ [0, 1]
        if κ < ϵ then
            Pick randomly an action from A.
        else
            Pick a* = argmax_{a∈A} Q(s, a).
        end if
        compute the reward W(s, a) using (7.6).
        Update the Q-value for (s, a) using (7.5).
        ϵ = max{ϵ_min, ϵ − ϵ_dec} with ϵ_min is the minimum allowed value for ϵ and ϵ_dec is the decay for each taken action.
    end while
end while
Return best (T*, C*).
```

We assume a 3×3 km^2 area in the city of Leuven, Belgium, where 20 three-sector BSs and 2 two-sector BSs are deployed. Each sector accounts for a cell, with a total number of 64. The area is divided into grid cells with a step of 20 meters on both X and Y axis. We set the following parameters as $v =$ 30 m/s and $E_C - E_S = 2500$ kJ. Finally, typical values of the cargo-UAV related parameters are taken from [75, Table I].

In any given 3D location (at a fixed altitude h), the received RSRP from each available cell in the area is measured and stored as part of the environment states space.

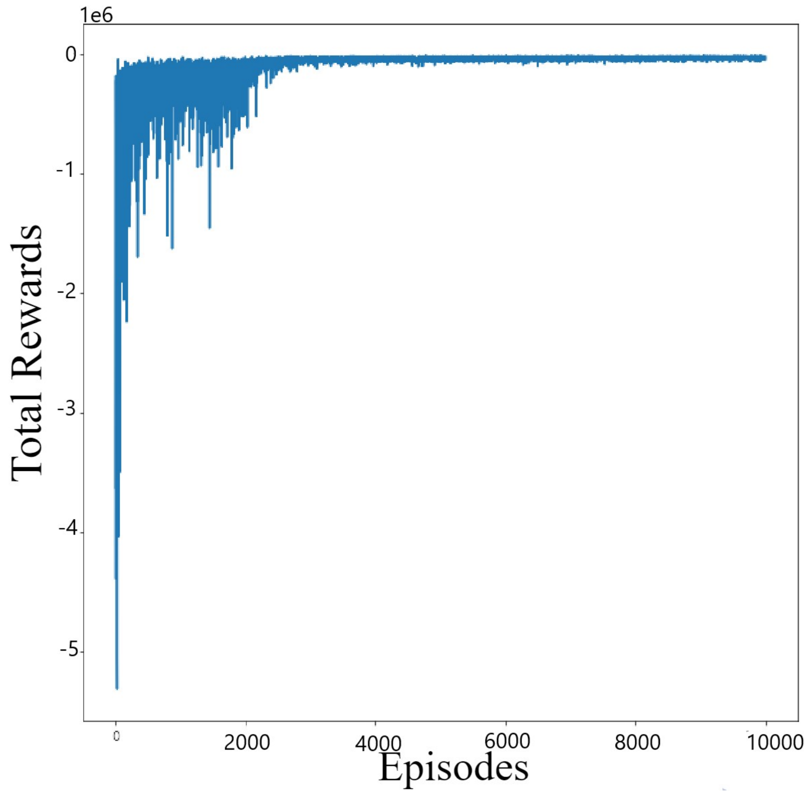

Fig. 7.2: Training convergence of proposed algorithm.

For the benchmark algorithms, only the cell with the strongest RSRP is considered to evaluate cellular disconnectivity and handoff performances, whereas our proposed algorithm considers in its states the first three strongest RSRPs, i.e., $N = 3$. Unless stated otherwise, the cellular service RSRP threshold is set to $T_{\text{th}} = -65$ dBm, $w_{\text{en}} = 0.5$, $w_{\text{sig}} = 0.35$, and $w_{\text{ho}} = 0.15$. For the RL parameters, we set $\beta = 0.9$, $\alpha = 0.01$, $\epsilon_{\text{min}} = 0.01$, and $\epsilon = 0.99$. The total number of training episodes is fixed to 10^4.

We show in Fig. 7.2 the learning curve of the proposed RL-based path planning algorithm. First, the cargo-UAV starts exploring the airspace without any prior knowledge and by randomizing its action, and accordingly constructs its Q-table by associating each realized action to a prospect reward. As the number of training episodes increases, the exploration phase is given less importance and the cargo-UAV starts to exploit the acquired experience to advance towards its destination. This translates into a proportional reward increase with training. As it can be seen, our algorithm converges from episode 3500, and the reward is maximized close to the maximum value 0.

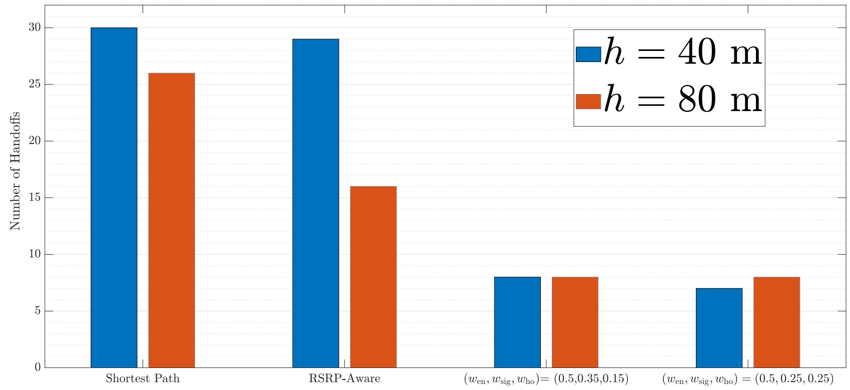

(a) Number of handoffs.

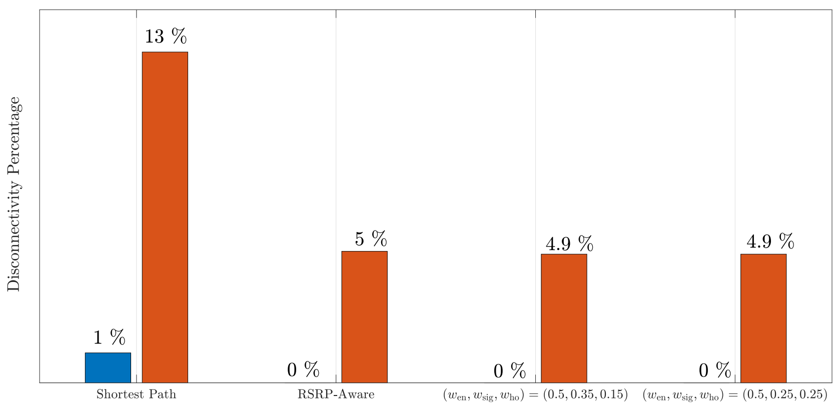

(b) Disconnectivity along cargo-UAV mission (%).

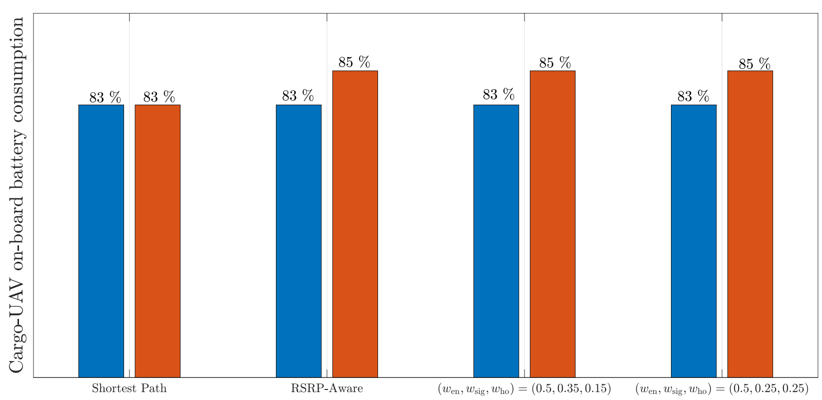

(c) Battery consumption (%).

Fig. 7.3: Comparison of path planning algorithms (different altitudes).

Fig. 7.3 compares the performance of the proposed algorithm against those of benchmarks, i.e., "Shortest Path" and "RSRP-Aware" [96] algorithms, in terms of number of

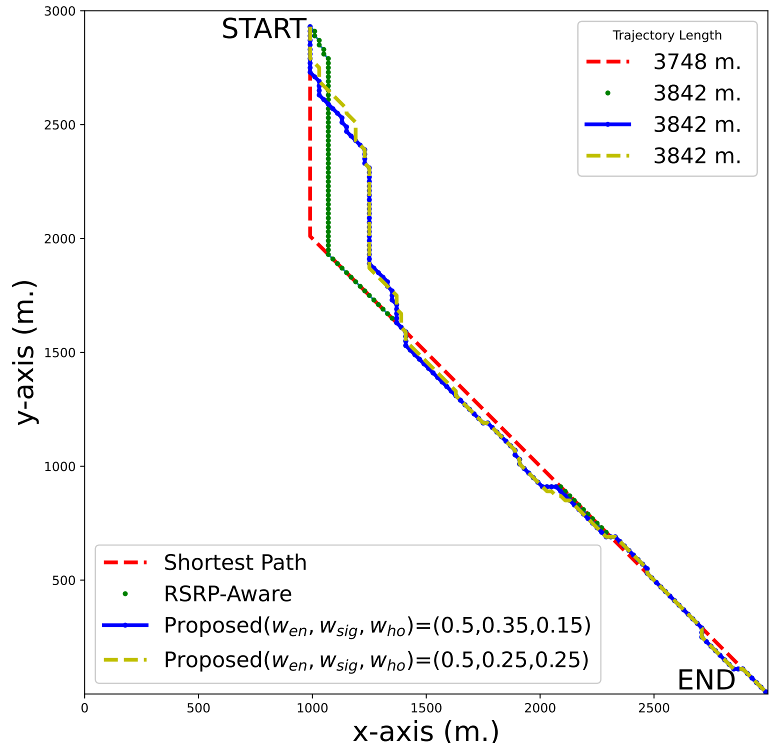

Fig. 7.4: Cargo-UAV trajectories ($h = 80$ m).

handoffs, battery consumption percentage, and disconnectivity percentage along the mission's trajectory. For the proposed algorithm, we considered two configurations, the first with $(w_{\text{en}}, w_{\text{sig}}, w_{\text{ho}}) = (0.5, 0.35, 0.15)$ and the second with $(w_{\text{en}}, w_{\text{sig}}, w_{\text{ho}}) = (0.5, 0.25, 0.25)$. According to Figs. 7.3.a-7.3.b, the shortest path algorithm experiences the highest number of handoffs and disconnectivity percentage for any flying altitude h. This is expected since the shortest path aim to reach the destination in the fastest possible way, regardless of other factors. As a consequence, it consumes the least energy as shown in Fig. 7.3.c. For RSRP-Aware algorithm, the number of handoffs and disconnectivity percentage are lower than for the previous method, since the cargo-UAV adjusts its trajectory to keep RSRP above the sensitivity threshold, whenever possible. However, this translates into a slightly higher energy consumption (about 1.8%), due to the additional flying maneuvers, especially at higher altitudes where RSRP signals are weaker. For the proposed algorithm, the number of handoffs and disconnectivity percentage are the lowest, while the consumed energy is approximately the same as the shortest path at $h = 40$ m and as the RSRP-Aware one at $h = 80$ m. Indeed, the consumed energy of the additional detours to avoid triggering

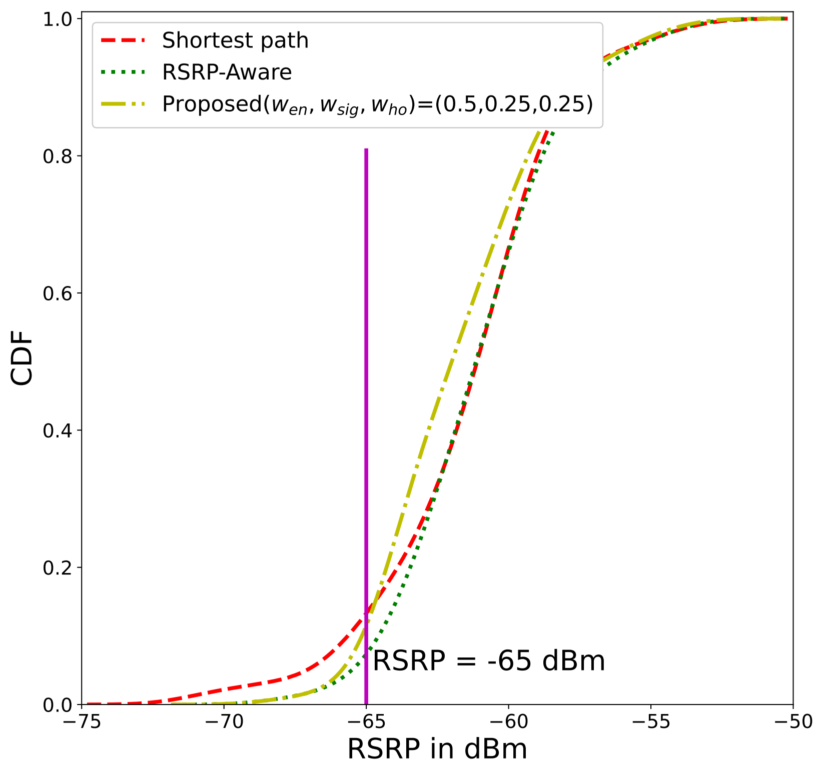

Fig. 7.5: Comparison of RSRP's CDFs.

handoffs compensates for the energy required by the handoff signalling mechanism, while ensuring a minimal number of handoffs and disconnectivity percentage. Also, when the handoffs weight w_{ho} is increased in the reward function from 0.15 to 0.25, the number of handoffs can be further reduced, in particular at lower altitudes.

In Fig. 7.4, we present the resulting trajectories of the Fig. 7.3's algorithms. Although the trajectories of our proposed approach (yellow and blue lines) experience several detours, it still achieves the mission with the best performances in terms of number of handoffs and disconnectivity, at the cost of a slight increase in energy consumption.

We illustrate in Fig. 7.5 the cumulative distribution function (CDF) of RSRP for the trajectory planning algorithms, and under the same aforementioned assumptions. Clearly, our proposed method achieves the best CDF performance for RSRP$<T_{\text{th}}$, however it degrades for higher RSRP. This is expected since our method trades off a lower link quality (close to T_{th} and no disconnectivity), for a smaller number of handoff events, thus reducing signalling overhead and energy consumption, compared to other methods.

7.6 Conclusion

In this Chapter, we proposed a novel energy-efficient disconnectivity and handoff aware RL-based trajectory planning and cell association algorithm for cargo-UAVs. Through simulations, we prove the superiority of our approach in terms of number of handoffs and disconnectivity, at the expense of a slight increase in battery consumption, when compared to baseline algorithms. Overall, this Chapter aims at using machine learning tools for energy-efficient trajectory planning with emphasis in minimizing the handoff rate and maximizing the cellular reliability of the cargo-UAV.

Chapter 8

iTUAVs: Intermittently tethered UAVs for future wireless networks

8.1 Introduction

Throughout this thesis, we have been focused on cellular-connected UAV. Nevertheless, UAV-BS have captured huge interest in the research community and industry. In this Chapter we present a new paradigm for UAV-BS to provide cellular coverage for terrestrial users, though, all drawn conclusion can still be applicable for aerial users, i.e., cellular-connected UAV. To start, we answer this important question, what are the advantages of UAV-mounted wireless communications? It increases the chances of a stable Line-of-Sight (LoS) dominated channel to ground terminals [13]. UAVs can also move and optimize their locations to satisfy the dynamic service demand [97,98]. These two features represent the core of all innovative wireless communication solutions enabled by Unmanned Aerial Vehicles (UAVs), including UAV base stations (UAV-BSs), also called UxNB by 3GPP.

The limited battery capacity is the main challenge to fully unleash the UAV-BS po-

This work has been accepted for publication at IEEE Wireless Communications Magazine in Sep. 8 th 2022: **N. Cherif**, W. Jaafar, E. Vinogradov, H. Yanikomeroglu, S.Pollin and A. Yongacoglu, "iTUAVs: Intermittently tethered UAVs for future wireless networks", accepted for publication in *IEEE Wireless Communications Magazine*.

tential. To overcome this issue, several solutions have been proposed such as i) deploying recharging stations, ii) battery or UAV swapping, and iii) laser charging. Moreover, providing UAVs with permanent energy supply through a tether, a.k.a., tethered UAV (TUAVs), has been proposed as an alternative to the aforementioned solutions. Nevertheless, this concept offers unlimited flight time at the expense of limited mobility due to its predetermined hovering region [99].

Consequently, we propose here a novel development to the operation mode of the TUAV system, which would make it more flexible and thus more attractive to industry. It consists on the introduction of an agile tether that can be attached/detached to/from existing infrastructures, called ground anchors, such as UAV and electric vehicle charging stations, illustrated in Fig. 8.1. We call this novel system intermittently tethered UAV (iTUAV). It is noteworthy that “ground anchor” and “anchor” are used interchangeably throughout the chapter.

The rest of the chapter is organized as follows. We discuss state-of-the-art works aiming to overcome UAV-BS battery limitation. Then, we describe the iTUAV system components, operational mode, and provide a qualitative comparison to existing technologies. The potential of the iTUAV is presented next through a case study. Finally, we highlight a number of future research opportunities and conclude the chapter.

8.2 UAV-based Communications: A Review

In recent years, the use of UAVs to provide cellular connectivity has attracted increasing attention and their potential for complementing terrestrial networks has been investigated extensively in the literature. Due to their agility and flexibility, UAV-BSs can handle temporary spikes in data demands during short-term events, such as large concerts and sporting events [36]. However, UAV-BS operations are hampered by limited flying times, typically ranging from 30 minutes to a few hours. To tackle this problem, numerous solutions have been investigated, including battery recharging and swapping, UAV swapping, laser charging, and TUAV systems. We provide an overview of the pros and cons of these

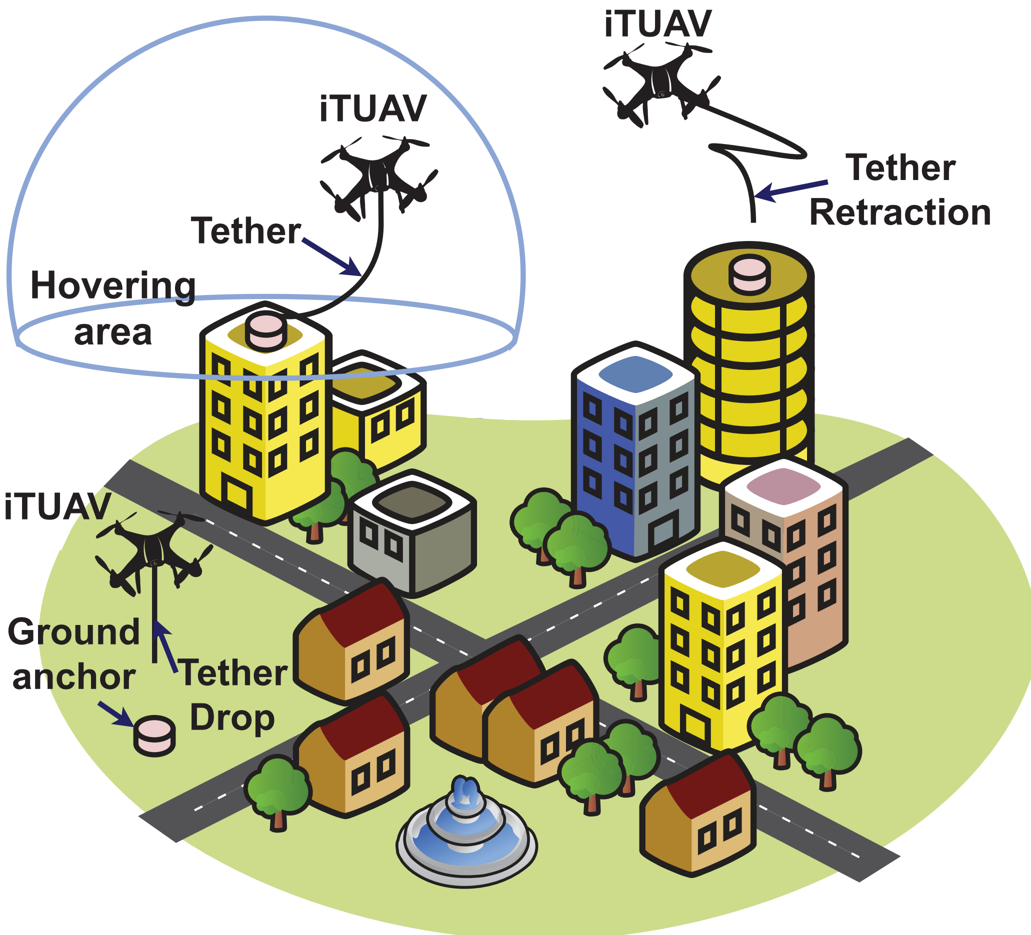

Fig. 8.1: Proposed iTUAV system.

solutions in Table 8.1 and describe them in the following subsections.

8.2.1 Battery Recharging and Swapping

To overcome the battery capacity limitation, one can design a system where a UAV-BS flies back to a dedicated charging station to either recharge its battery or exchange it for a filled one. In [100], the authors studied the coverage performance of a UAV-assisted cellular network supported by charging stations. They derived the coverage probability as a function of the battery size, density of charging stations, and charging time. In the analysis, they identified a tradeoff between the deployment density of charging stations

Table 8.1: Comparison of UAV-based cellular systems.

UAV-based solution	Pros	Cons
Battery swapping and recharging	• Operating a small UAV fleet compared to other systems	• Frequent service interruptions • Cost of charging stations deployment • Long battery charging time
UAV swapping	• Ubiquitous cellular coverage • Flexible cellular service	• High CAPEX/OPEX for large UAV fleets
Laser charging	• Practical and cost-effective DLC for small UAVs • Battery charging during missions • No service interruptions	• Restricted laser beaming in high dense areas • Mandatory LoS for efficient DLC charging • Long battery charging time
TUAV system	• Unlimited mission time • Good cellular coverage • Reliable backhaul link	• Limited hovering region • Static/manual deployment and redeployment

and their quality (i.e., charging time).

Critique: Since UAV-BSs have to spend time to travel and recharge at a dockstation or land for battery swapping, these solutions cause frequent service interruptions, which is not ideal for stringent connectivity services, such as safety applications.

8.2.2 UAV-BSs Swapping

In order to eliminate service interruptions, several works have proposed continuous UAV-BS swapping. In [100], the authors discussed the swapping strategy that continuously sustains a predefined mission. Similarly, the authors of [101] proposed automating UAV swapping for continuous cellular connectivity by monitoring UAV-BSs battery levels.

Critique: These approaches offer high UAV-BS deployment flexibility and sustained cellular services. However, their advantages come at the expense of higher capital and operational expenditures (CAPEX/OPEX), due to a larger UAV fleet.

8.2.3 Laser Charging

Another solution consists of recharging UAV-BSs on-the-fly through laser beaming. This technology can be implemented with a laser array oriented through a set of mirrors or diamonds aimed at the UAV-BS's collecting lens. In spite of its great potential, laser beaming requires large collecting lenses and high laser power, two factors that limit its deployment, especially in urban areas. Alternatively, distributed laser charging (DLC) involves the use of photo-voltaic cells instead of a collecting lens, which is practical and cost-effective for small UAV-BSs [91]. Unlike laser beaming, DLC uses less than one kilowatt transmit power, thus favoring its deployment anywhere. Finally, efficient DLC requires LoS between the charging source and UAV-BS.

Critique: Due to health-related concerns, laser beaming with high power cannot be used in densely populated areas. In the meanwhile, DLC may perform poorly in non-LoS conditions. Moreover, due to its slow charging regime, DLC is only efficient when the UAV-BS is on stand-by [91].

8.2.4 TUAV Systems

TUAV does not suffer from short operation time. Its main idea involves linking the UAV to the ground using a tether that provides both power supply and high-capacity backhaul. Consequently, the limited TUAV mobility is compensated by a longer operation time and higher backhauling capacity. In [99], the authors described a TUAV-aided cellular network and evaluated its coverage probability. This research was extended in [102] to optimize the TUAV joint-placement and user-association for maximized coverage probability.

These works introduced specific constraints to TUAVs such as limited tether length and safety considerations to avoid tangling the tether around surrounding buildings. Also, they assumed that the tether serves both as power cable and wired backhaul link. This assumption implies complex and high cost tether and anchor designs, since additional data equipment deployment/configuration are required. Alternatively, a simpler tether design can be used for power supply only, while relying on wireless backhauling through either radio or free-space optical communications [103].

Critique: The main disadvantage of TUAVs is the reduced flexibility due to the highly restricted flying distance. Moreover, backhauling through a tether implies higher equipment cost. Thus, TUAVs may be considered a good alternative to terrestrial BSs (TBSs) and by far do not offer the large advantages of UAV-BSs.

8.3 Intermittently Tethered UAVs

Given the limited hovering areas of TUAVs and battery-limited operation of untethered UAVs, we propose here a compromise solution, called iTUAV, which offers both the flexibility of a UAV and the sustainable operation of a TUAV. In what follows, we present the iTUAV system components, operation mode, and a qualitative features comparison to existing technologies.

8.3.1 System Components

An iTUAV-aided communication system involves several components shown in Fig. 8.1 and described as follows:

iTUAV An iTUAV is a small UAV equipped with a lightweight 5G New Radio (NR) UxNB for communication, e.g., Ericsson's network-on-a-drone. Specifically, the iTUAV has the following modules:

- **Access:** As specified in 3GPP TR 22.829, UxNB is able to connect to the 5G core network and operate as a BS, via a wireless backhaul link, and can bootstrap as a BS, from the core network's perspective. The user experiences no difference between being served by a UxNB or by a TBS. To do so, we assume that the UxNB is equipped with multiple antennas enabling directional patterns towards users [104].
- **Backhaul:** The backhaul can be provided by a wireless gateway (e.g., a nearby TBS, TUAV, or satellite) or through an associated anchor, if it provides backhauling services. In the case of a wireless backhaul, integrated access and backhaul (IAB) can be leveraged [103, 104]. Since 3GPP does not enforce any particular IAB implementation, radio access and backhauling can use different frequency bands (e.g., dual-band IAB: millimeter wave for backhaul and sub-6 GHz for access) or the same spectrum. The latter is possible since a UxNB supports directional antenna arrays to spatially separate the links. Although this technology is cost-effective and lowers

the iTUAV's payload, it provides a lower system capacity and requires more complex resource management than the dual-band IAB.

- **Power:** To reduce costs, we assume that the iTUAV is equipped with a *small battery* that enables short flight times to reach anchors and reconnect through a tether. Moreover, each iTUAV is equipped with a *socket* that allows it to attach a retractable tether from the anchor and that can be used simultaneously to power the motors in-flight and to recharge the battery. This design suggests landing over the anchor to attach the iTUAV, thus causing service delays. Alternatively, the iTUAV can be equipped with a *lightweight tether* that is dropped vertically to the anchor rather than landing on it [105].

Ground anchors These are mainly power supply sources used to sustain iTUAV operations. A ground anchor may include one or several of the following components. First, it must have access to the power grid and be equipped with adequate *power converters* to support different types and sizes of UAVs and electric vehicles. Second, it may be provided with *standardized sockets* to plug UAVs and electric vehicles. Third, it may include *power tethers* dedicated for iTUAVs with power sockets. Fourth, it may have a *battery swapping station*, which may be used by UAV-BSs. Additionally, the anchor can offer backhauling through a *wired link* combined with *on-site routing equipment*. The versatility of the anchor role favors its business and practical interests as part of the smart city infrastructure. For instance, anchors can be easily and seamlessly integrated to lampposts, road signs, and lights.

Gateway This is the entry-point of the iTUAV to the core network. It can be the routing equipment of an anchor, a TBS, a TUAV, or a satellite. Except for the anchor that allows a direct wired connection to the core network, the other alternatives require wireless links with the iTUAV. Although wireless transmissions are less efficient than wired ones, communicating with a TBS equipped with *highly directional antenna arrays* using IAB is an effective and cheap alternative.

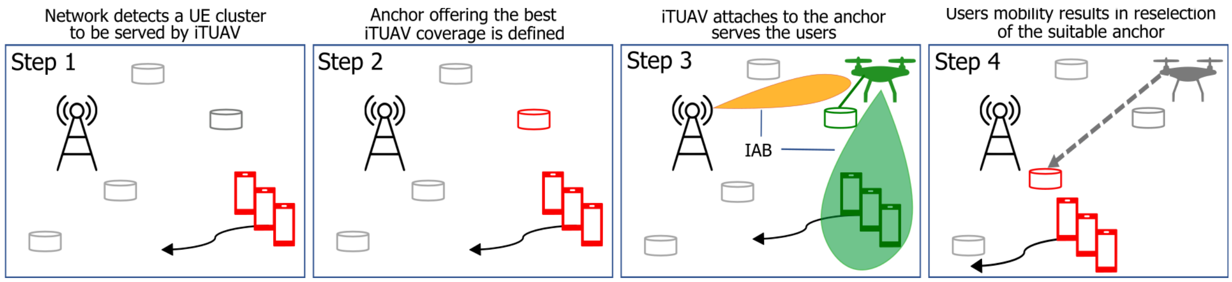

Fig. 8.2: Steps in the operation of the iTUAV system (the solid black arrows show the users' motion direction; the gray dashed arrow represents the ground anchor selection; the green solid line is the tether that connects the iTUAV to the anchor; the green and orange beams are the access and backhaul links, respectively.

8.3.2 System Operation

We assume a communication system deployed in an urban environment, e.g., smart city, consisting of iTUAVs, TBSs, ground anchors, and mobile ground users. The main goal of an iTUAV-aided communication network is to meet the performance requirements related to ubiquitous coverage, e.g., during temporary events, and to on-demand network densification due, for instance, to peak traffic demands. Fig. 8.2 details the operational steps of this system, explained below:

1. A TBS detects users that cannot be reliably served. These users are localized and clustered, then assigned to an iTUAV.
2. To serve the cluster of users, the optimal location of the iTUAV and its associated anchor are jointly determined. The formulation and solution of this problem may take into account practical limitations, such as the propagation environment, backhaul link quality, TBS radio resources, etc.
3. The iTUAV flies to the anchor and connects to it through a retractable power tether. Next, it travels to its optimal location and hovers to serve the associated cluster of users.

4. Since users are mobile, the optimal location of the iTUAV (determined in the previous steps) may become out of reach of the tether's length. In this case, the new optimal location and associated anchor must be recalculated. Subsequently, the iTUAV detaches itself from the current anchor and re-executes step 3.

8.3.3 iTUAV Systems Versus Existing Technologies

The idea behind iTUAV emerges from the tradeoff between mobility and power availability. In what follows, we compare the UAV-based cellular networks, namely iTUAV, UAV (i.e., untethered UAV-BS), TUAV, and TBS, from different perspectives.

- **Mobility:** UAVs equipped with BSs gained popularity thanks to their exceptional 3D mobility. A typical UAV-BS use-case consists of providing connectivity for temporary events with high traffic demands. Such scenarios cannot be handled by terrestrial cellular networks due to the fixed nature of TBSs. In contrast, TUAVs and iTUAVs are much less constrained, and thus can leverage their partially limited mobility to better serve users. Nevertheless, a TUAV is permanently fixed to an anchor, which limits its region of activity, compared to an iTUAV, which is able to travel from one anchor to another. Consequently, iTUAVs cover wider areas than TUAVs.

- **Re-deployment Flexibility:** UAVs are valued for their rapid deployment feature, due to their high flying speed. An iTUAV can be re-deployed almost as quickly, either by relocating within a hovering region, subject to the tether length, or by traveling to the closest anchor to the targeted location. Note that the inherent relocation flexibility of a TUAV is strongly linked to the length of the tether and thus to its hovering region. That means, if redeployment is required in an area outside the hovering region, the TUAV cannot satisfy the new requirement. Finally, TBSs lack this feature due to their fixed nature.

- **Cellular Reliability:** A terrestrial network is considered reliable when its TBSs deployment is optimized and does not experience substantial coverage gaps. An aerial BS increases the probability of LoS to communicate with ground users and thus is capable of providing a similar performance as a TBS. However, untethered UAV-BSs rely on wireless backhauling, which is limited compared to a TBS wired backhaul. A TUAV system offers better reliability due to its wired backhaul; nevertheless, its limited motion prevents it from offering a highly reliable coverage. Finally, an iTUAV ensures a better cellular reliability than UAV/TUAV systems due to its flexibility in connecting with different anchors to achieve better access/backhaul links. With enough available anchors, iTUAVs can achieve similar performance to TBSs.

- **Backhaul Availability:** A terrestrial network provides a highly available backhaul through fiber links and point-to-point RF transmissions. Similarly, TUAV-based solutions assume that backhauling is carried through fiber links aggregated with the power supply within the tether. By contrast, iTUAVs are expected to operate opportunistically with both wireless and wired backhauling. Indeed, whenever the anchor provides a tether with a fiber optic data link, backhauling goes through it. However, if an anchor is exclusively a power source or when an iTUAV is traveling between anchors, then it has to rely on wireless links to most adequate TBSs, i.e., with enough capacity to handle the iTUAV's traffic, or to other wireless gateways. Wireless backhauling is significantly affected by the environment conditions, such as closeness of wireless gateways, obstacles, shadowing, etc. Finally, untethered UAV-BSs rely solely on the wireless backhaul.

- **Energy Availability:** Clearly, the untethered UAV-BS has the lowest power capacity. By contrast, energy for TBSs and TUAVs is available continuously. iTUAVs, although occasionally traveling, enjoy a very high energy availability. When an iTUAV is attached to an anchor, it has unlimited access to power as TUAVs. This energy is used for both iTUAV operation and battery recharging. However, when it is traveling between anchors, it relies exclusively on its on-board battery. Note that locations of anchors and battery capacity must be carefully and jointly designed in order to avoid draining the iTUAV's battery when traveling between anchors.

- **Infrastructure Reuse:** Terrestrial cellular infrastructure suffers from a low usage rate due to users with sporadic traffic demands. In TUAV systems, the anchor is permanently powering a single or several TUAVs through tether(s), resulting in small or no opportunities to reuse the tether or the power supply of the anchor. By contrast, an iTUAV is only attached to an anchor for the time of its mission, then it releases the tether and flies to a different location. The low usage rate of anchors by iTUAVs favors their reuse for other applications such as recharging flying taxis, cargo UAVs, and electric vehicles. Moreover, the fleet of iTUAVs is much smaller than the one considered by UAV swapping. Infrastructure reuse substantially increases iTUAVs' economic viability. Moreover, the additional generated revenue from anchors reuse can offset the investment of extensive anchor networks and the expenses thereafter (e.g., rental of rooftops).

- **CAPEX:** One of the main concerns in setting up cellular services is the amount of initial investment needed. TBSs are usually costly. Locations for their deployment need to be purchased or leased, and they require expensive electrical and communications equipment. In contrast, UAVs are less expensive, but have limitations that need to be considered. This typically leads to purchasing a high number of UAVs, batteries, and recharging stations to enable UAV swapping, battery recharging/swapping. In the case of TUAVs, the initial investment consists of buying UAVs with their tether anchors for power supply and communication. Due to the limited tether length, covering a large area would require the deployment of several TUAVs, which may rapidly increase costs. Like TUAVs, iTUAVs rely on anchors, but with lighter functionalities. Indeed, Compared to TUAV systems, a smaller number of iTUAVs but a slightly higher number of anchors may be needed to sustain wireless services in large areas. In addition, iTUAV anchors might provide only power, thus alleviating any complexity in setting wired backhauling.

- **OPEX:** Terrestrial networks still face high operating costs for equipment maintenance. The use of UAVs instead requires sophisticated software and professional UAV pilots to lead missions and organize recharging/swapping operations. For TUAV and iTUAV systems, in addition to operation software, maintenance of UAVs and anchors is needed. However, the cost of maintaining a UAV is expected to be higher than that for an anchor. Hence, OPEX might be slightly lower for iTUAVs due to their forecast smaller number, but slightly higher number of anchors. Finally, iTUAV anchors can generate additional revenue through their reuse, which is expected to significantly offset the CAPEX/OPEX costs.

Based on the foregoing discussion, iTUAV systems present great potential to compete with or complement existing cellular technologies. They represent a promising middle-solution between the mobility features of UAVs and the operational sustainability of TUAVs and TBSs.

8.4 Case Study

To corroborate our findings on iTUAV systems, we investigate here their achievable performance in terms of average number of covered users as a function of terrestrial users density and of its sustainability. These results are compared against those of UAV and TUAV systems.

8.4.1 Simulation setup

We consider a 3×3 km^2 urban area where a single UAV (or a TUAV or an iTUAV) is deployed to provide cellular coverage for terrestrial users equipment (UEs). The transmit power is set to $P_t = 30$ dBm and the UE receiver sensitivity is $P_{\min} = -70$ dBm [13], which translates to a path loss threshold of 100 dB. We assume that the air-to-ground channels follow the probabilistic line-of-sight LoS and NLoS propagation model [46], operating at frequency $f_c = 2$ GHz. The average height of anchors is 50 m and the maximal tether length for both the TUAV and iTUAV is set to 150 m [102]. For the sake of simplicity, we assume that the TUAV (resp. iTUAV) minimum inclination angle that prevents tangling around surrounding buildings and ensures the safety of the tether is set to 0°. The UEs are distributed according to the Thomas point process. With this distribution, clustering of UEs is modeled through the coefficient of variation (CoV) of the Voronoi cell area around each user [106]. For instance, when CoV = 1, the UEs are uniformly distributed according to the Poisson point process, whereas a higher CoV represents more clustered users around a virtual cluster head [107, 108]. At each realization, i.e., UEs and anchors geographical distributions, the iTUAV determines the optimal anchor and attaches to it to provide cellular coverage to the highest number of UEs. In contrast, the untethered UAV freely determines and reaches the optimal 3D location that maximizes its coverage [13], whereas the TUAV, constrained to its pseudo-static deployment, relocates withing its hovering region to cover the maximal number of UEs [102]. Finally, simulation results are averaged over both the UEs' geographical distribution and anchor positions in each iteration.

Given the identified constraints of iTUAV (resp. UAV and TUAV) system, the formulated problems aim to maximize the cellular coverage of iTUAVs (resp. UAVs and TUAVs) through the optimization of the UAV-BS 3D location and ground anchor association (iTUAV). Although seeming different, these problems are convex [13,45]. Hence, they can be solved using MOSEK parser in the CVX package of Matlab.

8.4.2 Results and Discussion

Fig. 8.3 shows the average number of users covered by the single serving UAV as a function of the CoV for different UAV systems, namely, UAV, TUAV, and iTUAV. Although TUAV and iTUAV deploy a single UAV, the UAV system assumes UAV swapping in order to ensure a similar service continuity over time [101]. As expected, the UAV presents the best coverage performance thanks to its optimal placement. By contrast, the TUAV is extremely limited in its flying range by the tether/anchor location, thus often missing the best placement achieved by the UAV. Alternatively, the iTUAV outperforms the TUAV due to the availability of several anchors, which allows it to select the best one and optimally place itself to cover a higher number of users. Nevertheless, the iTUAV system performs below the UAV, since it may miss the optimal placement if none of the anchors is located close enough (subject to the tether's length) to the UAV optimal location. With a higher number of anchors, the iTUAV can exploit more optimized hovering locations, and thus achieves better coverage performance. Finally, as the CoV increases, coverage improves

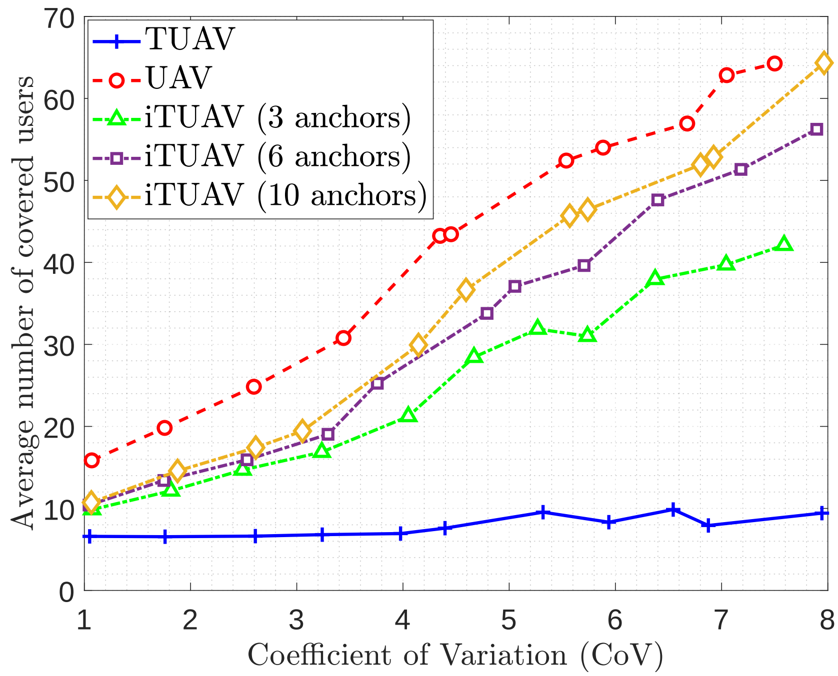

Fig. 8.3: Coverage performance of UAV (with swapping), TUAV, and iTUAV systems, for different user distributions.

for all systems. Since users are more clustered, the UAV can communicate through better channels to a higher number of users.

Fig. 8.4 compares the performances of the UAV without swapping (w/o swap), UAV with swapping (w/ swap), TUAV, and iTUAV systems in terms of the average number of covered users per time unit (min.). Specifically, we define a cellular radio access mission consisting of deploying one UAV within a target area to provide cellular connectivity during a temporary event of 100 minutes.[1] During this event, we aim to maximize the average number of connected users to the mobile UAV. The average is calculated over multiple network topologies (i.e., different scenarios for users' and anchors' locations) and time. We assume different battery capacities for the UAV (w/o swap), ranging between 30 and 60 minutes of flying time, while the iTUAV relies on a number of anchors, between 3 and 10. We notice that the UAV (w/o swap) coverage performance is low with a small battery capacity (e.g., 8 users per min. with a battery of 30 min.), but it improves with a larger

[1]This assumption implies no UAV swapping for the untethered UAV and the mission of the UAV is hence limited by the battery lifetime.

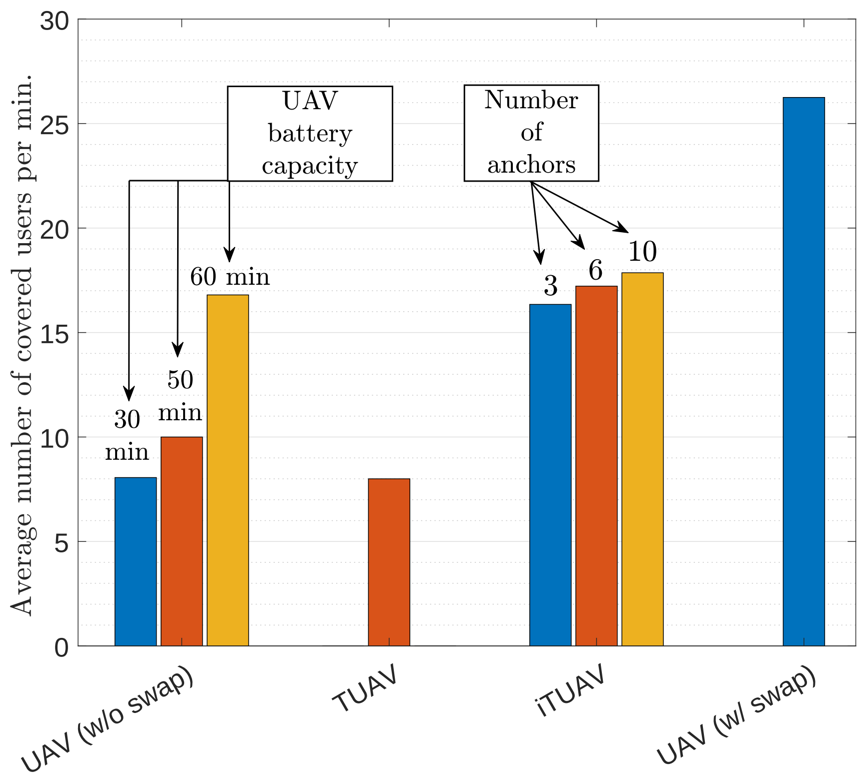

Fig. 8.4: Coverage performance of UAV, TUAV, and iTUAV systems for a temporary event of 100 minutes (CoV = 3).

battery capacity (e.g., 16.8 users per min. with a battery of 60 min.). However, the TUAV can continuously serve 8 users per minute. The TUAV performance is mainly limited by the tether that prevents the UAV from hovering at a better location where it could serve more users. With more anchors, the iTUAV enjoys better performance over time as it can also serve more users owing to its mobility and stable power source, i.e., through the tether and the on-board battery when traveling between anchors. Finally, considering UAV (w/ swap), this system is equivalent to having an unlimited battery capacity while enjoying full motion flexibility, thus it achieves the best performance, i.e., around 26 users in average are covered through time. This performance, however, comes at the expense of an additional investment in a higher number of UAVs and more complex operations. In a nutshell, we conclude that, thanks to its unlimited power and flexible association to anchors, the iTUAV is able to sustain a reliable cellular service over time, which is better than the UAV (w/o swap) and TUAV systems, but slightly below that of the UAV (w/

swap) reference system. If a higher number and more adequate locations of anchors are available, iTUAV performance is expected to reach that of the UAV (w/ swap).

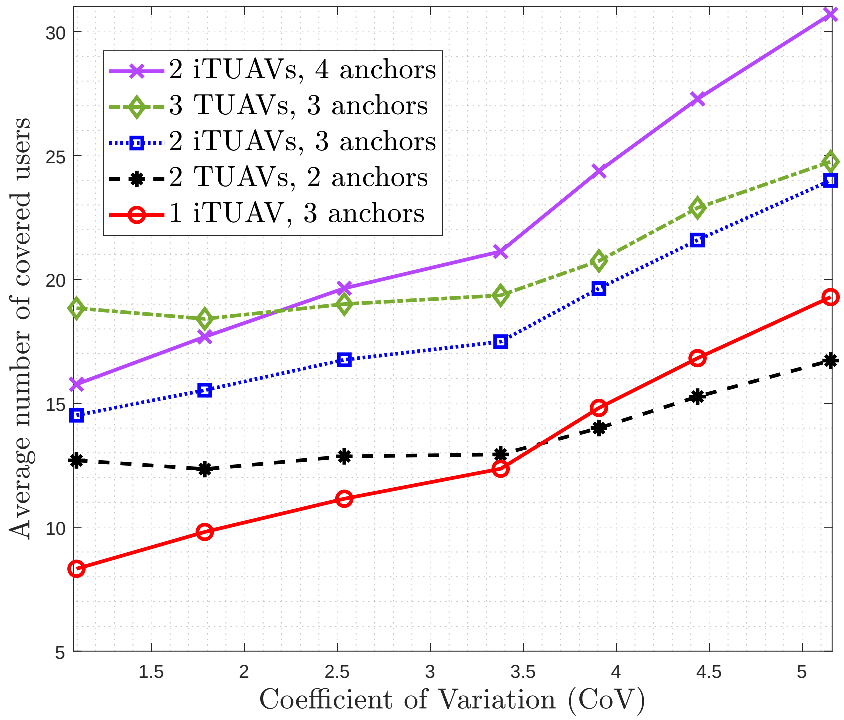

Fig. 8.5: Coverage performance of TUAV and iTUAV systems (different setups).

In Fig. 8.5, we illustrate the cellular coverage performance of iTUAV and TUAV systems with multiple UAVs as function of the CoV. When the users are very clustered, the iTUAV system performance mainly depends on the number of anchors, and a system with only 1 active iTUAV but 3 anchor locations even outperforms a system with 2 fixed TUAVs. A system with only 2 iTUAVs and 4 anchor locations, clearly achieves the best performance in clustered users scenarios. This is due to the opportunistic iTUAV behavior to move freely between anchors and associate with the best one. In contrast, the TUAV system has less leverage on relocating due to its static deployment.

8.5 Challenges and Future Directions

As research of TUAV and iTUAV systems is in its infancy, several challenges remain to be addressed. In what follows, we discuss some key issues:

- *New anchor, UAV, and tether designs:* Current TUAVs are built with the tether already attached at both anchor and UAV ends, such that attaching/detaching the tether must be executed manually. To achieve more flexibility to iTUAVs, two options can be considered: 1) the tether is within the anchor and it provides an easy-clip attach/detach system, but would require landing over the anchor to connect, or 2) the tether is within the iTUAV. The iTUAV drops the tether and the anchor "catches" it to establish the connection. The first option would require a longer power connection time than the second due to additional landing and taking-off, while the second option would require a careful "cable catching" mechanism to bypass environmental factors, such as strong winds and obstacles. The second option would also require a lightweight and inexpensive tether design to reduce impact on the UAV's size, weight, power and cost. For this matter, industry players, such as VICOR, are proposing to transfer high voltage over thin and lightweight tethers and to use small fixed-ratio bus converters within UAVs. Moreover, depending on whether the iTUAV will be equipped with a very lightweight tether or not, the challenge is to design automatic hold/release mechanical or electromagnetic winches and sockets at the stations and/or UAVs. Currently, similar conductive automatic charging systems are being prototyped for electric vehicles, such as the DAZEplug, which can inspire equivalent systems for iTUAVs. In addition, EasyAerial is on the right track with its Raptor UAV, which is capable of detaching itself from the tether.

- *Management of iTUAV operations:* The management of UAV operations is an active area of research a in the context of unmanned aircraft system traffic management (UTM). For iTUAVs, operations are slightly different since they can "jump" from one anchor to another and thus induce unpredictable environmental changes. This aspect should be considered when integrating iTUAV operations within UTM systems.

Also, iTUAV operations may be affected by the deployment strategy of anchors. For instance, vehicle-mounted anchors may change location, thus causing placement and trajectory updates for iTUAVs.

- *Integration of iTUAV with 5G and beyond technologies:* Although the proposed iTUAV system offers a tradeoff between the flexibility of UAVs and the unlimited power of TUAVs, their performance is still suboptimal. To further enhance iTUAV communications, other technologies can be leveraged, such as reconfigurable smart surfaces (RISs) and device-to-device (D2D) communications. Specifically, RIS and D2D communications can extend the coverage area of an iTUAV and thus reduce the number of required anchors. Such approaches are expected to drastically reduce the deployment costs of iTUAV systems.

8.6 Conclusion

With the proliferation of UAV-based applications and the recent development of TUAVs, iTUAV systems are envisioned in this article as an intermediate solution that offers a tradeoff between the continuous power supply of TUAVs and the mobility of UAVs. In this Chapter, we first provided an overview of UAV-based communications, including UAV-BSs and TUAVs. Then, we proposed the iTUAV system and detailed its components, operation mode, and distinguishing features. Through a case study, we evaluated the coverage performance of the proposed iTUAV system and compared it to UAV-BS and TUAV counterparts. Preliminary results demonstrated the potential of iTUAV systems to sustain long and reliable cellular connectivity missions. However, several issues need to be addressed before their extensive deployment. Finally, even though in this Chapter iTUAV systems were proposed mainly for ground users, they can be easily extended to serve aerial users.

Chapter 9

Summary and Future Work

9.1 Summary

The UAV technology is becoming mature, stable, and secure. Hence, UAVs are expected to be omnipresent over a wide range of applications including smart transportation systems, smart agriculture, cargo delivery, etc. Equipped with a BS, a UAV can be deployed easily and quickly to extend terrestrial and aerial users cellular coverage. Whether the deployment of UAVs needs cellular connectivity (UAV-UEs) or provides cellular coverage (UAV-BSs), it is crucial to investigate the performances of such systems, in order to optimize their deployment and ensure their coexistence with terrestrial cellular networks.

In Chapters 2 and 3, using tools from stochastic geometry, we studied the performance of UAV-UEs in VHetNets composed of a UAV-BSs based network and a terrestrial network. The results showed that the association probabilities of the UAV-UEs strongly dependent on 1) the altitude of the UAV-UEs, 2) the altitude of the UAV-BSs and 3) the terrestrial BSs environment. Specifically, a UAV-UE tends to be associated with a UAV-BS when 1) hovering at a very low altitude in dense environments or 2) hovering at a very high altitude. LoS interference from UAV-BSs and terrestrial-BSs drastically degrades the UAV-UE performance. Thus, orthogonal spectrum sharing between terrestrial BSs and UAV-BSs substantially alleviate the interference leading to a better UAV-UE performance. Moreover, at a very high altitude, the UAV-UE performance study can boil down to only two sets of BSs, namely the UAV-BSs and LoS terrestrial BSs. Finally, our work showed that the denser is the network of UAV-BSs, the worse is the performance of the UAV-UE, especially when hovering at low altitudes.

The aforementioned results motivated us to investigate in Chapter 4 the deployment of stand-alone UAV-BSs for UAV-UEs' cellular coverage, while accounting for different spectrum sharing policies between aerial and terrestrial BSs. In this context, the 3D placement problem of the UAV-BS was formulated as a mixed integer non-linear programming and was solved through iterative search. Results showed that UAV-BSs with wider antenna beamwidth tend to hover at low altitudes in order to cover more UAV-UEs under an orthogonal spectrum sharing (OSS) policy between terrestrial and aerial BSs. In contrast, under non-OSS (N-OSS), the optimal UAV-BS altitude is always the lowest authorized one by the regulation. Moreover, our investigation showed that an optimal total transmit power that maximizes the UAV-BS coverage exists, which increases with a tighter UAV-BS beamwidth. The work conducted in Chapter 4 drew multiple recommendations and design guidelines for the deployment and placement of the stand-alone UAV-BS for aerial users coverage.

In Chapter 5, we presented our vision for massive air delivery missions as the key enabler of the retail transformation. Indeed, we introduced a complete framework for the design of *3D aerial highways*. This new paradigm mainly discussed the coordination of a massive number of cargo-UAV deliveries and how such busy and dynamic aerial routes are designed. Also, the cellular connectivity for number of aerial users was thoroughly investigated. We concluded that a reliable cellular connectivity for cargo-UAVs is better guaranteed with at least two types of wireless networks.

Aligned with the same line of research as Chapter 5, we proposed a cellular disconnectivity-aware energy-efficient algorithm for cargo-UAV trajectory planning with minimum handoffs in Chapter 6. The results have shown that more stringent cellular connectivity requirements increase both the on-board energy consumption and handoff rate due to longer trajectories. Also, it is recommended that cargo-UAVs with a high tolerance to cellular disconnectivity fly at the lowest allowed altitude in order to reduce its energy consumption.

Finally, when operating above low density terrestrial environments, e.g., rural, cargo-UAVs tend to consume less energy thanks to the very low inter-cell interference.

In Chapter 7, we proposed a novel energy-efficient RL-based trajectory planning and cell association algorithm for cargo-UAVs. Results showed that the proposed RL-based algorithm significantly reduces the needed handoff along by smartly associating the cargo-UAV with the best terrestrial-BS while maintaining 1) its cellular link with serving terrestrial-BS at an acceptable reliability level, and 2) the on-board battery drainage at a close level to the shortest trajectory benchmark. This means that the saving on the signalling overhead, thanks to reduced handoff rate, and the acceptable cellular link reliability, come at the slightest expense of energy consumption.

In Chapter 8, based on the urgent need to find a tradeoff between the limitation of the energy supply of the UAV-BS and the static deployment of TUAV, we introduced a new system referred as iTUAV that overcomes the UAV-BS on-board capacity and the limited TUAV mobility. More specifically, the iTUAV, with the help of optimally deployed anchor nodes, will provide cellular coverage for users when tethered to an anchor node and travel to a more optimal anchor node in order to maintain cellular reliability. When compared against UAV-BAS and TUAV systems, the performance of the proposed iTUAV-based system proved its capability to sustain long and reliable cellular connectivity missions with a well designed anchors network.

9.2 Future Research Directions

Even with the extensive studies on both cellular-connected UAV and UAV-BS, there are still some issues that should be addressed. In this section, we discuss some worth-to investigate possibilities for the extension of the current work.

9.2.1 Flexible 3D trajectory planning for cargo-UAV for offline and online missions

In Chapters 6 and 7, we investigated the trajectory planning for a cargo-UAV while relying only on the terrestrial network's cellular connectivity. Our previous work assumed that the cargo-UAV presets an altitude of flying, vertically ascends to that altitude, then travels horizontally toward the drop-off location, and finally descends vertically to the destination. Constraining the cargo-UAV trajectory planning on only vertical or horizontal moves may force the latter to travel longer distances, thus consuming more energy to accomplish its delivery mission. Moreover, under stringent cellular disconnectivity, the energy-efficient cargo-UAV trajectory planning may be unfeasible under the limited allowed moves (only vertical and horizontal). Consequently, the problems in Chapters 6 and 7 with more relaxed 3D motion constraints. Specifically, a cargo-UAV can move freely in a gridded 3D space. This would allow more flexibility for the cargo-UAV to move efficiently toward its destination with less cellular disconnectivity and less handoff rate. For efficient offline and online UAV trajectory planning/operating, sophisticated dynamic programming and machine learning algorithms can be used.

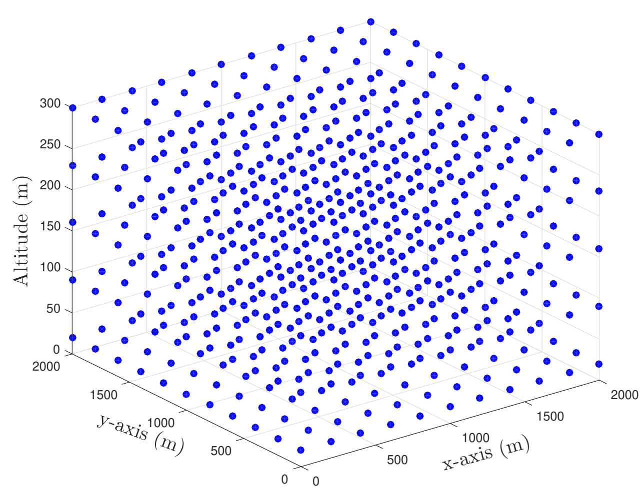

Fig. 9.1: 3D Airspace grid system.

We assume that a delivery mission to a consumer is accommodated by a cargo-UAV

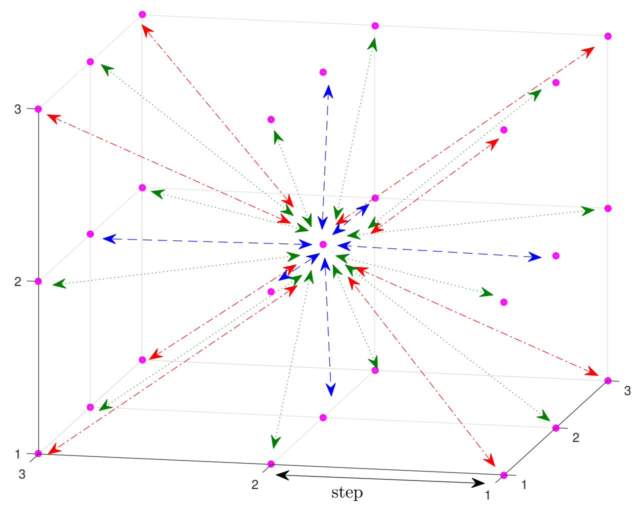

Fig. 9.2: Possible cargo-UAV moves where the magenta filled dots are a possible cargo-UAV location with its RSRP and serving BS ID.

through the 3D airspace with the Cartesian coordinate system (x, y, z). The imminent deployment of cargo-UAVs requires the stringent need for reliable and seamless cellular connectivity. Indeed, to ensure the safety and security of the cargo-UAV missions, command a control information exchanges between the cargo-UAV and a ground control center are crucial to monitor and proactively intervene in case of an emergency. Since the terrestrial network has matured over the last decades, it is seen as a stable candidate to provide cellular connectivity for cargo-UAVs. Although the terrestrial network was primarily deployed to serve users on the ground, yet, it can be re-utilized to assure cellular connectivity for aerial users. The feasibility of such as system has been investigated by the 3GPP report [2].

In this system, it can be assumed that the motion directions of the cargo-UAV are not limited in the 3D space. Subsequently, we show in Fig. 9.1 the gridded space to quantify any possible 3D location during the cargo-UAV mission. Each position would be characterized by its reference signal received power and the ID of the serving BS, i.e., the cargo-UAV is associated with the terrestrial BS that guarantees the highest averaged received power. Thus, the cargo-UAV has at most 26 possible moves (horizontal, vertical and inclined) as shown in Fig. 9.2. The optimal path travelled by the cargo-UAV is a mixture of horizontal, vertical, and inclined moves.

9.2.2 Backhaul constrained HAPS-SMBS deployment for cellular-connected UAVs

Owing to the great promises of high altitude platform station super macro BS (HAPS-SMBS), such as its extended period of operation, reliable wide coverage, and low latency, it is seen as a strong connectivity candidate for UAV operations [77]. As a future work, the optimal deployment of HAPS-SMBS for minimum UAVs power transmission under HAPS-SMBS backhaul capacity limits can be investigated. We assume that the HAPS-SMBS' backhaul is a free-space optics (FSO) link towards an earth gateway [109]. Then, the problem can be formulated through the joint optimization of the UAVs transmit powers and HAPS-SMBS 3D location, under UAVs' QoS and FSO backhaul capacity constraints.

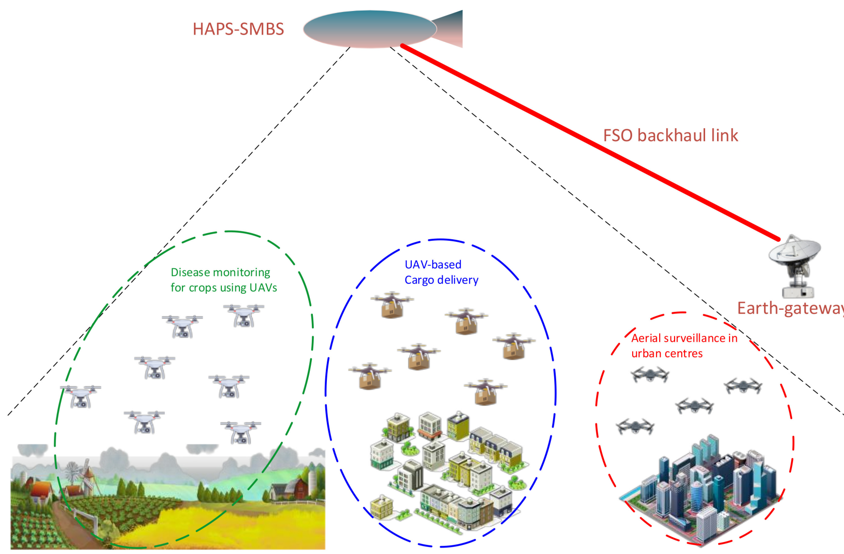

Fig. 9.3: HAPS-SMBS based wireless network for various use cases of cellular-connected UAVs. Cargo-UAV needs reliable cellular transmission link for C&C exchanges for their BVLoS missions. UAVs can be equipped with HD camera for urban centres aerial surveillance where the streaming of the data needs high-throughput wireless link. Smart agriculture is enabled with UAVs monitoring crops for diseases, humidity and irritation. UAVs in the range of scenarios depicted in this figure needs wireless link to ensure 1) the safety and security of the UAV BVLoS missions and 2) offloading the collected data back to an earth gateway for processing. HAPS-SMBS is envisioned to provide wide coverage and enhanced capacity for these heterogeneous cellular-connected UAVs in terms of QoS requirements.

APPENDICES

Appendix A

Appendices of Chapter 2

A.1 Proof of Lemma 2.1

The association probability to a terrestrial-BS can be written as

$$\begin{aligned}
\mathcal{A}_{\mathrm{T}} = & \mathbb{P}\left(\mu'_T R_T^{-\alpha_T} \geqslant \mu'_A R_A^{-\alpha_A}\right) = \mathbb{P}\left(R_A \geqslant \left(\frac{\mu'_A}{\mu'_T}\right)^{\frac{1}{\alpha_A}} R_T^{\frac{\alpha_T}{\alpha_A}}\right) \\
\overset{(a)}{=} & \int_{h_{\mathrm{UT}}}^{\infty} F_{R_A}^{(c)}\left(\left(\frac{\mu'_A}{\mu'_T}\right)^{\frac{1}{\alpha_A}} r^{\frac{\alpha_T}{\alpha_A}}\right) f_{R_T}(r)dr \qquad \text{(A.1)} \\
\overset{(b)}{=} & 1 - \left(\int_{h_{\mathrm{UT}}}^{\zeta_{\mathrm{A}}^{\mathrm{T}}(h_{\mathrm{UA}})} F_{R_A}\left(\left(\frac{\mu'_A}{\mu'_T}\right)^{\frac{1}{\alpha_A}} r^{\frac{\alpha_T}{\alpha_A}}\right) f_{R_T}(r)dr\right. \\
& + \int_{\zeta_{\mathrm{A}}^{\mathrm{T}}(h_{\mathrm{UA}})}^{\zeta_{\mathrm{A}}^{\mathrm{T}}(d)} F_{R_A}\left(\left(\frac{\mu'_A}{\mu'_T}\right)^{\frac{1}{\alpha_A}} r^{\frac{\alpha_T}{\alpha_A}}\right) f_{R_T}(r)dr \\
& \left. + \int_{\zeta_{\mathrm{A}}^{\mathrm{T}}(d)}^{\infty} f_{R_T}(r)dr\right) \\
\overset{(c)}{=} & 1 - \exp\left(-\pi\lambda_{\mathrm{T}}\left(\zeta^2 - h_{\mathrm{UT}}^2\right)\right) + \frac{2\pi\lambda_{\mathrm{T}}\exp\left(\pi\lambda_{\mathrm{T}}h_{\mathrm{UT}}^2\right)}{r_{\mathrm{D}}^{2N}} \\
& \times \int_{\zeta}^{\zeta_{\mathrm{A}}^{\mathrm{T}}(d)} r\exp\left(-\pi\lambda_{\mathrm{T}}r^2\right)\left(d^2 - \left(\frac{\mu'_A r^{\alpha_T}}{\mu'_T}\right)^{\frac{2}{\alpha_A}}\right)^N dr, \qquad \text{(A.2)}
\end{aligned}$$

where $\mu'_\nu = B_\nu \times \mu_\nu$ and (a) follows from the definition of the Complementary CDF, i.e., $F_X^{(c)}(x) = 1 - F_X(x)$ and averaging over R_T, (b) is obtained from excluding the range of R_A over which $F_{R_A}^{(c)} = 0$. Plugging (2.8) and (2.11) into (A.1) yield (c). Finally, using the

Binomial theorem [34, 1.111] and the upper incomplete Gamma function [34, 8.350.2] with some mathematical manipulations complete the proof.

A.2 Proof of Lemma 2.2

The CDF of $\tilde{R}_T$ can be expressed as

$$\begin{aligned}
F_{\tilde{R}_T}(r) &= \mathbb{P}\left[R_T < r | \mathcal{E}_\mathrm{T}\right] \overset{(a)}{=} \frac{\mathbb{P}\left[R_T < r; \mathcal{E}_\mathrm{T}\right]}{\mathbb{P}[\mathcal{E}_\mathrm{T}]} \\
&= \frac{\mathbb{P}\left[R_T \leqslant r; R_A \geqslant \tau_{A|\mathcal{E}_\mathrm{T}}(r)\right]}{\mathcal{A}_\mathrm{T}} \\
&\overset{(b)}{=} \frac{1}{\mathcal{A}_\mathrm{T}} \int_{h_\mathrm{U}}^{r} F_{R_A}^{(c)}(\tau_{A|\mathcal{E}_\mathrm{T}}(x)) f_{R_T}(x) dx,
\end{aligned} \tag{A.3}$$

where (a) follows from applying Bayes' rule and (b) is obtained by averaging over R_T. Finally, differentiating (A.3) over r using Leibniz's rule completes the proof.

A.3 Proof of Lemma 2.4

Conditioned on $\mathcal{E}_\nu$, $\nu \in \{\mathrm{T}, \mathrm{A}\}$, the Laplace transform of the aggregated terrestrial interference power can be written as

$$\begin{aligned}
&\mathcal{L}_{I_T|\mathcal{E}_\nu}(s) = \mathbb{E}_{I_T|\mathcal{E}_\nu}\left[\exp(-s(I_T))\right] \\
&\overset{(a)}{=} \mathbb{E}_{\Phi_\mathrm{T}}\left[\prod_{x_j \in \Phi_\mathrm{T} \setminus x_0} \mathbb{E}_{\mathrm{H}_T^{x_j}}\left[\exp\left(-s\mu_T \mathrm{H}_T^{x_j} d_{T,x_j}^{-\alpha_T}\right)\right]\right] \\
&\overset{(b)}{=} \mathbb{E}_{\Phi_\mathrm{T}}\left[\prod_{x_j \in \Phi_\mathrm{T} \setminus x_0} \left(\frac{m_T}{m_\omega + s\mu_T d_{T,x_j}^{-\alpha_T}}\right)^{m_T}\right] \\
&\overset{(c)}{=} \exp\left(-2\pi\lambda_\mathrm{T} \int_{\tau_{T|\mathcal{E}_\nu}(r)}^{\infty} y \left(1 - \left(\frac{m_T}{m_T + s\mu_T y^{-\alpha_T}}\right)^{m_T}\right) dy\right) \\
&\overset{(d)}{=} \exp\left(-2\pi\lambda_\mathrm{T} s\mu_T \sum_{i=0}^{m_T-1} m_T^{m_T-1-i} \int_{\tau_{T|\mathcal{E}_\nu}(r)}^{\infty} y^{1-\alpha_T} \right. \\
&\qquad \left. \times (m_T + s\mu_T y^{-\alpha_T})^{i-m_T} dy\right),
\end{aligned} \tag{A.4}$$

where (a) follows from (2.6) and the independence of the small-scale fading and the PPP, (b) is obtained from using the moment generating function of Gamma distribution. (c) follows from substituting $y = d_{T,x_j}$ and using the probability generating functional (PGFL) of the PPP, (d) follows from using the identity $a^n - b^n = (a-b)\sum_{i=0}^{n-1} a^i b^{n-1-i}$. Finally, using [59, Eq.(1.43)] and [34, 7.811.2] with the binomial theorem [34, 1.111] completes the proof.

A.4 Proof of Lemma 2.5

It was proven in [26, Corollary 3] that given that the serving BS (either terrestrial-BS or aerial-BS) is located at a distance r from the aerial user, the distribution of the distance between the aerial user and the j-th interfering aerial-BS $d_{A,x_j}, j \in [1, N']$, is given by

$$f_{d_{A,x_j}}(t) = \begin{cases} \frac{2t}{d^2 - r^2}, & r \leqslant t \leqslant d, \\ 0, & \text{otherwise} \end{cases}, \tag{A.5}$$

where N' is the number of interfering aerial-BSs. Note that there are $N' - i$ interfering aerial-BSs that have a gain of G_A with a probability q_{A} and i interfering aerial-BSs that has a gain of g_A with probability $1 - q_{\mathrm{A}}$. Hence, i follows a Binomial distribution, $\mathcal{B}(N', q_{\mathrm{A}})$. Indeed, the two subsets of interferes (those with gain G_A and those with gain g_A) are dependent where the joint distribution of $(N' - i, i)$ is multinomial distribution on N' trials with success probabilities $(q_{\mathrm{A}}, 1 - q_{\mathrm{A}})$.

Conditioned on $\mathcal{E}_\nu, \nu \in \{\mathrm{T}, \mathrm{A}\}$, the Laplace transform of the aerial interference can be expressed as

$$
\begin{aligned}
&\mathcal{L}_{I_A}(s|\mathcal{E}_\nu) = \mathbb{E}_{I_A}\left[\exp(-s(I_A))|\mathcal{E}_\nu\right] \\
&= \mathbb{E}_{d_{A,x_j}}\left[\prod_{j=1}^{N'} \mathbb{E}_{\mathrm{H}_A^{x_j}}\left[\exp\left(-sP_A B_A G_r \eta_A \mathrm{H}_A^{x_j} d_{A,x_j}^{-\alpha_A}\right)\right]\right] \\
&\overset{(a)}{=} \prod_{j=1}^{N'}\left[\mathbb{E}_{d_{A,x_j}}\left[\left(\frac{m_A}{m_A + sP_A B_A G_r \eta_A d_{A,x_j}^{-\alpha_A}}\right)^{m_A}\right]\right] \\
&\overset{(b)}{=} f_i(i)\left[\mathbb{E}_{d_{A,x_j}}\left[\left(\frac{m_A}{m_A + sP_A B_A \eta_A G_A d_{A,x_j}^{-\alpha_A}}\right)^{m_A}\right]\right]^{N'-i} \\
&\times \left[\mathbb{E}_{d_{A,x_j}}\left[\left(\frac{m_A}{m_A + sP_A B_A \eta_A g_A d_j^{-\alpha_A}}\right)^{m_A}\right]\right]^{i} \\
&\overset{(c)}{=} \sum_{i=0}^{N'} \binom{N'}{i} q_A^{N'-i}(1-q_{\mathrm{A}})^i \\
&\left[\int_{\tau_{A|\mathcal{E}_\nu}(r)}^{d} \left(\frac{m_A}{m_A + sP_A B_A \eta_A G_A t^{-\alpha_A}}\right)^{m_A} \frac{2t}{d^2 - r^2} dt\right]^{N'-i} \\
&\left[\int_{\tau_{A|\mathcal{E}_\nu}(r)}^{d} \left(\frac{m_A}{m_A + sP_A B_A \eta_A g_A t^{-\alpha_A}}\right)^{m_A} \frac{2t}{d^2 - r^2} dt\right]^{i},
\end{aligned} \tag{A.6}
$$

where (a) follows from the expectation of Gamma distribution, (b) follows from the binomial distribution of i with $f_i(i) = \sum_{i=0}^{N'} \binom{N'}{i} q_{\mathrm{A}}^{N'-i}(1-q_{\mathrm{A}})^i$, (c) is obtained from averaging over d_{A,x_j}. Finally, using the identity $(1+z)^a = 1/\Gamma(-a)\mathrm{G}_{1,1}^{1,1}[z|{}^{1-a}_{0}]$ and [34, 7.811.2], and with some mathematical manipulations, we complete the proof.

A.5 Proof of Theorem 2.6

By applying the law of total probability, the downlink coverage probability can be expressed as

$$
\mathcal{C} = \sum_{\nu \in \{\mathrm{T},\mathrm{A}\}} \mathcal{A}_\nu \times \mathcal{C}_\nu, \tag{A.7}
$$

where $\mathcal{C}_\nu$ denotes the coverage probability given that the aerial user is associated with the tier ν of BSs. $\mathcal{C}_\nu$ can be written as

$$\begin{aligned}\mathcal{C}_\nu = &\mathbb{P}(\gamma \geqslant T) \overset{(a)}{=} \mathbb{E}_{\mathrm{H}_\nu^{x_0},\tilde{R}_\nu,I}\left[\mathbb{P}\left(\frac{\mu_\nu \mathrm{H}_\nu^{x_0} r_\nu^{-\alpha_T}}{I} \geqslant T\right)\right]\\ &\overset{(b)}{=} \mathbb{E}_{\tilde{R}_\nu,I}\left[\mathbb{E}_{\mathrm{H}_\nu^{x_0}}\left[\mathbb{P}\left(\mathrm{H}_\nu^{x_0} \geqslant \frac{r_\nu^{\alpha_T} T I}{\mu_\nu}\right)\right]\right]\\ &\overset{(c)}{=} \mathbb{E}_{\tilde{R}_\nu}\left[\mathbb{E}_I\left[\frac{\Gamma\left(m_\nu, \frac{m_\nu T r^{\alpha_\nu} I}{\mu_\nu}\right)}{\Gamma(m_\nu)}\right]\right] \overset{(d)}{=} \sum_{k=0}^{m_\nu-1}\frac{1}{k!}\left(\frac{m_\nu T}{\mu_\nu}\right)^k\\ &\times \mathbb{E}_{\tilde{R}_\nu}\left[r^{k\alpha_\nu}\mathbb{E}_I\left[I^k \exp\left(\frac{-m_\nu T r^{\alpha_\nu} I}{\mu_\nu}\right)\right]\right], \qquad \text{(A.8)}\end{aligned}$$

where (a) follows from averaging over $\mathrm{H}_\nu^{x_0}$, $\tilde{R}_T$, and I, where $I = I_T + I_A$, (b) is obtained from the independence of $\mathrm{H}_\nu^{x_0}$, $\tilde{R}_T$, and I. (c) follows from applying the CCDF of Gamma-distributed channel gain $\mathrm{H}_\nu^{x_0}$, (d) is obtained from the assumption that m_ν is an integer and using the series expansion of the upper incomplete Gamma function. Finally, using the identity $\mathbb{E}_I\left[I^k \exp(-sI)\right] = (-1)^k \frac{\partial \mathcal{L}_I(s)}{\partial s^k}$ and averaging over $\tilde{R}_\nu$ completes the proof.

Appendix B

Appendices of Chapter 3

B.1 Proof of Lemma 3.1

R_ν can be written as $R_\nu = \sqrt{Z_\nu^2 - h_{\rm UT}^2}$, $\nu \in \{\rm L, N\}$, where Z_ν is the horizontal distance between the aerial user and the nearest LoS and NLoS terrestrial-BSs. Using the null probability of PPP [32], we have

$$F_{R_\nu}(r) = 1 - \mathbb{P}\left(R_\nu \geqslant r\right) \stackrel{(a)}{=} 1 - \exp\left(-2\pi \int_{h_{\rm UT}}^{r} \lambda_{\rm T} t P_\nu(t) dt\right). \tag{B.1}$$

Since $r = \sqrt{z^2 + h_{\rm UT}^2}$, taking the integral in (a) with respect to z completes the proof of (3.14) (note that t is a dummy variable). (3.13) can be obtained by differentiating $F_{R_\nu}(r)$ with respect to r.

B.2 Proof of Lemma 3.2

The association probability of an aerial user with an LoS terrestrial-BS can be written as

$$\begin{aligned}
\mathcal{A}_{\rm L} &= \mathbb{P}\left(\mu_L R_L^{-\alpha_L} \geqslant \mu_N R_N^{-\alpha_N}; \mu_L R_L^{-\alpha_L} \geqslant \mu_A R_A^{-\alpha_A}\right) \\
&\stackrel{(a)}{=} \mathbb{P}\left(\mu_L R_L^{-\alpha_L} \geqslant \mu_N R_N^{-\alpha_N}\right) \times \mathbb{P}\left(\mu_L R_L^{-\alpha_L} \geqslant \mu_A R_A^{-\alpha_A}\right) \\
&= \mathbb{P}\left(R_N \geqslant \tau_{N|\mathcal{E}_{\rm L}}(r)\right) \times \mathbb{P}\left(R_A \geqslant \tau_{A|\mathcal{E}_{\rm L}}(r)\right) \qquad \text{(B.2)} \\
&\stackrel{(b)}{=} \left(\int_{h_{\rm UT}}^{\infty} F_{R_N}^{(c)}\left(\tau_{N|\mathcal{E}_{\rm L}}(r)\right) f_{R_L(r)} dr\right) \times \left(\int_{h_{\rm UT}}^{\infty} F_{R_A}^{(c)}\left(\tau_{A|\mathcal{E}_{\rm L}}(r)\right) f_{R_L}(r) dr\right), \qquad \text{(B.3)}
\end{aligned}$$

where (a) follows from the independence of the two point processes that represent the aerial-BSs and terrestrial-BSs, (b) follows from the definition of the Complementary CDF and averaging over R_L. Finally, using (3.14) and (3.16) along with some mathematical manipulations completes the proof.

B.3 Proof of Lemma 3.4

The CDF of $\tilde{R}_L$ can be written as

$$
\begin{aligned}
F_{\tilde{R}_L|\mathcal{E}_\mathrm{L}}(r) &= \mathbb{P}\left[R_L < r|\mathcal{E}_\mathrm{L}\right] \overset{(a)}{=} \frac{\mathbb{P}\left[R_L < r; \mathcal{E}_\mathrm{L}\right]}{\mathbb{P}[\mathcal{E}_\mathrm{L}]} \overset{(b)}{=} \frac{\mathbb{P}\left[R_L \leqslant r; (R_A \geqslant \tau_{A|\mathcal{E}_\mathrm{L}}(r); R_N \geqslant \tau_{N|\mathcal{E}_\mathrm{L}}(r))\right]}{\mathcal{A}_\mathrm{L}} \\
&= \frac{\mathbb{P}\left[R_L \leqslant r; R_A \geqslant \tau_{A|\mathcal{E}_\mathrm{L}}(r)\right]\mathbb{P}\left[R_L \leqslant r; R_N \geqslant \tau_{N|\mathcal{E}_\mathrm{L}}(r)\right]}{\mathcal{A}_\mathrm{L}} \\
&\overset{(c)}{=} \frac{1}{\mathcal{A}_\mathrm{L}} \int_{h_\mathrm{UT}}^{r} F^{(c)}_{R_A}(\tau_{A|\mathcal{E}_\mathrm{L}}(r)) F^{(c)}_{R_N}(\tau_{N|\mathcal{E}_\mathrm{L}}(r)) f_{R_L}(x) dx,
\end{aligned} \tag{B.4}
$$

where (a) follows from Bayes' rule, (b) is obtained from (B.2), and (c) follows from averaging over R_L. Finally, differentiating (B.4) with respect to r completes the proof.

B.4 Proof of Lemma 3.7

The Laplace transform of the aggregated interference power is given by

$$
\begin{aligned}
&\mathcal{L}_{(I_N+I_L)|\mathcal{E}_\nu}(s) = \mathbb{E}_{(I_N+I_L)|\mathcal{E}_\nu}\left[\exp(-s(I_N+I_L))\right] \\
&\overset{(a)}{=} \mathbb{E}_{\Phi_\mathrm{L}}\left[\prod_{x_j\in\Phi_\mathrm{L}\setminus x_0} \mathbb{E}_{\mathrm{H}_\mathrm{L}^{x_j}}\left[\exp\left(-s\mu_L \mathrm{H}_\mathrm{L}^{x_j} d_{L,x_j}^{-\alpha_L}\right)\right]\right] \times \mathbb{E}_{\Phi_\mathrm{N}}\left[\prod_{x_j\in\Phi_\mathrm{N}\setminus x_0} \mathbb{E}_{\mathrm{H}_\mathrm{N}^{x_j}}\left[\exp\left(-s\mu_N \mathrm{H}_\mathrm{N}^{x_j} d_{N,x_j}^{-\alpha_N}\right)\right]\right] \\
&\overset{(b)}{=} \prod_{\omega\in\{\mathrm{L},\mathrm{N}\}}\left[\mathbb{E}_{\Phi_\omega}\left[\prod_{x_j\in\Phi_\omega\setminus x_0}\left(\frac{m_\omega}{m_\omega + s\mu_\omega d_{\omega,x_j}^{-\alpha_\omega}}\right)^{m_\omega}\right]\right],
\end{aligned} \tag{B.5}
$$

where (a) follows from (3.11) and the independence of the small-scale fading and PPP, and (b) is obtained from the moment generating function of the Gamma distribution. Finally, using the probability generating functional (PGFL) and the results in Table 3.4 complete the proof.

B.5 Proof of Lemma 3.8

It was proven in [26, Corollary 3] that when the serving BS (either terrestrial-BS or aerial-BS) is located at a distance r from the aerial user, the distribution of the distance between the aerial user and the j-th interfering aerial-BS $d_{A,x_j}, j \in [1, N']$ is given by

$$f_{d_{A,x_j}}(d_j) = \begin{cases} \frac{2d_j}{d^2-r^2}, & r \leqslant d_j \leqslant d \\ 0, & \text{Otherwise} \end{cases}, \tag{B.6}$$

where N' is the number of interfering aerial-BSs. It should be noted that there are $N'-i$ interfering aerial-BSs that have a gain of $G_{\mathrm{m}}^{\mathrm{A}}$ with a probability q_{A} and i interfering aerial-BSs that have a gain of $g_{\mathrm{s}}^{\mathrm{A}}$ with a probability of $1-q_{\mathrm{A}}$. Hence, i follows a Binomial distribution $\mathcal{B}(N', q_{\mathrm{A}})$. Indeed, the two subsets of interfering aerial-BSs (those with a gain of $G_{\mathrm{m}}^{\mathrm{A}}$ and those with a gain $g_{\mathrm{s}}^{\mathrm{A}}$) are dependent where the joint distribution of $N'-i$ and i is a multinomial distribution on N' trials with success probabilities q_{A} and $1-q_{\mathrm{A}}$, respectively.

The Laplace transform of the interference received from aerial-BSs is given by

$$\begin{aligned}
\mathcal{L}_{I_A|\mathcal{E}_\nu}(s) &= \mathbb{E}_{I_A|\mathcal{E}_\nu}\left[\exp(-sI_A)\right] = \mathbb{E}_{d_{A,x_j}}\left[\prod_{j=1}^{N'} \mathbb{E}_{\mathrm{H}_A^{x_j}}\left[\exp\left(-sP_A G^{\mathrm{A}}(d_j)\mathrm{H}_A^{x_j} d_j^{-\alpha_A}\right)\right]\right] \\
&\overset{(a)}{=} \prod_{j=1}^{N'}\left[\mathbb{E}_{d_{A,x_j}}\left[\left(\frac{m_A}{m_A + sP_A G^{\mathrm{A}}(d_j) d_j^{-\alpha_A}}\right)^{m_A}\right]\right] \overset{(b)}{=} f_i(i)\left[\mathbb{E}_{d_{A,x_j}}\left[\left(\frac{m_A}{m_A + sP_A G_{\mathrm{m}}^{\mathrm{A}} d_j^{-\alpha_A}}\right)^{m_A}\right]\right]^{N'-i} \\
&\quad \times \left[\mathbb{E}_{d_{A,x_j}}\left[\left(\frac{m_A}{m_A + sP_A g_{\mathrm{s}}^{\mathrm{A}} d_j^{-\alpha_A}}\right)^{m_A}\right]\right]^{i} \\
&\overset{(c)}{=} \sum_{i=0}^{N'}\binom{N'}{i} q_{\mathrm{A}}^{N'-i}(1-q_{\mathrm{A}})^i \left[\int_{\tau_{A|\mathcal{E}_\nu}(r))}^{d}\left(\frac{m_A}{m_A + sP_A G_{\mathrm{m}}^{\mathrm{A}}\eta_A t^{-\alpha_A}}\right)^{m_A}\frac{2t}{d^2-r^2}dt\right]^{N'-i} \\
&\quad \times \left[\int_{\tau_{A|\mathcal{E}_\nu}(r))}^{d}\left(\frac{m_A}{m_A + sP_A g_{\mathrm{s}}^{\mathrm{A}}\eta_A t^{-\alpha_A}}\right)^{m_A}\frac{2t}{d^2-r^2}dt\right]^{i},
\end{aligned} \tag{B.7}$$

where (a) follows from using the Gamma distribution of the small scale fading channel gain of the A2A link. (b) follows from the binomial distribution of i with $f_i(i) = \sum_{i=0}^{N'}\binom{N'}{i} q_{\mathrm{A}}^{N'-i}(1-q_{\mathrm{A}})^i$. (c) is obtained after averaging over d_j. Using the identity $(1+z)^a = 1/\Gamma(-a)\mathrm{G}_{1,1}^{1,1}[z|\,{}^{1-a}_{0}]$ and [34, eq(7.811.2)] along with some additional mathematical manipulations, (3.27) is obtained.

B.6 Proof of Theorem 3.11

The coverage probability conditioned on the event that the aerial user is connected to a BS from Φ_ν, $\nu \in \{\mathrm{L}, \mathrm{N}, \mathrm{A}\}$, is given by

$$\begin{aligned}\mathcal{C}_\nu &= \mathbb{P}(\gamma \geqslant T) \overset{(a)}{=} \mathbb{E}_{\mathrm{H}_\nu^{x_0}, \tilde{R}_\nu, I}\left[\mathbb{P}\left(\frac{\mu_\nu \mathrm{H}_\nu^{x_0} r_\nu^{-\alpha_L}}{I+\sigma^2} \geqslant T\right)\right] \overset{(b)}{=} \mathbb{E}_{\tilde{R}_\nu, V}\left[\mathbb{E}_{\mathrm{H}_\nu^{x_0}}\left[\mathbb{P}\left(\mathrm{H}_\nu^{x_0} \geqslant \frac{r_\nu^{\alpha_L} T V}{\mu_\nu}\right)\right]\right] \\ &\overset{(c)}{=} \mathbb{E}_{\tilde{R}_\nu}\left[\mathbb{E}_V\left[\frac{\Gamma\left(m_\nu, \frac{m_\nu T r^{\alpha_\nu} V}{\mu_\nu}\right)}{\Gamma(m_\nu)}\right]\right] \overset{(d)}{=} \sum_{k=0}^{m_\nu - 1} \frac{1}{k!}\left(\frac{m_\nu T}{\mu_\nu}\right)^k \mathbb{E}_{\tilde{R}_\nu}\left[r^{k\alpha_\nu} \mathbb{E}_V\left[V^k \exp\left(\frac{-m_\nu T r^{\alpha_\nu} V}{\mu_\nu}\right)\right]\right], \end{aligned} \tag{B.8}$$

where (a) follows from averaging the coverage probability over the random variables, $\{\mathrm{H}_\nu^{x_0}, \tilde{R}_\nu, V\}$ and (b) is obtained by exploiting the independence between the three random variables. Moreover in (B.8), (c) follows after applying the CCDF of Gamma-distributed channel gain $\mathrm{H}_\nu^{x_0}$, and (d) is obtained by assuming m_ν to be an integer and using the series expansion of the upper incomplete Gamma function. Finally, using the identity, i.e., $\mathbb{E}_V\left[V^k \exp(-sV)\right] = (-1)^k \frac{\partial \mathcal{L}_V(s)}{\partial s^k}$, and averaging over $\tilde{R}_\nu$, we obtain (3.35).

References

[1] A. Colpaert, E. Vinogradov, and S. Pollin, "Aerial coverage analysis of cellular systems at LTE and mmwave frequencies using 3D city models," *Sensors*, vol. 18, no. 12, p. 4311, Dec. 2018.

[2] 3GPP, "Study on enhanced LTE support for aerial vehicles (release 15), TR 36.777," Jun. 2018.

[3] N. Cherif, W. Jaafar, H. Yanikomeroglu, and A. Yongacoglu, "3D aerial highway: The key enabler of the retail industry transformation," *IEEE Commun. Mag.*, vol. 59, no. 9, pp. 65–71, Sep. 2021.

[4] I. Bor-Yaliniz, A. El-Keyi, and H. Yanikomeroglu, "Efficient 3-D placement of an aerial base station in next generation cellular networks," in *Proc. IEEE Int. Conf. Commun. (ICC)*, Kuala Lumpur, Malaysia, May 2016, pp. 1–5.

[5] M. Mozaffari, W. Saad, M. Bennis, Y.-H. Nam, and M. Debbah, "A tutorial on UAVs for wireless networks: Applications, challenges, and open problems," *IEEE Commun. Surv. Tutorial*, vol. 21, no. 3, pp. 2334–2360, Thirdquarter 2019.

[6] M. Mozaffari, W. Saad, M. Bennis, and M. Debbah, "Mobile unmanned aerial vehicles (UAVs) for energy-efficient internet of things communications," *IEEE Trans. Wireless Commun.*, vol. 16, no. 11, pp. 7574–7589, Nov. 2017.

[7] E. Kalantari, H. Yanikomeroglu, and A. Yongacoglu, "On the number and 3D placement of drone base stations in wireless cellular networks," in *Proc. IEEE Veh. Tech. Conf. (VTC-Fall)*, Montreal, QC, Canada, Sep. 2016, pp. 1–6.

[8] E. Kalantari, I. Bor-Yaliniz, A. Yongacoglu, and H. Yanikomeroglu, "User association and bandwidth allocation for terrestrial and aerial base stations with backhaul considerations," in *Proc. IEEE Int. Symp. on Pers., Indoor and Mobile Radio Commun. (PIMRC)*, Montreal, QC, Canada, Oct. 2017, pp. 1–6.

[9] R. Amer, W. Saad, H. ElSawy, M. M. Butt, and N. Marchetti, "Caching to the sky: Performance analysis of cache-assisted CoMP for cellular-connected UAVs," in *Proc. IEEE Wireless Commun. Netw. Conf. (WCNC)*, Marrakech, Morocco, Apr. 2019, pp. 1–6.

[10] M. M. Azari, F. Rosas, A. Chiumento, and S. Pollin, "Coexistence of terrestrial and aerial users in cellular networks," in *Proc. IEEE Glob. Commun. Conf. (Globecom) Workshops*, Singapore, Dec. 2017, pp. 1–6.

[11] M. M. Azari, F. Rosas, and S. Pollin, "Cellular connectivity for UAVs: Network modeling, performance analysis, and design guidelines," *IEEE Trans. Wireless Commun.*, vol. 18, no. 7, pp. 3366–3381, Jul. 2019.

[12] A. Fotouhi, H. Qiang, M. Ding, M. Hassan, L. G. Giordano, A. Garcia-Rodriguez, and J. Yuan, "Survey on UAV cellular communications: Practical aspects, standardization advancements, regulation, and security challenges," *IEEE Commun. Surveys Tuts.*, vol. 21, no. 4, pp. 3417–3442, Firstquarter 2019.

[13] M. Alzenad, A. El-Keyi, F. Lagum, and H. Yanikomeroglu, "3-D placement of an unmanned aerial vehicle base station (UAV-BS) for energy-efficient maximal coverage," *IEEE Wireless Commun. Lett.*, vol. 6, no. 4, pp. 434–437, Aug. 2017.

[14] M. Alzenad, A. El-Keyi, and H. Yanikomeroglu, "3-D placement of an unmanned aerial vehicle base station for maximum coverage of users with different QoS requirements," *IEEE Wireless Commun. Lett.*, vol. 7, no. 1, pp. 38–41, Feb. 2018.

[15] M. Alzenad and H. Yanikomeroglu, "Coverage and rate analysis for unmanned aerial vehicle base stations with LoS/NLoS propagation," in *Proc. IEEE Glob. Commun. Conf. (Globecom) Workshops*, Abu Dhabi, UAE, Dec. 2018, pp. 1–7.

[16] M. Alzenad and H. Yanikomeroglu, "Coverage and rate analysis for vertical heterogeneous networks (VHetNets)," *IEEE Trans. Wireless Commun.*, vol. 18, no. 12, pp. 5643–5657, Dec. 2019.

[17] N. Cherif, M. Alzenad, H. Yanikomeroglu, and A. Yongacoglu, "Downlink coverage and rate analysis of an aerial user in vertical heterogeneous networks (VHetNets)," *IEEE Trans. Wireless Commun.*, vol. 20, no. 3, pp. 1501–1516, Mar. 2021.

[18] [Online]. Available: https://www.amazon.com/Amazon-Prime-Air

[19] X. Cao, P. Yang, M. Alzenad, X. Xi, D. Wu, and H. Yanikomeroglu, "Airborne communication networks: A survey," *IEEE J. Select. Areas Commun.*, vol. 36, no. 9, pp. 1907–1926, Aug. 2018.

[20] S. Hayat, E. Yanmaz, and R. Muzaffar, "Survey on unmanned aerial vehicle networks for civil applications: A communications viewpoint," *IEEE Commun. Surv. Tutorial*, vol. 18, no. 4, pp. 2624–2661, Fourthquarter 2016.

[21] A. Kumbhar, F. Koohifar, I. Güvenç, and B. Mueller, "A survey on legacy and emerging technologies for public safety communications," *IEEE Commun. Surv. Tutorial*, vol. 19, no. 1, pp. 97–124, Firstquarter 2017.

[22] L. Gupta, R. Jain, and G. Vaszkun, "Survey of important issues in UAV communication networks," *IEEE Commun. Surv. Tutorial*, vol. 18, no. 2, pp. 1123–1152, Secondquarter 2016.

[23] A. M. Hayajneh, S. A. R. Zaidi, D. C. McLernon, M. Di Renzo, and M. Ghogho, "Performance analysis of UAV enabled disaster recovery networks: A stochastic geometric framework based on cluster processes," *IEEE Access*, vol. 6, pp. 26 215–26 230, 2018.

[24] J. Chen, M. Ding, and Q. T. Zhang, "Interference statistics and performance analysis of MIMO ad hoc networks in binomial fields," *IEEE Trans. Veh. Technol.*, vol. 61, no. 5, pp. 2033–2043, Jun. 2012.

[25] D. Torrieri and M. C. Valenti, "The outage probability of a finite ad hoc network in Nakagami fading," *IEEE Trans. Commun.*, vol. 60, no. 11, pp. 3509–3518, Nov. 2012.

[26] V. V. Chetlur and H. S. Dhillon, "Downlink coverage analysis for a finite 3-D wireless network of unmanned aerial vehicles," *IEEE Trans. Commun.*, vol. 65, no. 10, pp. 4543–4558, Oct. 2017.

[27] V. Yajnanarayana, Y.-P. E. Wang, S. Gao, S. Muruganathan, and X. L. Ericsson, "Interference mitigation methods for unmanned aerial vehicles served by cellular networks," in *IEEE 5G World Forum (5GWF)*, Silicon Valley, USA, Jul. 2018.

[28] M. Walter, S. Gligorević, T. Detert, and M. Schnell, "UHF/VHF air-to-air propagation measurements," in *Proc. fourth European Conf. Ant. Propag.*, Barcelona, Spain, Apr. 2010, pp. 1–5.

[29] N. Goddemeier and C. Wietfeld, "Investigation of air-to-air channel characteristics and a UAV specific extension to the Rice model," in *Proc. IEEE Glob. Commun. Conf. (Globecom) Workshops*, San Diego, CA, USA, Dec. 2015, pp. 1–5.

[30] M. Mozaffari, W. Saad, M. Bennis, and M. Debbah, "Efficient deployment of multiple unmanned aerial vehicles for optimal wireless coverage," *IEEE Commun. Lett.*, vol. 20, no. 8, pp. 1647–1650, Aug. 2016.

[31] V. V. Chetlur and H. S. Dhillon, "Coverage and rate analysis of downlink cellular vehicle-to-everything (C-V2X) communication," *IEEE Trans. Wireless Commun.*, vol. 19, no. 3, pp. 1738–1753, Mar. 2020.

[32] J. G. Andrews, F. Baccelli, and R. K. Ganti, "A tractable approach to coverage and rate in cellular networks," *IEEE Trans. Commun.*, vol. 59, no. 11, pp. 3122–3134, Nov. 2011.

[33] H. Jo, Y. J. Sang, P. Xia, and J. G. Andrews, "Heterogeneous cellular networks with flexible cell association: A comprehensive downlink SINR analysis," *IEEE Trans. Wireless. Commun.*, vol. 11, no. 10, pp. 3484–3495, Oct. 2012.

[34] I. Gradshteyn and I. Ryzhik, *Table of Integrals, Series, and Products.* Academic Press, Inc., Boston, MA, 1994.

[35] Y. Zeng, Q. Wu, and R. Zhang, “Accessing from the sky: A tutorial on UAV communications for 5G and beyond,” *Proceedings of the IEEE*, vol. 107, no. 12, pp. 2327–2375, Dec. 2019.

[36] I. Bor-Yaliniz and H. Yanikomeroglu, “The new frontier in RAN heterogeneity: Multi-tier drone-cells,” *IEEE Commun. Mag.*, vol. 54, no. 11, pp. 48–55, Nov. 2016.

[37] 3GPP, “Unmanned aerial system (UAS) support in 3GPP (release 17), TS 22.125,” Dec. 2019.

[38] W. Mei and R. Zhang, “Uplink cooperative NOMA for cellular-connected UAV,” *IEEE J. Select. Topics Signal Processing*, vol. 13, no. 3, pp. 644–656, Jun. 2019.

[39] A. Imran, M. Shateri, and R. Tafazolli, “On the comparison of performance, capacity and economics of terrestrial base station and high altitude platform based deployment of 4G,” in *Proceedings of the 6th ACM symposium on Performance evaluation of wireless ad hoc, sensor, and ubiquitous networks*, New York, USA, Oct. 2009, pp. 58–62.

[40] X. Zhou, J. Guo, S. Durrani, and H. Yanikomeroglu, “Uplink coverage performance of an underlay drone cell for temporary events,” in *Proc. IEEE Int. Conf. Commun. (ICC) Workshops*, Kansas City, MO, May 2018, pp. 1–6.

[41] T. Tomic, K. Schmid, P. Lutz, A. Domel, M. Kassecker, E. Mair, I. L. Grixa, F. Ruess, M. Suppa, and D. Burschka, “Toward a fully autonomous UAV: Research platform for indoor and outdoor urban search and rescue,” *IEEE Robotics & Autom. Mag.*, vol. 19, no. 3, pp. 46–56, Sep. 2012.

[42] F. Lagum, I. Bor-Yaliniz, and H. Yanikomeroglu, “Strategic densification with UAV-BSs in cellular networks,” *IEEE Wireless Commun. Lett.*, vol. 7, no. 3, pp. 384–387, Jun. 2018.

[43] C. She, C. Liu, T. Q. S. Quek, C. Yang, and Y. Li, "Ultra-reliable and low-latency communications in unmanned aerial vehicle communication systems," *IEEE Trans. Commun.*, vol. 67, no. 5, pp. 3768–3781, May 2019.

[44] N. Cherif, M. Alzenad, H. Yanikomeroglu, and A. Yongacoglu, "Downlink coverage analysis of an aerial user in vertical heterogeneous networks," in *Proc. IEEE Glob. Commun. Conf. (Globecom)*, Waikoloa, Hawaii, USA, Dec. 2019, pp. 1–6.

[45] N. Cherif, W. Jaafar, H. Yanikomeroglu, and A. Yongacoglu, "On the optimal 3D placement of a UAV base station for maximal coverage of UAV users," in *Proc. IEEE Glob. Commun. Conf. (Globecom)*, Taipei, Taiwan, Dec. 2020, pp. 1–6.

[46] A. Al-Hourani, S. Kandeepan, and S. Lardner, "Optimal LAP altitude for maximum coverage," *IEEE Wireless Commun. Lett.*, vol. 3, no. 6, pp. 569–572, Dec. 2014.

[47] C. Shen, T. Chang, J. Gong, Y. Zeng, and R. Zhang, "Multi-UAV interference coordination via joint trajectory and power control," *IEEE Trans. Signal Process.*, vol. 68, pp. 843–858, Jan. 2020.

[48] G. Geraci, A. Garcia-Rodriguez, L. Galati Giordano, D. López-Pérez, and E. Björnson, "Understanding UAV cellular communications: From existing networks to massive MIMO," *IEEE Access*, vol. 6, pp. 67 853–67 865, 2018.

[49] U. Challita, W. Saad, and C. Bettstetter, "Interference management for cellular-connected UAVs: A deep reinforcement learning approach," *IEEE Trans. Wireless Commun.*, vol. 18, no. 4, pp. 2125–2140, Apr. 2019.

[50] X. Zhou, S. Durrani, J. Guo, and H. Yanikomeroglu, "Underlay drone cell for temporary events: Impact of drone height and aerial channel environments," *IEEE Internet Things J.*, vol. 6, no. 2, pp. 1704–1718, Apr. 2019.

[51] ITU-R, "Recommendation p.1410-5: Propagation data and prediction methods required for the design of terrestrial broadband radio access systems operating in a frequency range from 3 to 60 GHz," *Tech. Rep.*, 2012.

[52] A. Al-Hourani, S. Kandeepan, and A. Jamalipour, "Modeling air-to-ground path loss for low altitude platforms in urban environments," in *Proc. IEEE Glob. Commun. Conf. (Globecom)*, Austin, TX, USA, Dec. 2014, pp. 2898–2904.

[53] D. S. Baum, J. Hansen, J. Salo, G. Del Galdo, M. Milojevic, and P. Kyösti, "An interim channel model for beyond-3G systems: extending the 3GPP spatial channel model (SCM)," in *Proc. IEEE Veh. Technol. Conf.*, vol. 5, Stockholm, Sweden, Dec. 2005, pp. 3132–3136.

[54] J. Holis and P. Pechac, "Elevation dependent shadowing model for mobile communications via high altitude platforms in built-up areas," *IEEE Trans. Anten. Propag.*, vol. 56, no. 4, pp. 1078–1084, Apr. 2008.

[55] M. Haenggi, *Stochastic Geometry for Wireless Networks.* Cambridge University Press, 2012.

[56] 3GPP, "Evolved universal terrestrial radio access (E-UTRA); further advancements for E-UTRA physical layer aspects (relase 9), TR 36.814," Mar. 2010.

[57] H. N. Qureshi and A. Imran, "Towards designing systems with large number of antennas for range extension in ground-to-air communications," in *Proc. IEEE Int. Symp. on Pers., Indoor and Mobile Radio Commun. (PIMRC)*, Bologna, Italy, Sep. 2018, pp. 1–5.

[58] ——, "On the tradeoffs between coverage radius, altitude, and beamwidth for practical UAV deployments," *IEEE Trans. Aerosp. Electron. Syst.*, vol. 55, no. 6, pp. 2805–2821, Jan. 2019.

[59] A. M. Mathai, R. K. Saxena, and H. J. Haubold, *The H-function: Theory and Applications.* Springer Science & Business Media, 2009.

[60] H. Alzer, "On some inequalities for the incomplete gamma function," vol. 66, no. 218, pp. 771–778, Apr. 1997.

[61] A. Merwaday, A. Tuncer, A. Kumbhar, and I. Guvenc, "Improved throughput coverage in natural disasters: Unmanned aerial base stations for public-safety communications," *IEEE Veh. Technol. Mag.*, vol. 11, no. 4, pp. 53–60, Dec. 2016.

[62] Federal Aviation Administration (FAA). [Online]. Available: https://www.faa.gov/uas/resources/by_the_numbers/

[63] M. Mozaffari, A. T. Z. Kasgari, W. Saad, M. Bennis, and M. Debbah, "Beyond 5G with UAVs: Foundations of a 3D wireless cellular network," *IEEE Trans. Wireless Commun.*, vol. 18, no. 1, pp. 357–372, Jan. 2019.

[64] N. Parvaresh and B. Kantarci, "Deep Q-learning-enabled deployment of aerial base stations in the presence of mobile users," ser. MobiWac '22. New York, NY, USA: Association for Computing Machinery, 2022, p. 73–80.

[65] N. Parvaresh, M. Kulhandjian, H. Kulhandjian, C. D'Amours, and B. Kantarci, "A tutorial on AI-powered 3D deployment of drone base stations: State of the art, applications and challenges," *Vehicular Communications (Elsevier)*, p. 100474, Aug. 2022.

[66] X. Liu, J. Wang, N. Zhao, Y. Chen, S. Zhang, Z. Ding, and F. R. Yu, "Placement and power allocation for NOMA-UAV networks," *IEEE Wireless Commun. Lett.*, vol. 8, no. 3, pp. 965–968, Jun. 2019.

[67] M. Mozaffari, A. T. Z. Kasgari, W. Saad, M. Bennis, and M. Debbah, "3D cellular network architecture with drones for beyond 5G," in *Proc. IEEE Glob. Commun. Conf. (Globecom)*, Abu Dhabi, UAE, Dec. 2018, pp. 1–6.

[68] W. Jaafar, T. Ohtsuki, W. Ajib, and D. Haccoun, "Impact of the CSI on the performance of cognitive relay networks with partial relay selection," *IEEE Trans. Veh. Tech.*, vol. 65, no. 2, pp. 673–684, Feb. 2016.

[69] M. Grant and S. P. Boyd, "CVX: MATLAB software for disciplined convex programming," *http://cvxr.com/cvx/*, Jan. 2014.

[70] K. Peng, J. Du, F. Lu, Q. Sun, Y. Dong, P. Zhou, and M. Hu, "A hybrid genetic algorithm on routing and scheduling for vehicle-assisted multi-drone parcel delivery," *IEEE Access*, vol. 7, pp. 49 191–49 200, 2019.

[71] J. K. Stolaroff, C. Samaras, E. R. O'Neill, A. Lubers, A. S. Mitchell, and D. Ceperley, "Energy use and life cycle greenhouse gas emissions of drones for commercial package delivery," *Nature Commun.*, vol. 9, no. 1, pp. 1–13, 2018.

[72] A. W. Sudbury and E. B. Hutchinson, "A cost analysis of amazon prime air (drone delivery)," *J. Eco. Educ.*, vol. 16, no. 1, pp. 1–12, 2016.

[73] M. Hamnanaka, "Optimum design for drone highway network," in *Proc. Inter. Conf. on UAS (ICUAS)*, Atlanta, GA, USA, Jun. 2019, pp. 923–929.

[74] A. Majd and E. Troubitsyna, "Integrating safety-aware route optimisation and run-time safety monitoring in controlling swarms of drones," Toulouse, France, Oct. 2017, pp. 94–95.

[75] Y. Zeng, J. Xu, and R. Zhang, "Energy minimization for wireless communication with rotary-wing UAV," *IEEE Trans. Wireless Commun.*, vol. 18, no. 4, pp. 2329–2345, Mar. 2019.

[76] R. A. Clothier, D. A. Greer, D. G. Greer, and A. M. Mehta, "Risk perception and the public acceptance of drones," *Risk Analysis*, vol. 35, no. 6, pp. 1167–1183, Feb. 2015.

[77] M. S. Alam, G. K. Kurt, H. Yanikomeroglu, P. Zhu, and N. D. Dao, "High altitude platform station based super macro base station (HAPS-SMBS) constellations," *IEEE Commun. Mag.*, vol. 59, no. 1, pp. 103–109, Jan. 2021.

[78] G. Karabulut Kurt, M. G. Khoshkholgh, S. Alfattani, A. Ibrahim, T. S. J. Darwish, M. S. Alam, H. Yanikomeroglu, and A. Yongacoglu, "A vision and framework for the high altitude platform station (HAPS) networks of the future," *IEEE Communications Surveys & Tutorials*, vol. 23, no. 2, pp. 729–779, Secondquarter 2021.

[79] T. S. Rappaport, G. R. MacCartney, M. K. Samimi, and S. Sun, "Wideband millimeter-wave propagation measurements and channel models for future wireless communication system design," *IEEE Trans. Commun.*, vol. 63, no. 9, pp. 3029–3056, Sep. 2015.

[80] M. Ozger, M. Vondra, and C. Cavdar, "Towards beyond visual line of sight piloting of UAVs with ultra reliable low latency communication," in *Proc. IEEE Glob. Commun. Conf. (Globecom)*, Abu Dhabi, UAE, Dec. 2018, pp. 1–6.

[81] S. Li, Y. Gu, B. Subedi, C. He, Y. Wan, A. Miyaji, and T. Higashino, "Beyond visual line of sight UAV control for remote monitoring using directional antennas," in *Proc. IEEE Glob. Commun. Conf. (Globecom) Workshops*, Waikoloa, HI, USA, Dec. 2019, pp. 1–6.

[82] R. M. de Amorim, J. Wigard, I. Z. Kovacs, T. B. Sorensen, and P. E. Mogensen, "Enabling cellular communication for aerial vehicles: Providing reliability for future applications," *IEEE Veh. Technol. Mag.*, vol. 15, no. 2, pp. 129–135, Jun. 2020.

[83] A. Fakhreddine, C. Bettstetter, S. Hayat, R. Muzaffar, and D. Emini, "Handover challenges for cellular-connected drones," in *Proc. ACM Workshop Micro Aerial Veh. Net., Sys., Applications*, Seoul, South Korea, Jun. 2019, pp. 9–14.

[84] E. Bulut and I. Guevenc, "Trajectory optimization for cellular-connected UAVs with disconnectivity constraint," in *Proc. IEEE Int. Conf. Commun. (ICC) Workshops*, Kansas City, MO, USA, May 2018, pp. 1–6.

[85] M. M. U. Chowdhury, S. J. Maeng, E. Bulut, and I. Güvenç, "3D trajectory optimization in UAV-assisted cellular networks considering antenna radiation pattern and backhaul constraint," *IEEE Trans. Aerosp. Electron. Syst.*, vol. 56, no. 5, pp. 3735–3750, Mar. 2020.

[86] U. Challita, W. Saad, and C. Bettstetter, "Deep reinforcement learning for interference-aware path planning of cellular-connected UAVs," in *Proc. IEEE Int. Conf. Commun. (ICC)*, Kansas City, MO, USA, May 2018, pp. 1–7.

[87] Y. Zeng and X. Xu, "Path design for cellular-connected UAV with reinforcement learning," in *Proc. IEEE Glob. Commun. Conf. (Globecom)*, Waikoloa, HI, USA, Dec. 2019, pp. 1–6.

[88] S. Zhang and R. Zhang, "Radio map based path planning for cellular-connected UAV," in *Proc. IEEE Glob. Commun. Conf. (Globecom)*, Waikoloa, HI, USA, Dec. 2019, pp. 1–6.

[89] M. M. Azari, A. H. Arani, and F. Rosas, "Mobile cellular-connected UAVs: Reinforcement learning for sky limits," in *Proc. IEEE Glob. Commun. Conf. (Globecom) Workshops*, Taipei, Taiwan, Dec. 2020, pp. 1–6.

[90] X. Xu and Y. Zeng, "Cellular-connected UAV: Performance analysis with 3D antenna modelling," in *Proc. IEEE Int. Conf. Commun. (ICC) Workshops*, Shanghai, China, May 2019, pp. 1–6.

[91] W. Jaafar and H. Yanikomeroglu, "Dynamics of laser-charged UAVs: A battery perspective," *IEEE Internet Things J.*, vol. 8, no. 13, pp. 10 573–10 582, Jul. 2021.

[92] J. K. Lenstra and A. H. G. R. Kan, "Complexity of vehicle routing and scheduling problems," *Networks*, vol. 11, no. 2, pp. 221–227, 1981.

[93] A. Alkhateeb, I. Beltagy, and S. Alex, "Machine learning for reliable mmwave systems: Blockage prediction and proactive handoff," in *IEEE Global Conf. on Sig. and Inf. Proc. (GlobalSIP)*, Anaheim, CA, USA, Feb. 2019, pp. 1055–1059.

[94] S. Euler, H.-L. Maattanen, X. Lin, Z. Zou, M. Bergström, and J. Sedin, "Mobility support for cellular connected unmanned aerial vehicles: Performance and analysis," in *Proc. IEEE Wireless Commun. Netw. Conf. (WCNC)*, Marrakesh, Morocco, Apr. 2019, pp. 1–6.

[95] Y. Chen, X. Lin, T. Khan, and M. Mozaffari, "Efficient drone mobility support using reinforcement learning," in *Proc. IEEE Wireless Commun. Netw. Conf. (WCNC)*, Seoul, South Korea, May 2020, pp. 1–6.

[96] N. Cherif, W. Jaafar, H. Yanikomeroglu, and A. Yongacoglu, "Disconnectivity-aware energy-efficient cargo-UAV trajectory planning with minimum handoffs," in *Proc. IEEE Int. Conf. Commun.*, Montreal, Quebec, Canada, Jun. 2021, pp. 1–6.

[97] Q. Wu, Y. Zeng, and R. Zhang, "Joint trajectory and communication design for multi-UAV enabled wireless networks," *IEEE Trans. Wireless Commun.*, vol. 17, no. 3, pp. 2109–2121, Mar. 2018.

[98] W. Jaafar, S. Naser, S. Muhaidat, P. C. Sofotasios, and H. Yanikomeroglu, "On the downlink performance of RSMA-based UAV communications," *IEEE Trans. Veh. Technol.*, vol. 69, no. 12, pp. 16 258–16 263, Dec. 2020.

[99] M. Kishk, A. Bader, and M.-S. Alouini, "Aerial base station deployment in 6G cellular networks using tethered drones: The mobility and endurance tradeoff," *IEEE Veh. Technol. Mag.*, vol. 15, no. 4, pp. 103–111, Sep. 2020.

[100] B. Galkin, J. Kibilda, and L. A. DaSilva, "UAVs as mobile infrastructure: Addressing battery lifetime," *IEEE Commun. Mag.*, vol. 57, no. 6, pp. 132–137, Jun. 2019.

[101] M. Erdelj, O. Saif, E. Natalizio, and I. Fantoni, "UAVs that fly forever: Uninterrupted structural inspection through automatic UAV replacement," *Ad Hoc Netw.*, vol. 94, p. 101612, Nov. 2019.

[102] M. A. Kishk, A. Bader, and M.-S. Alouini, "On the 3-D placement of airborne base stations using tethered UAVs," *IEEE Trans. Commun.*, vol. 68, no. 8, pp. 5202–5215, Aug. 2020.

[103] N. Tafintsev, D. Moltchanov, M. Gerasimenko, M. Gapeyenko, J. Zhu, S.-p. Yeh, N. Himayat, S. Andreev, Y. Koucheryavy, and M. Valkama, "Aerial access and backhaul in mmwave B5G systems: Performance dynamics and optimization," *IEEE Commun. Mag.*, vol. 58, no. 2, pp. 93–99, Feb. 2020.

[104] G. Castellanos, A. Colpaert, M. Deruyck, E. Tanghe, E. Vinogradov, L. Martens, S. Pollin, and W. Joseph, "Evaluation of beamsteering performance in multiuser

MIMO unmanned aerial base stations networks," *IEEE Access*, vol. 10, pp. 62 565–62 580, 2022.

[105] A. L. Yingst and V. Marojevic, "Tethered UAV with high gain antenna for BVLOS CNPC: A practical design for widespread use," in *IEEE International Symposium on a World of Wireless, Mobile and Multimedia Networks (WoWMoM)*, Pisa, Italy, Jul. 2021, pp. 323–328.

[106] M. Mirahsan, R. Schoenen, and H. Yanikomeroglu, "HetHetNets: Heterogeneous traffic distribution in heterogeneous wireless cellular networks," *IEEE J. Sel. Areas Commun.*, vol. 33, no. 10, pp. 2252–2265, Oct. 2015.

[107] J. Zhu, C.-H. Lung, and V. Srivastava, "A hybrid clustering technique using quantitative and qualitative data for wireless sensor networks," *Ad Hoc Networks (Elsevier)*, vol. 25, pp. 38–53, Feb. 2015.

[108] C.-H. Lung and C. Zhou, "Using hierarchical agglomerative clustering in wireless sensor networks: An energy-efficient and flexible approach," *Ad Hoc Networks (Elsevier)*, vol. 8, no. 3, pp. 328–344, May 2010.

[109] H. Safi, A. Dargahi, J. Cheng, and M. Safari, "Analytical channel model and link design optimization for Ground-to-HAP free-space optical communications," *Journal of Light. Tech.*, vol. 38, no. 18, Sep. 2020.